Universidade de São Paulo
Instituto de Astronomia, Geofísica e Ciências Atmosféricas
Departamento de Astronomia

Ivan Almeida

Winds and Feedback from underfed supermassive black holes

São Paulo
2023

Ivan Almeida

Winds and Feedback from underfed supermassive black holes

Thesis submitted to the Department of Astronomy from the Institute of Astronomy, Geophysics, and Atmospheric Science of the University of São Paulo as requisite for obtaining the PhD title.

Corrected version. The original is available at the Unit.

Concentration Area: Astronomy
Advisor(a): Prof. PhD Rodrigo Nemmen

São Paulo
2023

to Jade and Rosa

Acknowledgements

This thesis is a brief synthesis of four years of work and a presentation of the results. Scientific results carry relevant information about the studied topic; however, they do not discuss the history behind their production, and many things happened during this time.

Over these four years, numerous events occurred, and unfortunately, many of them were not favorable. The world faced a global pandemic (the last one occurred a hundred years ago), which is likely the most significant historical event of our century. COVID-19 victimized millions of people, a tragedy that I have never witnessed with my own eyes. It was a difficult time; initially, fear engulfed us, but after a few months, that fear transformed into depression and hopelessness. This feeling only subsided with the development of a vaccine. Here, I express my deep appreciation to all the scientists and healthcare workers who valiantly fought this battle. The pandemic had a profound impact on our lives and on our morale as scientists. Unfortunately, far-right movements with anti-science agendas gained power in many parts of the world in recent years. Regrettably, these groups are particularly strong here in Brazil. This further complicated the days for me and all other scientists. Nonetheless, we stood our ground and continued our work. For me, this thesis represents a personal victory after these challenging times, and I could not have completed it alone. There are many people I must thank.

I would like to say "Muito obrigado"to my family, who always supported my unconventional decision to become an astrophysicist. I cannot express my gratitude to them in English because they deserve to understand my words. Despite our financial situation, they consistently encouraged me to seek knowledge and satisfy my curiosity. I am grateful to my parents, Claudemir and Joana, who made many sacrifices to enable me to reach this point. I also extend my thanks to my younger sister, Mariana, for her support. She

will be finishing high school this year, and I hope she has a pleasant university experience, although not in astronomy as she is inclined towards the Humanities.

I must express my gratitude to my girlfriend, Stephane, who stood by me throughout the past three years. Both of us pursued our PhDs during the dark age of COVID-19, experiencing moments of fear, stress, and uncertainty. However, we remained together and overcame those difficult days. I firmly believe that I would not have succeeded without her help and love.

I extend my thanks to all the members of the IAG Black Hole group. Starting with my advisor, Prof. Rodrigo Nemmen, who trusted me and my abilities throughout this time and provided invaluable guidance on research, career development, and what it means to be a true scientist. I am deeply grateful to you. I also appreciate all my colleagues (both current and former) in the group: Artur, Douglas, Fabio, Gustavo, Lucas, Pedro, Raniere, Roberta, and Maria L'ucia. They have all been immensely helpful and have provided me with unforgettable moments of learning and friendship.

I must express my gratitude to all my friends, including the Tucuruvi team, my old friends from IFSP-SP and IFUSP (our pub table is always filled with great people), and all my IAG friends who have made my postgraduate life better. I especially want to thank my D&D friends Caval ao, Diogo, Gewers, L'eo, and Xorts, who provided immense support during the pandemic through their friendship. Fighting mythical creatures and devising plans to conquer formidable foes were crucial ways to escape the pain of being confined at home for two years. I will never forget the adventures of Alineu, Maril Za, Conall, Razael, Mei Donzza, Neneh, and the many other characters we created and saw grow.

Last but certainly not least, I am grateful to my cats, Jade and Rosa. Despite the moments of sadness or discomfort, embracing them tightly–despite their protests–always brought me happiness. This work was supported by FAPESP e CNPq.

FAPESP processo nº 2019/10054-7, Fundação de Amparo à Pesquisa do Estado de São Paulo (FAPESP); processo nº 2017/01461-2, Fundação de Amparo à Pesquisa do Estado de São Paulo (FAPESP).

CNPq processo nº141903/2019-8, Conselho Nacional de Desenvolvimento Cient'ifico e Tecnol'ogico

This work has made use of the computing facilities of the Laboratory of Astroinformatics (IAG/USP, NAT/Unicsul), whose purchase was made possible by the Brazilian agency

FAPESP (grant 2009/54006-4) and the INCT-A. Research developed with the help of HPC resources provided by the Information Technology Superintendence of the University of São Paulo.

As opiniões, hipóteses e conclusões ou recomendações expressas neste material são de responsabilidade do(s) autor(es) e não necessariamente refletem a visão da FAPESP.

O presente trabalho foi realizado com apoio do Conselho Nacional de Desenvolvimento Científico e Tecnológico (CNPq).

This thesis was written in LaTeX with the class `IAGTESE`, for thesis and dissertations from IAG.

"*Nothing is better than happiness, however a good sandwich is better than nothing*"

Lig Lig (chinese restaurant) fortune cookie

"*We're sometimes anti-social*
But we're always anti-fascist"

Stage Bottles

Resumo

No centro de cada galáxia gigante, existe um buraco negro supermassivo (SMBH). Esses objetos são conhecidos por coevoluir com suas galáxias hospedeiras e impactar em sua evolução. O efeito exato dos SMBHs ativos, os chamados núcleos galácticos ativos (AGN), sobre a galáxia ainda é uma questão em aberto. Nesta tese, estudamos os AGNs no universo local –os AGNs de baixa luminosidade (LLAGNs)– e como eles podem produzir ventos e impactar seu ambiente. Esta tese está dividida em três trabalhos principais sobre (i) a física da produção ce ventos nas pequenas escalas próximas ao SMBH; (ii) a interação dos outflows com a galáxia hospedeira; e (iii) melhorar a forma como vinculamos nossos modelos com as observações. Eles cobrem os diferentes aspectos do mesmo fenômeno: a atividade AGN de baixa luminosidade (LLAGN) e seu *feedback* através de intensos ventos. Estimamos em nosso trabalho a capacidade desses sistemas de produzir escoamentos que ejetam uma quantidade razoável de energia das escalas de subparsec $L_{\rm wind} \sim 0.01{-}0.08\dot{M}c^2$ – em unidades físicas $\sim 10^{39-40}$erg/s. Com ventos fortes como este, estimamos que SMBHs com $M_{\rm BH} \gtrsim 10^8 M_\odot$ e $\dot{M} \gtrsim 10^{-3}\dot{M}_{\rm Edd}$ podem reduzir a taxa de formação estelar em mais de 10% em 10^7 anos de atividade. Paralelamente, também desenvolvemos o código `AGNNES`, uma nova forma de calcular a densidade de energia espectral de um LLAGN usando IA com um aumento de velocidade considerável.

Abstract

At the centre of each giant galaxy, there is a supermassive black hole (SMBH). These objects are known to coevolve with their host galaxies and impact their life. The exact effect of the active SMBHs, the so-called active galactic nuclei (AGN), over the galaxy is an open question. In this thesis, we studied the AGN in the local universe –the low-luminosity AGN (LLAGN)– and how they can produce winds and impact their environment. This thesis is divided into three main works regarding (i) the physics of wind production in the small scales near the SMBH; (ii) the interaction of the outflows with the host galaxy; and (iii) improving how we constrain our models with observations. They cover the different aspects of the same phenomenon: the low-luminosity AGN (LLAGN) activity and their feedback through powerful winds. We estimated in our work the ability of these systems to produce outflows that carry away from the subparsec scales a reasonable amount of energy $L_{\rm wind} \sim 0.01 - 0.08\dot{M}c^2$ – in physical units $\sim 10^{39-40}$erg/s. With winds powerful as this, we estimated that SMBHs with $M_{\rm BH} \gtrsim 10^8 M_\odot$ and $\dot{M} \gtrsim 10^{-3}\dot{M}_{\rm Edd}$ can reduce the star formation rate in more than 10% in 10^7yr of activity. In parallel, we also developed the code AGNNES, a new way to calculate an LLAGN spectral energy density using AI with a considerable speed-up.

List of Figures

1.1 Masses of the detected object by the LIGO/VIRGO consortium before 2020 31
1.2 AGN unified model 33
1.3 Physical size of the AGN structures compared to the galaxy 34
1.4 BH zones 36
1.5 Accretion discs in the function of the efficiency parameter ϵ 39
1.6 Representation of a Low-Luminosity AGN 41
1.7 Hot accretion flows SEDs 47
1.8 SgrA* imaged by EHT 50
1.9 X-ray emission from SgrA* 50
1.10 SED of SgrA* 51
1.11 Ionized gas inside Akira 52
1.12 BH mass and the bulge stars velocity dispersion 54

2.1 Disc regions following the $-hu_t$ 68
2.2 Particles trajectories 69
2.3 Plots showing the density map and velocity field for the simulations. These maps were averaged on time between 45000 GM/c^3 and 50000 GM/c^3. . . 70
2.4 Continuation of figure 2.3. 71
2.5 Time evolution of the accretion rate and the magnetic flux at r_H for the simulations. 73
2.6 Continuation of figure 2.5. 74
2.7 Time evolution of the wind efficiency at some radius –R = 50M (red solid line), R = 200M (cyan dashed line), and R = 1000M (yellow dash-dotted line) for the simulations. 76

2.8 Continuation of figure 2.7. 77
2.9 Jet and wind efficiency as radius function for the simulations. 78
2.10 Continuation of figure 2.9. 79
2.11 Lost mass through outflows and accretion 80
2.12 Particles radial velocity 81
2.13 Angular distribution of the ejected particles 82
2.14 Continuation of figure 2.13. 83
2.15 Continuation of figure 2.14. 84
2.16 Continuation of figure 2.15. 85
2.17 Relation of the results for s and η_w with the initial parameters 87

3.1 Overview of the neural network architecture 100
3.2 Posterior distribution of parameters for the RIAF model tests 103
3.3 Posterior distribution of parameters for jet model tests 104
3.4 M87 SED best fit 108
3.5 Posterior distributions for M87 108
3.6 NGC 315 SED best fit 109
3.7 Posterior distributions for NGC 315 110
3.8 NGC 4261 SED best-fit 110
3.9 Posterior distributions for NGC 4261 111
3.10 NGC 4261 SED best-fit (no UV) 112
3.11 Posterior distributions for NGC 4261 (no UV) 112
3.12 Comparison between the SEDs calculated with `AGNNES` and the fiducial model 114

4.1 Energy injected by LLAGN winds 121
4.2 The quenching fraction as a function of the average heating of the region . 124
4.3 Quenching fraction inside a region of 20kpc as a function of the LLAGN accretion rate 125
4.4 Family of accreting SMBH parameters required to produce quenching of star formation of at least ten per cent, as a function of BH mass 126
4.5 Wind power required to produce quenching of star formation of at least ten per cent 127

A.1 Comparison of AGNNES predictions (blue line and black dots) with the fiducial RIAF model (red line). 160
A.2 Comparison of AGNNES predictions (blue line and black dots) with the fiducial jet model (red line). 161

B.1 Image from Vanzo and Siviglia (2018) showing the discrete grid. In this problem, we know the values of x_n at t^n, the objective is to calculate the value of x_n at $t^{n+1} = t^n + \Delta t$. 164
B.2 A generic cell 165
B.3 The Riemann problem 166

C.1 Solution of equation (C.15) 176

List of Tables

2.1 Set of simulations and their initial parameters. 66

2.2 Results concerning outflows for all simulations. 86

3.1 Separation of dataset into training, validation, and test. 100

3.2 `AGNNES` test results. Error bars correspond to 68% confidence intervals. . . 104

3.3 Resulting parameters from fitting `AGNNES` to our LLAGN sample. † Neglects UV observations. 106

A.1 SED data for M87. 158

A.2 SED data for NGC 315. 158

A.3 SED data for NGC 4261. 159

Contents

1. Introduction 29

1.1 Overview of the thesis 29

1.2 Black Holes 30

1.3 SMBHs in the universe 32

1.4 Characterizing BHs 34

1.4.1 Kerr metric 34

1.4.2 Interesting features of a Kerr BH 35

1.5 Accretion physics 37

1.6 Cold accretion flows 39

1.7 Hot accretion flows 40

1.7.1 One-dimensional solution 40

1.7.2 Two-temperature fluid 45

1.7.3 Theoretical spectrum 46

1.7.4 Numerical simulations 48

1.7.5 Observations of hot accretion flows in nature 48

1.8 AGN feedback 52

1.8.1 Thesis structure 55

2. GRMHD numerical simulations 57

2.1 Introduction 57

2.2 HD simulations 60

2.3 General Relativistic Magnetohydrodynamics 61

2.3.1 `H-AMR` 61

2.3.2 GRMHD equations . . . 62
2.4 Numerical methods . . . 64
2.5 Simulations overview . . . 65
2.5.1 Initial conditions . . . 65
2.5.2 Lagrangian particle tracking . . . 67
2.6 Simulations results . . . 69
2.6.1 Accretion flow properties . . . 69
2.6.2 Wind properties . . . 72
2.6.3 Analysis using tracer particles . . . 80
2.7 Discussion . . . 81
2.7.1 Accretion flow and density radial profile . . . 81
2.7.2 Wind launching mechanism . . . 88
2.7.3 Comparison with observations . . . 89
2.7.4 Comparison with previous numerical simulations . . . 91
2.7.5 Shortcomings . . . 92
2.8 Summary . . . 93

3. AGNNES . . . 95
3.1 Introduction . . . 95
3.2 Methods . . . 97
3.2.1 RIAF and jet . . . 97
3.2.1.1 RIAF . . . 98
3.2.1.2 Jet . . . 98
3.2.2 Neural network . . . 99
3.2.3 `AGNNES`'s performance . . . 101
3.2.4 Fitting Method . . . 101
3.3 Results . . . 102
3.3.1 Tests . . . 102
3.3.2 Applications to observations . . . 103
3.3.2.1 M87 . . . 107
3.3.2.2 NGC 315 and NGC 4261 . . . 107
3.4 Discussion . . . 113

3.4.1 Model accuracy . . . 113
3.4.2 Comparison with previous work . . . 113
3.4.3 Shortcomings . . . 115
3.5 Summary . . . 116

4. RIAF winds and Feedback . . . 117
4.1 Introduction . . . 117
4.2 Model . . . 118
4.2.1 Galaxy . . . 118
4.2.2 LLAGN Energy Output . . . 119
4.2.3 Star-formation . . . 120
4.3 Results . . . 120
4.3.1 Energetics . . . 120
4.3.2 How far does the wind reach? . . . 120
4.3.3 Star formation quenching . . . 123
4.4 Discussion . . . 128
4.5 Summary . . . 129

5. Summary . . . 131

Bibliography . . . 133

Appendix 155

A. AGNNES Appendix . . . 157
A.1 Observational data . . . 157
A.2 Further validations . . . 159

B. Numerical Methods - Riemman Problem and Godunov method . . . 163
B.1 Godunov Method . . . 165
B.2 Solving the Riemann problem: The HLL solver . . . 168

C. Wind calculations . . . 171
C.1 Expanding bubble . . . 171

C.1.1 Flow timescale 171
C.1.2 Cooling timescale 172
C.1.3 Wind radius 173
C.2 Thermal transfer 173
C.2.1 Analytical Solving 174
C.2.2 Numerical Solving 175

List of Abbreviations

- ADAF – Advection Dominated Accretion Flow
- ADIOS – Adiabatic Inflow-Outflow Solution
- AGN – Active Galactic Nuclei
- BH – Black Hole
- GR – General Relativity
- GRMHD – General Relativistic Magnetohydrodynamics
- HD – Hydrodynamics
- LLAGN – Low-Luminosity Active Galactic Nuclei
- MHD – Magnetohydrodynamics
- ML – Machine Learning
- NN – Neural Network
- RIAF – Radiatively Inefficient Accretion Flow
- SED – Spectral Energy Density
- SMBH – Supermassive Black Hole

Constants and important variables list

- $c = 3 \times 10^{10}$ cm s^{-1} – speed of light
- $G = 6.67 \times 10^{-8}$ cm^3 g^{-1} s^{-2} – gravitational constant
- $e = 4.80$ cm$^{3/2}$ g$^{1/2}$ s^{-1} – electron charge
- $k_B = 1.38 \times 10^{-16}$ erg K^{-1} – Boltzmann constant
- $\hbar = 1.05 \times 10^{-27}$ cm^2 g s^{-1} – reduced Planck constant
- $L_{\rm Edd}$ (see equation (1.10)) – Eddington luminosity
- $m_H = 1.66 \times 10^{-24}$ g – hydrogen mass
- $M_\odot = 1.99 \times 10^{33}$ g – solar mass
- $\dot{M}_{\rm Edd}$ (see equation (1.11)) – Eddington mass accretion rate
- $\sigma_T = 6.65 \times 10^{-25}$ cm^2– Thompson cross-section for an electron

Chapter 1

Introduction

1.1 Overview of the thesis

Supermassive black holes (SMBH) lie in the centre of every early or late type galaxy. They are known to coevolve with their host galaxies and impact their evolution. How this happens–the details of active galactic nuclei (AGN) feedback–is an ongoing field of study. There are several outstanding open questions regarding the interplay of SMBHs. This thesis focuses on SMBH accretion in the nearby universe, typified by low accretion rates. It is an open question of how these black holes (BHs) produce winds and the feedback impact of these winds. Our work tackles these questions on three fronts:

- The physics of wind production in the small scales near the SMBH.
- The interaction of the outflows with the host galaxy.
- Improving how we constrain our models with observations.

The three topics were developed as different projects which became the main chapters of this thesis. Chapter 1 offers a more detailed introduction to AGN physics and feedback. This chapter aims to provide a background and context to the thesis work. Chapters 2-4 are independent and can be read in any order. They are the main body of the thesis. They cover different aspects of the same phenomenon: the low-luminosity AGN (LLAGN) activity.

We start by numerically exploring the physics of BH accretion in chapter 2, how the magnetized gas can fall into the SMBH and the physical processes that produce powerful outflows. These are simulations occurring at the innermost region of the LLAGN and profile the ejection from these subparsec scales.

The accretion disc is not bigger than a single parsec. It can still produce outflows capable of affecting the host galaxy, which is a million to billion times bigger. The dichotomy between SMBH and galaxy can be seen with our telescopes. Significant relations like the M-σ and the bubbles in galaxy clusters show the connections between the AGN ejecta and the larger environment. In the third chapter, we create a simplified theoretical model for the interaction of LLAGN winds and the medium. We used the previous knowledge from our simulations (Almeida and Nemmen (2020) and the results from chapter 2) and extrapolate these results to the larger galaxy scales, calculating a possible impact of the winds.

The following two chapters delve into the observational modelling of LLAGN. In our work, we also developed a model to fit the LLAGN SEDs, as reported in the fourth chapter. The SED fitting gives us essential information to constrain and test our models against the natural universe. Comparing models to real data is necessary for a theorist because their union of them is the best way to understand nature.

The common thread of the work described in chapter 2-4 are LLAGN winds. Each of them offers a piece to this puzzle. We worked to link the different scales of the problem, the subparsec accretion disc region and the galactic environment, consistent with the observational signatures. Ultimately, we aimed to characterize the whole picture of the phenomena –arguably a herculean task– from the accretion disc of the LLAGN to their impact over the galaxy and their observational features.

1.2 Black Holes

Black holes (BH) are for sure one of the most fascinating and mysterious objects of the universe. Their mystery lies in the impossibility to explain their properties based on our human senses and time and space perception. These objects enclose giants amounts of mass in extremely small volumes, we can estimate the radius of an Earth-size black for example using the classic Schwarzschild radius formula:

$$R_S = \frac{2GM}{c^2} = 2R_g. \tag{1.1}$$

In this case, we got the value of 0.89cm. It is unimaginable for anyone all the mountains of the planet along with all the people, and everything else to be comprised in such a small

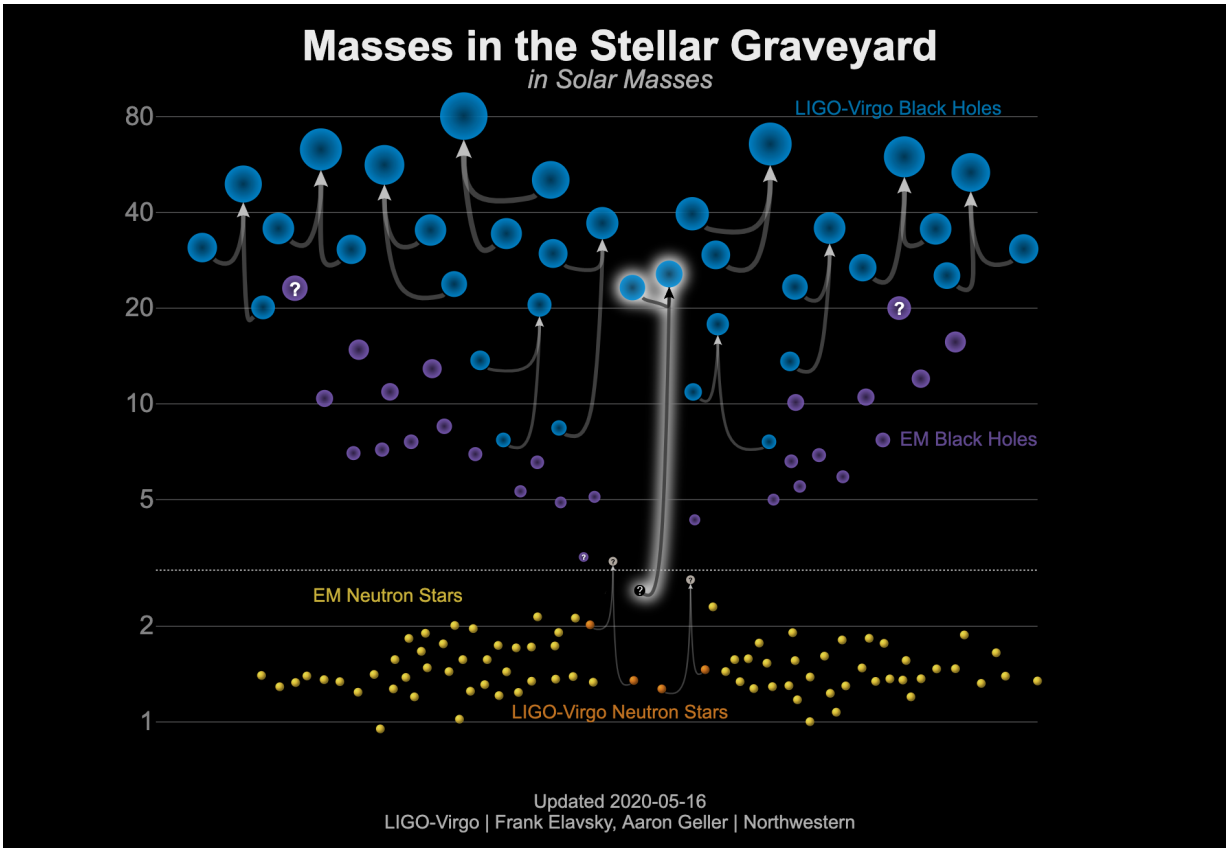

Figure 1.1: Masses of the detected object by the LIGO/VIRGO consortium before 2020. We can see the BHs in the upper part of the figure, LIGO detected stellar mass black holes from $3M_\odot$ to $100M_\odot$. These BHs are in the range of the so-called stellar mass black holes.

sphere. Physically speaking, the Schwarzschild radius is the radius of an object with mass M, without rotation, in that the escape velocity from its gravitational field is equal to the speed of light (c); here G is the gravitational constant. Once inside R_S only superluminal particles could escape from the BH–which relativity promptly forbids. In equation 1.1, we defined R_g as GM/c^2, and we will call it gravitational radius and we will use it as our length unit in the next sections.

In nature, we never found a BH with such mass. Usually, they come in two populations: the stellar and supermassive BHs. Talking briefly about stellar-size BHs, these objects are remnants of high massive stars that collapsed under their own gravity after their fuel was exhausted. The mass range comes from $\sim 3M_\odot$ to almost $100M_\odot$. The range of stellar-mass BHs detected by the LIGO/VIRGO consortium shown in figure 1.1 is a good sample of this population mass range. In this work, we will not explore these types of objects, we are interested in the other group the supermassive BHs (SMBHs).

SMBHs are in total different mass scales, hanging from millions to billions of solar

masses. In this category, we have the BHs living in the giant galaxies centre (Ferrarese and Ford, 2005). Objects like SgrA* and M87* were SMBHs imaged by the EHT collaboration (Akiyama et al., 2019a, 2022a). SMBHs were extensively studied in the last decades, they present very characteristic and strong radiation emission across all wavelengths.

We will dwell on the SMBHs world in the next section, but before let me cite the intermediate mass BHs, the category between the stellar and supermassive. Surprisingly, we had very few observations of BHs in this mass range, the absence of them is an open question in black hole astrophysics. We expect to observe some of them hanging around the universe, in the centre of dwarf galaxies and massive globular clusters.

1.3 SMBHs in the universe

There are plenty of SMBHs in the universe. Many of them live in the centre of giant galaxies and shine from radio to γ-rays in the sky. A BH cannot emit light to be detectable to our telescopes. Still, we can see the interaction between matter and the BH, independent of the BH mass.

Once a BH is in a gas-rich environment, it starts to gravitationally attract the material and accrete it through an accretion disc (Frank et al., 2002). This process occurs naturally both to stellar or supermassive BHs. The accreting stellar BHs can be seen in the so-called high-massive x-ray binaries. For the case of SMBHs, we have the phenomena called active galactic nuclei (AGN), which is the state when the SMBH is accreting available gas from the galactic nucleus. The origin of the gas could be from galactic mergers, stellar tidal disruptions, or material that comes from the galaxy and fell into the central SMBH via dynamical friction. AGNs have been studied for a long time, and before the 60s, their physical mechanism was a complete mystery.

AGNs are very complex systems. The unified model–a model that, as the name says, is an effort to explain them adequately–is displayed in figure 1.2. It is composed of an accreting black hole surrounded by a giant dust torus; this system could present a relativistic jet too (Beckmann and Shrader, 2012; Netzer, 2015).

Spatially speaking we have the following structures with sizes represented in figure 1.3:

- The accretion disc is in the core of the AGN and corresponds to a tiny region. The average size of the accretion disc is in subparsec scales, which is almost impossible

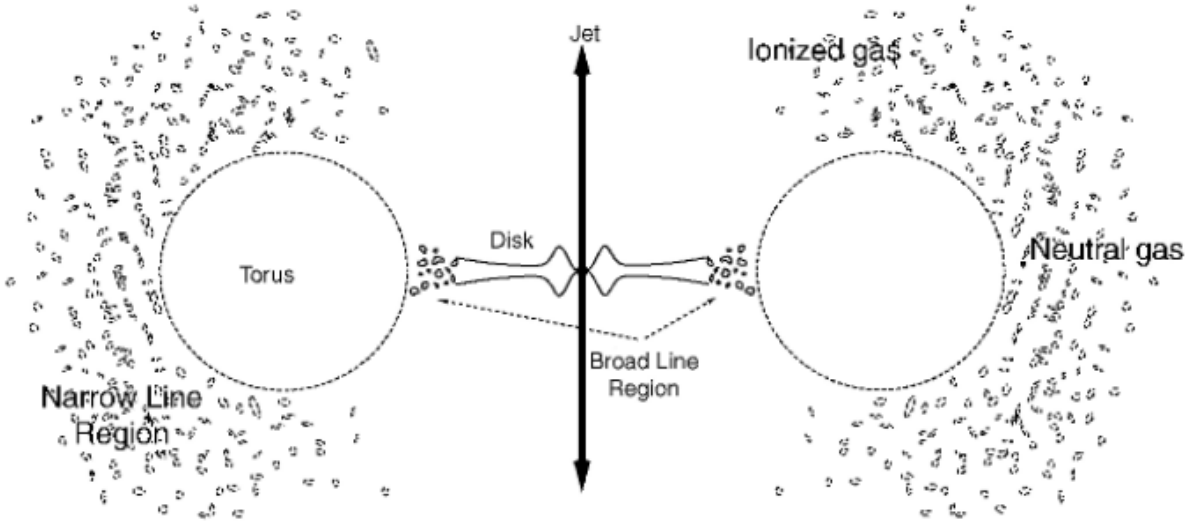

Figure 1.2: Simplified sketch of the AGN unified model extracted from Schneider (2006) (figure 5.25).

to resolve with typical telescopes (only GRAVITY and the Event Horizon Telescope collaborations (Doeleman et al., 2008; Abuter et al., 2018; Akiyama et al., 2022a) achieved it). However, it is still a big challenge to do it for most extragalactic sources (cf. Sturm et al. 2018).

- The dust torus is an irregular parsec scale structure surrounding the accretion disc.
- The relativistic jet is a structure that arises from the interaction between the infalling plasma and the BH highly distorted spacetime at its vicinity.
- BH jets are the most notable feature of an AGN and can reach Mpc scales.

AGNs span many physical scales, making studying them very complex. Typically an SMBH has a physical scale of an astronomical unit (see equation (1.2)) and can launch a relativistic jet able to reach megaparsec scales. Unifying all the phenomena is still a challenge for the astronomers

$$R_S \approx 2 \text{ AU } \left(\frac{M_{BH}}{10^8 M_\odot}\right) = 10^{-5} \text{ pc } \left(\frac{M_{BH}}{10^8 M_\odot}\right) \tag{1.2}$$

AGNs are very diverse, with several categories such as quasars, Seyfert galaxies, radio galaxies, blazars etc. Our study focused on low-luminosity AGNs (LLAGNs), a common type of AGN in the nearby universe. LLAGNs, as the name reveals, are ones with much

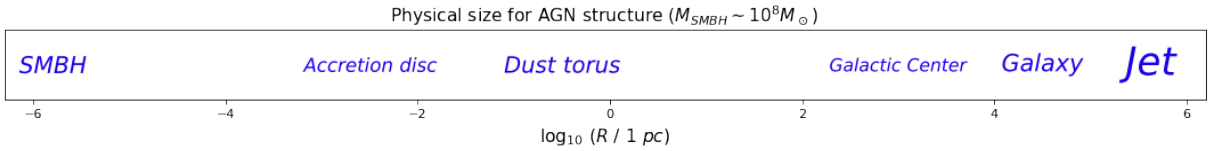

Figure 1.3: Representation of the physical size of the AGN structures compared to the galactic size. In this figure, we can see the extension of the problem, coming from microparsec scales to megaparsecs.

smaller luminosity than quasars (and other AGN types). They usually are present in quiescent galaxies. The smaller luminosity is indicative that the SMBH is underfed, compared to an SMBH in a quasar. The physics behind the accretion will be better explored in the section 1.5.

1.4 Characterizing BHs

SMBHs are the main engine of AGNs. In this section, I will provide a quick characterization of these objects. Firstly, we can consider the objects as charge neutral in the large-scale universe. So we assume SMBHs can be described as Kerr BHs. We only need two main parameters to characterize these objects, the mass M and the spin a (a proxy for the angular momentum).

1.4.1 Kerr metric

A Kerr black hole spacetime can be mathematically described by the Kerr metric. There are two famous ways to present the metric: the Boyer-Lindquist coordinates (BLc) and the Kerr-Schild coordinates (KSc). Each representation has its pros. In this section, we are using the units $G = c = 1$.

The BLc favours the visualization of some main features of the BH spacetime, like the event horizon and the singularity ring. Using BLc, the BH rotating spacetime can be written as

$$ds^2 = -\left(1 - \frac{2Mr}{\Sigma^2}\right) dt^2 + \frac{\Sigma^2}{\Delta} dr^2 + \Sigma^2 d\theta^2 + \left(r^2 + a^2 - \frac{2Ma^2 r \sin^2\theta}{\Sigma^2}\right) \sin^2\theta d\phi^2 - \frac{2Mar\sin^2\theta}{\Sigma^2} dt d\phi. \tag{1.3}$$

In equation (1.3): $\Delta = r^2 - 2Mr + a^2$ and $\Sigma = r^2 + a^2\cos^2\theta$. The conversion between cartesian coordinates and BLc is written in equation (1.4).

$$\begin{aligned} x &= \sqrt{r^2 + a^2} \sin\theta \cos\phi \\ y &= \sqrt{r^2 + a^2} \sin\theta \sin\phi \\ z &= \sqrt{r^2 + a^2} \cos\theta \end{aligned} \tag{1.4}$$

It is easy to spot that $\Delta = 0$ is a singularity. Solving this equation, we find two surfaces described in equation (1.5).

$$\begin{aligned} r_+ &= M + \sqrt{M^2 - a^2} \\ r_- &= M - \sqrt{M^2 - a^2} \end{aligned} \tag{1.5}$$

$r_\pm$ are two null surfaces, being r_+ a "point of no return of the BH, the famous event horizon. r_- is an inner boundary inside the BH event horizon, and its nature is outside the scope of our work.

It is important to note that if we assume the BH has spin $a = 0$, i.e. non-rotating BH, equation (1.3) is reduced to the Schwarzschild metric. Furthermore, the event horizon size r_+ (see equation (1.5)) equals the Schwarzschild radius (equation (1.1)).

The event horizon singularity is a *coordinate singularity*, depending on the choice of coordinates. In the BLc, it is the r_+ surface corresponding to the singularity of $\Delta = 0$. If we change these coordinates to the KSc, the event horizon singularity vanishes. In particular, KSc is relevant to us because the numerical code H-AMR solves the fluid equation in a curved spacetime using this metric. The Kerr BH spacetime can be described using KSc as written in equation (1.6).

$$ds^2 = \eta_{\mu\nu} + \frac{2Mr^3}{r^4 + a^2 z^2} \left(dt + \frac{rx + ay}{r^2 + a^2} dx + \frac{ry - ax}{r^2 + a^2} dy + \frac{z}{r} dz \right)^2 \tag{1.6}$$

Here, r is defined as the solution of $r^4 - (x^2 + y^2 + z^2 - a^2)r^2 - a^2 z^2 = 0$.

1.4.2 Interesting features of a Kerr BH

The event horizon was described in the previous section. BHs also have another interesting region in their vicinity called the *ergosphere*. This region is outside the event horizon, and a particle inside it cannot remain at rest. The ergosphere is a region delimited by the surface:

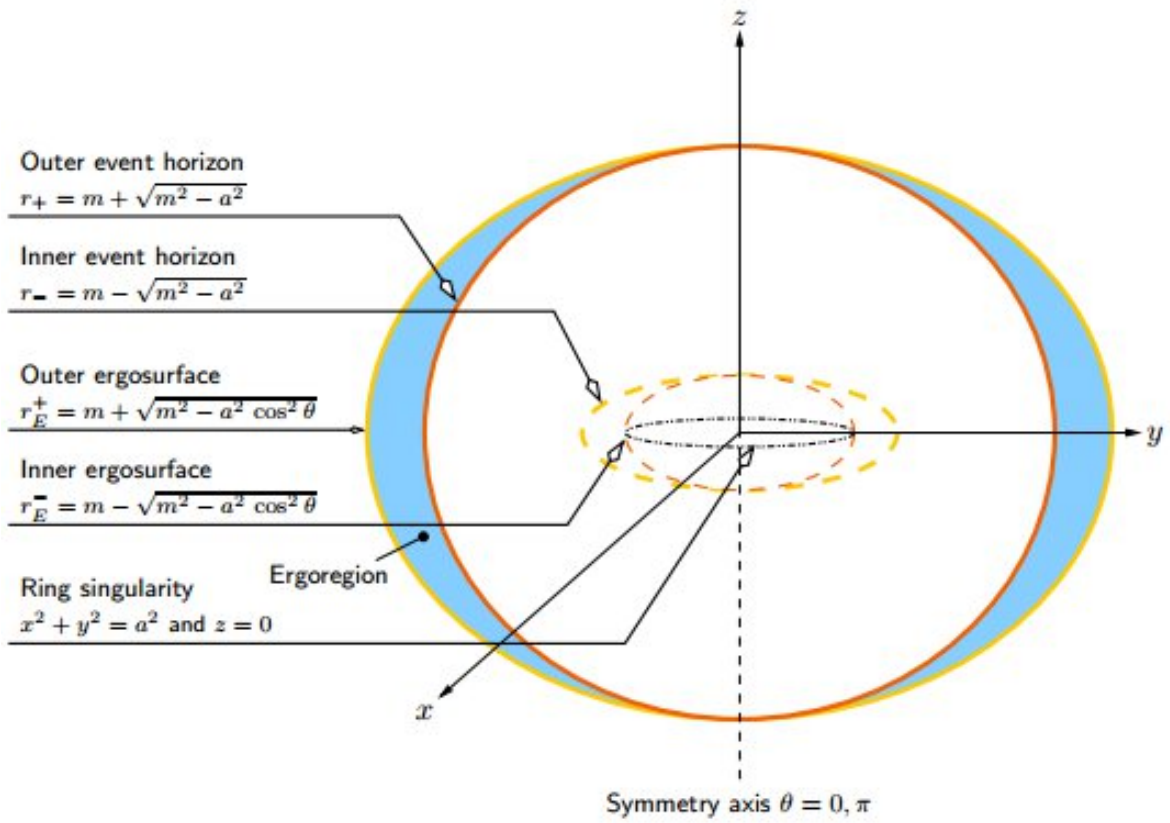

Figure 1: Schematic location of the horizons, ergosurfaces, and curvature singularity in the Kerr spacetime.

Figure 1.4: Representation of the BH's zones. This figure is extracted from Visser (2007)

$$r_{\text{erg}} = M + \sqrt{M^2 - a^2 \cos^2\theta} \tag{1.7}$$

At the poles, ($cos\theta = 1$), the ergosphere boundary overlaps the event horizon. Once a particle is trapped between r_+ and r_{erg}, it is obligated to rotate along the BH, being impossible to be static. The name of this effect is *frame dragging*. For a more mathematical treatment see Misner et al. (1973). These BH zones and important surfaces is shown in figure 1.4.

An observer at infinity can measure the energy of particles inside the ergosphere and notice a particle with negative energy. This shocking observation is a unique feature of GR and BHs. At first glance, this is an utterly unintuitive fact. Still, it allows some notorious physical processes involving the energy extraction from the Kerr BH spacetime called Penrose processes. Without delving into the equations, the Penrose process will enable particles to obtain large amounts of energy and escape the BH gravitational zone

of influence. In simplified words, a particle p_0 inside the ergosphere with energy E_0 could decay into two different particles p_+ and p_- with corresponding energies E_+ and E_-. Supposing the energy necessary to escape the BH gravitational binding is E_g. Let's do the following considerations:

$$\begin{aligned} E_0 &< E_g \\ E_0 &= E_+ + E_- \end{aligned} \tag{1.8}$$

If $E_- < 0$, it implies in $E_+ > E_0$. In the case of $E_+ > E_g$, the particle p_+ has enough energy to escape the BH, while p_- will be accreted. In the end, the ejected particle has a larger energy than the original particle p_0 by the amount $|E_-|$. The net energetic gain comes from extracting the BH's spacetime rotating energy. For example, the Blandford-Znajek process (Blandford and Znajek, 1977) that triggers the relativistic jet can be understood as a magnetic Penrose process observable in nature.

1.5 Accretion physics

Whenever a massive central object is surrounded by gas, the gas naturally falls into the centre via accretion discs. Accretion discs are born when a fluid with angular momentum falls under the influence of a gravitational field originating from a central object (or set of objects). These discs can be present around ordinary stars, white dwarves, neutron stars, and BHs.

The matter forms a disk-like structure while falling into the central object due to the angular moment that barries a free-fall movement. However, to fall, the gas needs to transfer angular momentum somehow. To allow the momentum transfer and the accretion process, we need the presence of magnetic fields. Magnetic stresses in the ionized plasma introduce friction enabling the gas to flow toward the BH (Balbus, 2003). In practice, the magnetic field converts part of the gravitational potential energy of the accretion flows into heat, working as an "effective viscosity". A considerable fraction of their rest mass energy can be released as energy, being the main power source behind AGNs, black hole binaries and gamma-ray bursts (Meier, 2012).

The accretion disc dynamics is directly impacted by what happens to the produced thermal energy is irradiated (Abramowicz and Fragile, 2013). We can parameterize the

radiative efficiency as

$$\eta = L/\dot{M}c^2. \tag{1.9}$$

L is the radiative luminosity produced by the accretion flow. $\dot{M}$ is the mass accretion rate and c is the traditional speed of light. η becomes the radiative efficiency. Higher values of η mean the thermal energy produced by the accretion flow is more efficiently emitted away as electromagnetic radiation.

Another useful parameterization to study the accretion flows is the Eddington luminosity and mass accretion rate. The Eddington luminosity is defined as the luminosity needed to prevent a steady spherical gas accretion. Mathematically we can define it as the situation where $P_{\rm gas} = P_{\rm Rad}$. This value is

$$L_{\rm Edd} = GM\frac{4\pi m_H c}{\sigma_T} = 1.26 \times 10^{46}\left(\frac{M}{10^8 M_\odot}\right)\ {\rm erg/s}. \tag{1.10}$$

M is the BH mass, and the other constants can be seen in the constant list . We can relate the Eddington luminosity to a mass accretion luminosity using (1.12) into (1.10).

$$\dot{M}_{\rm Edd} = \frac{L_{\rm Edd}}{\eta c^2} \approx 2.1 M_\odot/{\rm yr}\ \left(\frac{M}{10^8 M_\odot}\right)\left(\frac{\eta}{0.1}\right)^{-1} \tag{1.11}$$

Finally, we can define the efficiency ϵ as the ratio between the AGN luminosity (SMBH mass accretion rate) over the Eddington luminosity (mass accretion rate).

$$\epsilon = \frac{L_{\rm AGN}}{L_{\rm Edd}} = \frac{\dot{M}_{\rm BH}}{\dot{M}_{\rm Edd}} \tag{1.12}$$

In figure 1.7, we related the accretion flow characteristics with the efficiencies η e ϵ. The notable impact of ϵ is visible in the disc dynamics. The accretion disc is geometrically thick, supported by the hot gas pressure and presents smaller radiative efficiency for small accretion rates (i.e. $\epsilon \leq 10^{-2}$). Most of the AGNs in the local universe are accreting at this state and show smaller luminosities. In this work, we are particularly interested in BHs accreting at low $\dot{M}$. At rates below $\epsilon = 0.01$, the gas cannot properly radiate its thermal energy away and becomes extremely hot ($T \sim 10^{12}$ K), inflated, and optically thin, giving rise to what we call "radiatively inefficient accretion flow" (RIAF) (Yuan and Narayan, 2014). For more details, see section 1.7.

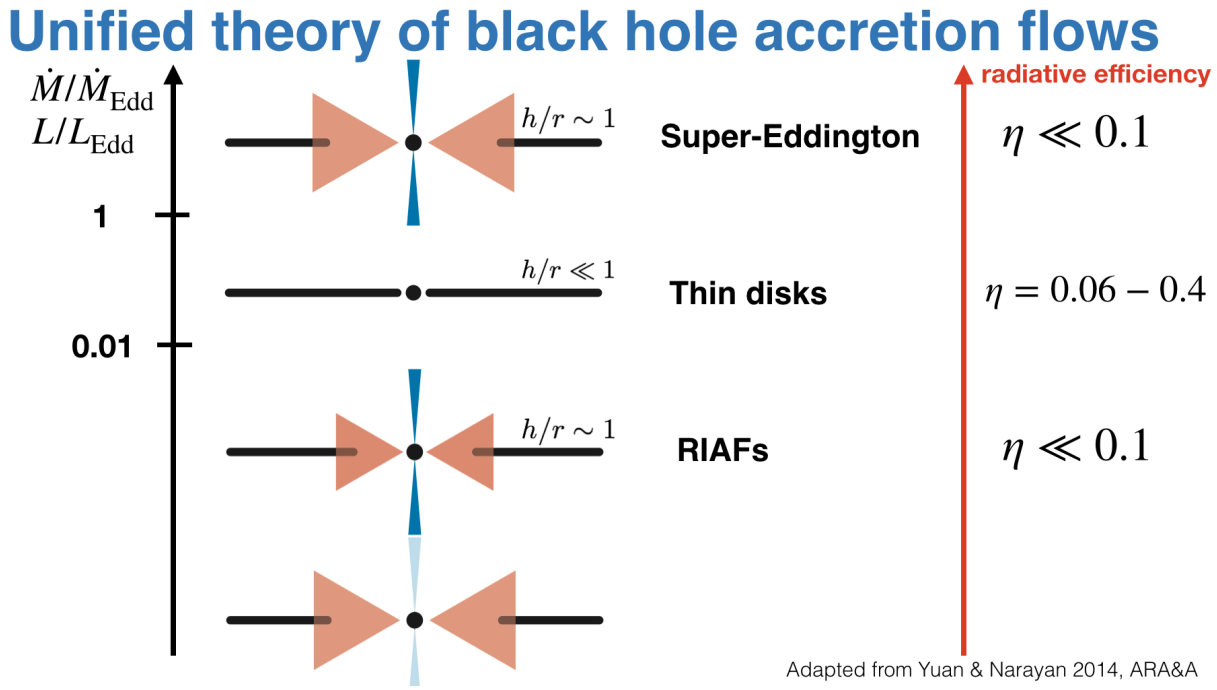

Figure 1.5: Scheme adapted from Yuan and Narayan (2014) showing the types of accretion discs in the function of the radiative efficiency parameter η and the mass accretion rate. The accretion rate determines the geometry of the accretion flow. Image edited by Rodrigo Nemmen.

If the efficiency is close to the unity ($\epsilon = 0.1 - 1$), the accretion disc becomes geometrically thin and radiatively efficient. Quasars of the distant universe are accreting gas at this rate. For the super-Eddington case, the accretion flow is geometrically thick, but this time supported by radiation pressure. Objects in the super-Eddington regime are rarer and transient.

1.6 Cold accretion flows

In a few words, accretion discs are rotating flows of fluid with viscous transport of angular momentum through the material (Yuan and Narayan, 2014). There are two types of accretion discs: cold and hot. The cold accretion flows are optically thick systems and can be *thin* or *slim discs* with temperatures between $10^4 - 10^7$K.

The thin disc was first presented in the seminal paper from Shakura and Sunyaev (1973). It quickly became one of the most influential works in the field. This accretion flow is geometrically thin, optically thick and thermally radiates like a blackbody – with some changes. The thin disc model can be applied to accretion flows close to the Eddington regime and reproduce very well the observed quasars. For more details, see Narayan et al.

(1997); Abramowicz and Fragile (2013).

The slim disc is a solution for the highest accretion rates when the accretion flows reach the super-Eddington regime. In this state, the disc's optical depth is too high to radiate the energy. The radiation becomes trapped inside the flow, inflating the accretion disc and being advected into the BH later. For more details, see Abramowicz et al. (1988); Ohsuga (2006).

1.7 Hot accretion flows

In this work, the focus is on the hot accretion flows in RIAF mode. The primary model described here can also be called ADAF (advection-dominated accretion flow). This accretion flow is dominated by advection, where the thermal energy cannot be irradiated away, is trapped inside the flow, and finally falls into the BH. (Ho, 2008; Abramowicz and Fragile, 2013; Blaes, 2014).

The hot accretion flows present much higher temperatures than their cold counterparts. The temperature is closer to the virial temperature and can be higher than 10^{10-11}K. This model has radiative emission that can be applied to understand the local universe AGN and the hard state of high-mass X-ray binaries.

Figure 1.6 from Nemmen et al. (2014) represents a low-luminosity AGN system, where there is a hot accretion flow in the region closer to the SMBH and an external thin disc. This figure illustrates very well the two types of accretion flows.

1.7.1 One-dimensional solution

Hot accretion flows can be studied as a steady axisymmetric flow and solved for a one-dimensional case. This example from Yuan and Narayan (2014) included integration over the disc height and the azimuthal angle. Conservation of mass, radial momentum, angular momentum, and energy are respectively described by the set of four equations (1.13) to (1.16).

$$\frac{d}{dR}(\rho R H v) = 0 \tag{1.13}$$

$$v\frac{dv}{dR} - \Omega^2 R = -\Omega_K^2 R - \frac{1}{\rho}\frac{d}{dR}(\rho c_s^2) \tag{1.14}$$

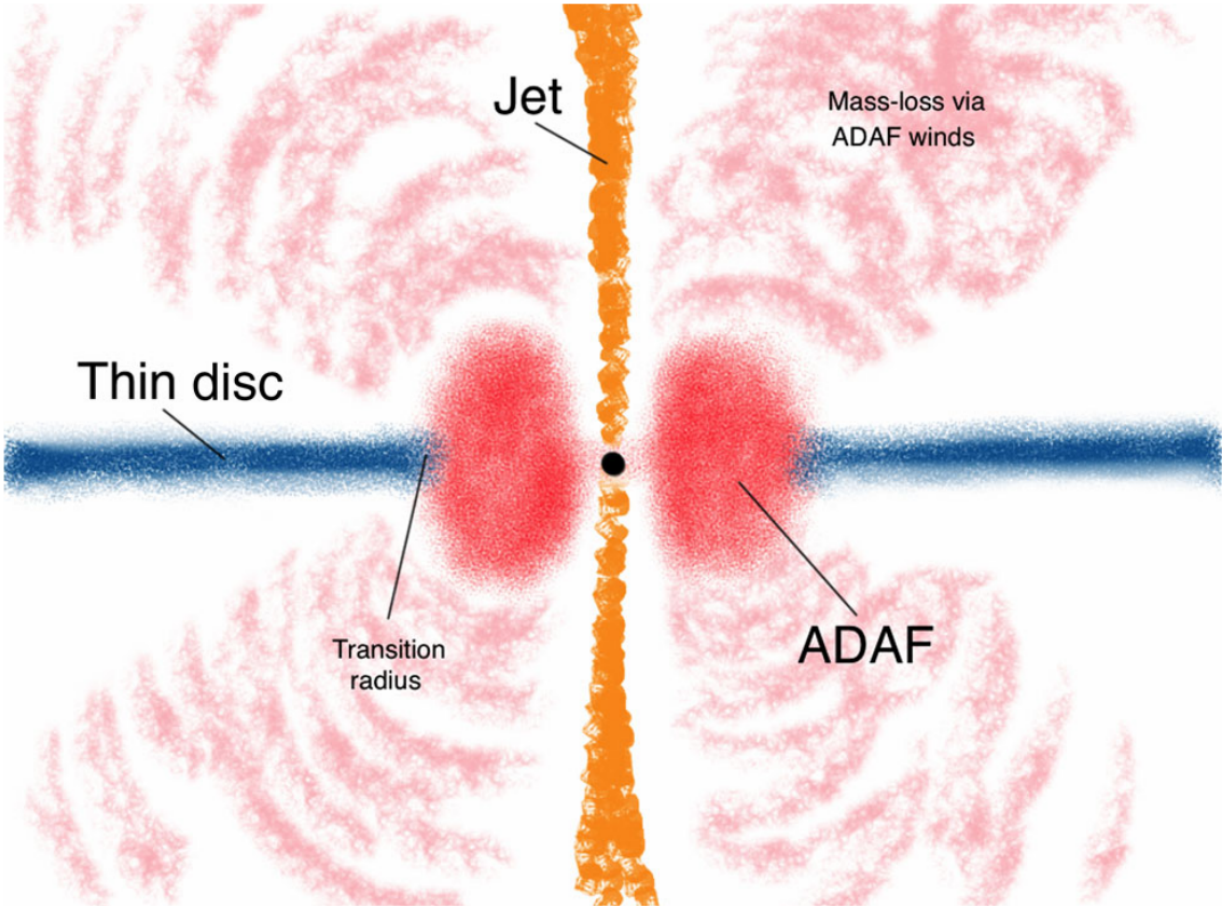

Figure 1.6: Representation of a Low-Luminosity AGN system from Nemmen et al. (2014). In the centre, there is a hot accretion flow in ADAF mode and an external thin disc in the system. Also, there is a representation of a possible relativistic jet coming out from the system.

$$v\frac{d(\Omega R^2}{dR} = \frac{1}{\rho R H}\frac{d}{dR}\left(\nu\rho R^3 H\frac{d\Omega}{dR}\right) \tag{1.15}$$

$$\rho v\left(\frac{de}{dR} - \frac{p}{\rho^2}\frac{d\rho}{dR}\right) = \rho\nu R^2\left(\frac{d\Omega}{dR}\right)^2 - q^- \tag{1.16}$$

For instance,

- ρ is the mid-plane density of the gas;
- R is the radius distance;
- H is the height estimative ($H \approx c_s/\Omega_K$);
- v is the radial velocity;
- Ω is the angular velocity;
- Ω_K is the keplerian angular velocity;
- $c_s = \sqrt{(P/\rho)}$ is the sound speed;
- P is the pressure;
- e is the specific internal energy;
- q^- is the radiative cooling rate per unit of volume;
- ν is the kinematic viscosity coefficient parameterized via the Shakura and Sunyaev (1973) as it is shown in equation (1.17).

$$\nu = \alpha c_s H = \alpha\frac{c_s^2}{\Omega_K},\ (\alpha = \text{cte}) \tag{1.17}$$

The model described through equations (1.13)-(1.16) is for an accretion flow without outflowing material. However, numerical simulations suggest consistent production of outflows from hot accretion flows (Narayan et al., 2012; Sądowski et al., 2013; Almeida and Nemmen, 2020). To take into account the produced outflow, it is useful to use the power-law approximation from Blandford and Begelman (1999) in equation (1.18) in addition to equation (1.13).

$$\dot{M}(R) = 4\pi\rho RH|v| = \dot{M}_{BH}\left(\frac{R}{R_S}\right)^s,\ R_S \leq R \leq R_{\rm out}. \tag{1.18}$$

$\dot{M}_{BH}$ is the accretion rate in the BH ($R = R_S$). The index s must be between 0-1, being $s = 0$ in the situation with no outflows. The limit $s < 1$ is due to energetic reasons. A common approximation is changing (1.13) with (1.18) and keeping the other three equations (1.14)-(1.16) unchanged.

Looking at equation (1.16) with more detail, it can be divided into two parts, the left-hand and right-hand sides. The left side is the change rate of internal energy and the work done by compression; these two terms correspond to the advective component $q^{\rm adv}$, and it can be related to an entropic flow. On the right-hand side, we had the cooling rate per unit of volume q^-, and the other component is the heating rate per unit of volume, which can be defined as q^+. Rewriting it:

$$q^{\rm adv} = q^+ + q^- = fq^+. \tag{1.19}$$

The parameter f measures the importance of advection in the system compared to the total released energy. Considering this parameterization, the energy fraction advected to the BH is f and the energy fraction radiated away is $1 - f$. For a thin disc, $f = 0$ and all energy is radiated away. For the slim disc and hot accretion flow, $f \to 1$, indicating advection dominates the system.

Narayan and Yi (1994, 1995) solved the equations (1.14)-(1.16) in a self-similar way, considering a Newtonian gravitational potential and f independent of radius and found a solution without outflows ($s = 0$). Adding outflows via equation (1.18) affects only the density profile and becomes approximately (Yuan et al., 2012; Yuan and Narayan, 2014)

$$v \approx -1.1 \times 10^5 \alpha r^{-0.5}\ [\mathrm{km\ s^{-1}}], \tag{1.20}$$

$$\Omega \approx 2.9 \times 10^4 m^{-1} r^{-1.5}\ [\mathrm{s^{-1}}], \tag{1.21}$$

$$c_s^2 \approx 1.4 \times 10^{10} \alpha r^{-1}\ [\mathrm{km^2\ s^{-2}}], \tag{1.22}$$

$$n_e \approx 6.3 \times 10^{19} \alpha^{-1} m^{-1} \dot{m}_{\rm BH} r^{-1.5+s}\ [\mathrm{cm^{-3}}], \tag{1.23}$$

$$B \approx 6.5 \times 10^{8}(1+\beta)^{-0.5}\alpha^{-0.5}m^{-0.5}\dot{m}_{\rm BH}^{0.5}r^{-1.25+s/2}\ [\rm G], \tag{1.24}$$

$$P \approx 1.7 \times 10^{16}\alpha^{-1}m^{-1}\dot{m}_{\rm BH}r^{-2.5+s}\ [\rm g\ cm^{-1}\ s^{-2}]. \tag{1.25}$$

Approximating the temperature value to

$$T \approx \frac{GMm_p}{6k_B R} \sim \frac{10^{12}}{r}\ [\rm K]. \tag{1.26}$$

Where the normalization for black hole mass, accretion rate and radius are

$$m \equiv \frac{M_{\rm BH}}{M_\odot},\ \dot{m}_{\rm BH} \equiv \frac{\dot{M}_{\rm BH}}{\dot{M}_{\rm Edd}},\ r \equiv \frac{R}{R_S}. \tag{1.27}$$

The parameter β is an indicative of the magnetic field strength as the ratio between the gas pressure $P_{\rm gas}$ and the magnetic pressure $P_{\rm mag} = B^2/8\pi$.

$$\beta \equiv \frac{P_{\rm gas}}{P_{\rm mag}}. \tag{1.28}$$

The obtained solution is the most simplified scenario possible. Still, it can offer powerful insights into the hot accretion flows physics. The ADAF solution describes an accretion flow for $\dot{m} \lesssim 10^{-4}$ and $f \approx 1$. From equations 1-1, many inferences can be made and compared to the cold accretion flows.

1. The temperature of the hot accretion flow is much hotter than the thin disc solution, being near the virial temperature.

2. The accretion disc is thick, with a height scale close to $H/R \sim 0.5$.

3. Radial velocity in the hot accretion flow is larger than in the cold one.

4. Angular velocity is sub-keplerian

5. The optical depth is below the unity, making the hot accretion flow optically thin and unable to irradiate blackbody-like radiation. The radiative processes most likely to happen inside the hot accretion flow are synchrotron, bremsstrahlung, and inverse Compton scattering.

6. Radiative efficiency is much lower than the typical 10% from the thin discs.

7. The high temperature makes the flow Bernoulli parameter Be positive, suggesting the production of strong outflows.

1.7.2 Two-temperature fluid

Beyond the most simple solution for the ADAF presented in subsection 1.7.1, it is common to analyze the flow thermodynamics considering different temperatures for the ions and electrons inside the accretion flow (Shapiro and Lightman, 1976). For this scenario, equation (1.16) is replaced by two intertwined equations (1.29) (Quataert and Narayan, 1999).

$$\begin{aligned} q^{\rm adv} &= q^{\rm adv,ion} + q^{\rm adv,eletron} = q_i^{\rm adv} + q_e^{\rm adv} \\ q_i^{\rm adv} &\equiv \rho v \left(\frac{de_i}{dR} - \frac{p_i}{\rho^2}\frac{d\rho}{dR} \right) = \rho v \frac{de_i}{dR} - q_i^{\rm compression} = (1-\delta)q^+ - q^{ie} \\ q_e^{\rm adv} &\equiv \rho v \left(\frac{de_e}{dR} - \frac{p_e}{\rho^2}\frac{d\rho}{dR} \right) = \rho v \frac{de_e}{dR} - q_e^{\rm compression} = \delta q^+ + q^{ie} - q^- \end{aligned} \tag{1.29}$$

Where $e_i = k_B T_i/(\gamma_i - 1)\mu_i m_p$ and $e_e = k_B T_e/(\gamma_e - 1)\mu_e m_e$ are the internal energies for ions and electrons per unit of mass of the gas. γ_i and γ_e are the adiabatic indices, and the subscript notation is applied to all other variables. q^{ie} is the energy transfer rate between ions and electrons via collisions. The expected cooling mechanism for the ions is transferring their thermal energy to the electronic population. However, this mechanism is inefficient for the low-density regime of hot accretion flows, leading to $q^{ie} \to 0$ (Yuan and Narayan, 2014). Finally, δ is a fraction of the viscously dissipated energy to heat the electronic population. At the same time, the fraction $1-\delta$ goes to the ions. δ is often considered a free parameter because constraining its effect is a theoretical challenge.

Note that in equations (1.29), the cooling term only appear in q_e^{adv}, it is because electrons can lose their energy much faster than ions due their smaller rest mass. Another important feature is how the energy is transformed, the gravitational energy is converted into heat via two main channels: the viscous heating q^+ and the compressional heating $q_{e,i}^{\rm compression}$.

The viscous heating is shared between ions and electrons by the fraction $\delta \sim 0.1 - 0.5$ –this value comes from many works on plasma theory and astrophysical observations (Quataert, 1998; Yuan et al., 2003; Sharma et al., 2007; Nemmen et al., 2014; Almeida et al., 2018). While the compressional heating (in adiabatic conditions) scales the temperature

as $T \propto \rho^{\gamma-1}$. Going back to the temperature profile (see equation (1.26), for $R \lesssim 100R_S$, the electronic population presents relativistic temperatures, while the ionic population does not. This difference makes the adiabatic index differ $\gamma^{NR} = 5/3$ and $\gamma^{R} = 4/3$, and summed to the inefficient heat exchange between ions and electrons, inducing the two-temperature scenario naturally.

1.7.3 Theoretical spectrum

The only way to compare the model described in the previous sections with the observations is by looking at the emitted light from the ADAF. The first step is numerically solving the equations (1.13)-(1.16) with the considerations mentioned above and taking into account the boundary conditions for the problem (Yuan et al., 2003). The solution presented in equations (1.20)-(1.26) only works in the middle of the accretion flow, being invalid in the closest regions to the BH – where a significant part of the radiation comes from.

The main free parameters to solve this equation are the BH mass M, BH mass accretion rate $\dot{M}_{\rm BH}$, the viscosity parameter α, magnetization parameter β, wind index s, electron heating parameter δ and the fraction of energy into electrons and magnetic field e_e, e_B. These parameters are essential in chapter 3.

With the equations and free parameters in hand, the radial distributions of velocity, angular momentum, density, and many others can be numerically computed. Considering the nature of the hot accretion flow as a magnetized optically thin gas, the main radiative processes occurring in the system are synchrotron, bremsstrahlung, and inverse Compton (IC) emission (Narayan and Yi, 1995; Yuan et al., 2003; Nemmen et al., 2014).

A brief summary of the hot accretion flow model electromagnetic emission features.

1. Around the first peak in the SED, the emission is dominated by a highly-absorbed synchrotron emission from a thermal population of electrons.

2. The synchrotron peak emission comes from the gas close to the BH, and the lower frequencies come from the gas at larger distances.

3. Synchrotron photons suffer comptonization and gain energies up to the thermal energy $kT_e \gtrsim 100$keV.

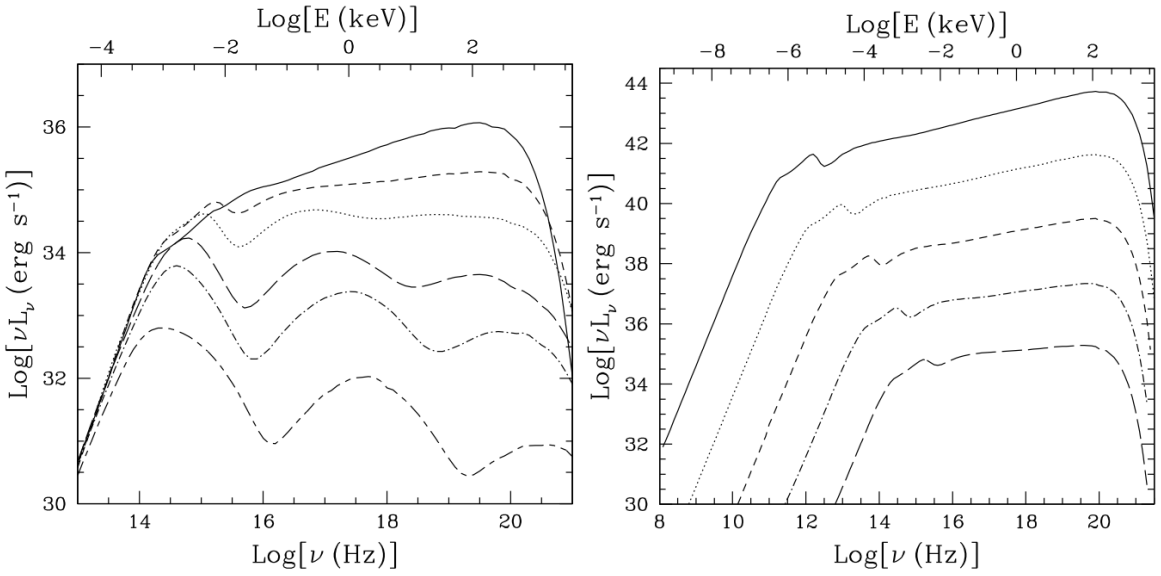

Figure 1: Model spectra of hot accretion flows for the following parameters: viscosity parameter $\alpha = 0.1$, magnetization parameter $\beta = 9$, electron heating parameter $\delta = 0.5$, wind parameter $s = 0.4$ (§§2.1, 2.2). *Left:* Spectra corresponding to a $10M_\odot$ black hole accreting with a mass accretion rate, from bottom to top, $\dot{m}_{\rm BH} = 8 \times 10^{-6}$, 5×10^{-5}, 1.6×10^{-4}, 8×10^{-4}, 2.4×10^{-3} and 5×10^{-3}, respectively. *Right:* Spectra corresponding to $\dot{m}_{\rm BH} = 2.4 \times 10^{-3}$ for black hole masses, from bottom to top, $M/M_\odot = 10$, 10^3, 10^5, 10^7 and 10^9, respectively. The model spectra shown here are for hot thermal accretion flows. When there is a cool outer disk beyond a transition radius, the spectrum has an additional thermal blackbody-like component (see Fig. 8). If there is a jet with non-thermal electrons, or if the hot flow itself has non-thermal particles, there is enhanced emission at radio and infrared wavelengths, and the prominent inverse Compton bumps shown here at low mass accretion rates are smoothed out to some degree (Figs. 6, 8). (Adapted from Narayan 1996, but with modern parameters.)

Figure 1.7: Figure extracted from Yuan and Narayan (2014) along the subtitles, showing different hot accretion flows SEDs for several parameters.

4. $\dot{m}$ is critical to the IC emission. For higher values of $\dot{m}$, the IC can be more dominant than the synchrotron emission. While for low $\dot{m}$, the IC can be dominated by the bremsstrahlung emission in the higher frequencies.

5. Inside the hot accretion flow, it is possible that proton-proton collisions create pions that will decay and emit γ-rays (Mahadevan et al., 1997).

6. Shocks and other effects in the accretion disc can produce a non-thermal population of particles responsible for the very-low energy part of the spectrum (Yuan et al., 2003; Almeida et al., 2018).

7. Hot accretion flows systems are prone to produce relativistic jets, making it sometimes harder to discern the origin of radio emission.

8. In some cases, a thin disc can be present at larger radius and add a typical thermal emission to the final SED.

1.7.4 Numerical simulations

The presented solution in subsection 1.7.1 is a simplified one-dimensional model that offers important insights into the hot accretion flows. However, it eliminated the three-dimensional structure and interesting features such as the outflow production and the zenithal distribution.

Solving the three-dimensional equations for hot accretion flows is not possible analytically and is a challenging task, even numerically. Many papers have been published about the topic in the last three decades, from works like HD simulations of Stone et al. (1999) to the highly optimized GRMHD simulations from Liska et al. (2018).

The numerical simulations will be treated in more detail in chapter 2.

1.7.5 Observations of hot accretion flows in nature

The hot accretion flows are in nature in the centre of the so-called low-luminosity AGN (LLAGN). While the bright distant quasars present the emission of a thin disc with $\dot{M} \lesssim \dot{M}_{\rm Edd}$, these low-luminosity AGN present emissions several orders of magnitude smaller and correspond to an underfed SMBH surrounded by a hot accretion flow.

This subsection will present a tiny list of widely studied LLAGN sources and their main characteristics.

Sagittarius A*

Sagittarius A* or simply SgrA* is the SMBH in the centre of Milky Way (Genzel and Cesarsky, 2000; Genzel et al., 2003; Ghez et al., 2005). The SMBH has a mass of approximately $4 \times 10^6 M_\odot$ and is distant to Earth by 8kpc (Gillessen et al., 2009; Akiyama et al., 2022a). Due to the source proximity, this is probably the most observed SMBH – including being one of the imaging targets of the EHT (Akiyama et al., 2022a) (see figure 1.8. Figure 1.9 shows the X-ray emission from SgrA*, this persistent and strong emission is one of the indicatives of the accreting SMBH presence.

This compact source has a persistent multiwavelength emission characterized by a hot accretion flow with an extremely low mass accretion rate of $\dot{M} \sim 10^{-6} \dot{M}_{\rm Edd}$ Genzel et al. (2010). Despite the current low accretion rate, there are pieces of evidence of past episodes of higher accretion Ponti et al. (2010).

With plenty of data, it is possible modelling the flow and model the source as an ADAF. Yuan et al. (2003) constrained SgrA* quiescent state as it is shown in figure 1.10. SgrA* can be well described by a thermal electronic population of electrons emitting synchrotron radiation that is posteriorly comptonized (dot-dashed line). Also, they used a population of non-thermal electrons to explain the low-energy radio emission (short-dashed line). A bremsstrahlung emission comes from electrons at a larger radius (long-dashed line).

M87*

M87* is the $6.5 \times 10^9 M_\odot$ Gebhardt et al. (2011) SMBH inside the M87– a massive galaxy in the centre of the Virgo cluster. M87* is famous for being the first BH imaged with the EHT (Akiyama et al., 2019a).

This SMBH is notorious for the presence of a large-scale relativistic jet, an expected feature of hot accretion flows around rotating BHs. For more detail about relativistic jets, see Tchekhovskoy et al. (2010). This source SED can be explained only considering the jet as it is shown in 3.4 in chapter 3.

Akira

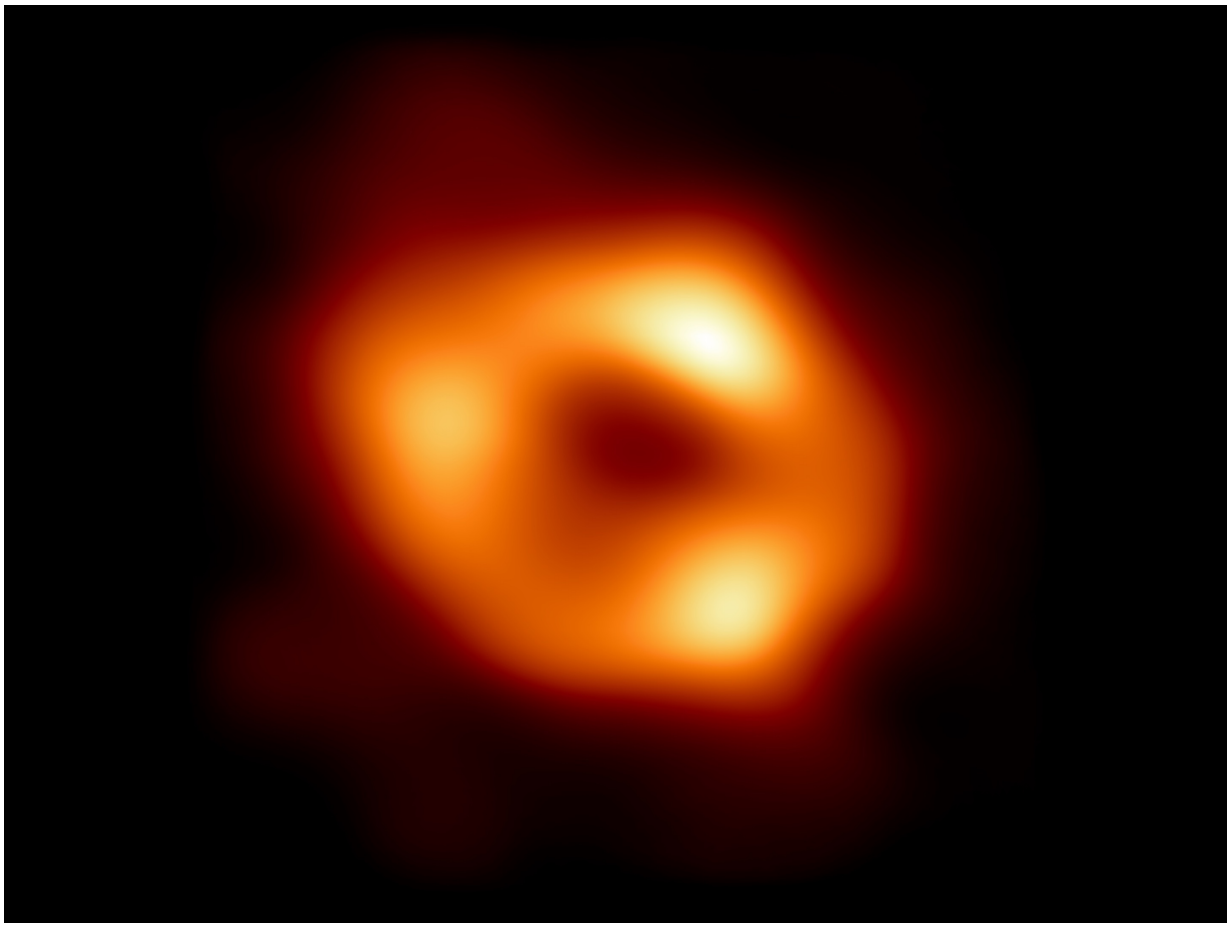

Figure 1.8: Milky Way's SMBH SgrA* imaged by Akiyama et al. (2022a). This BH presents a characteristic ADAF emission.

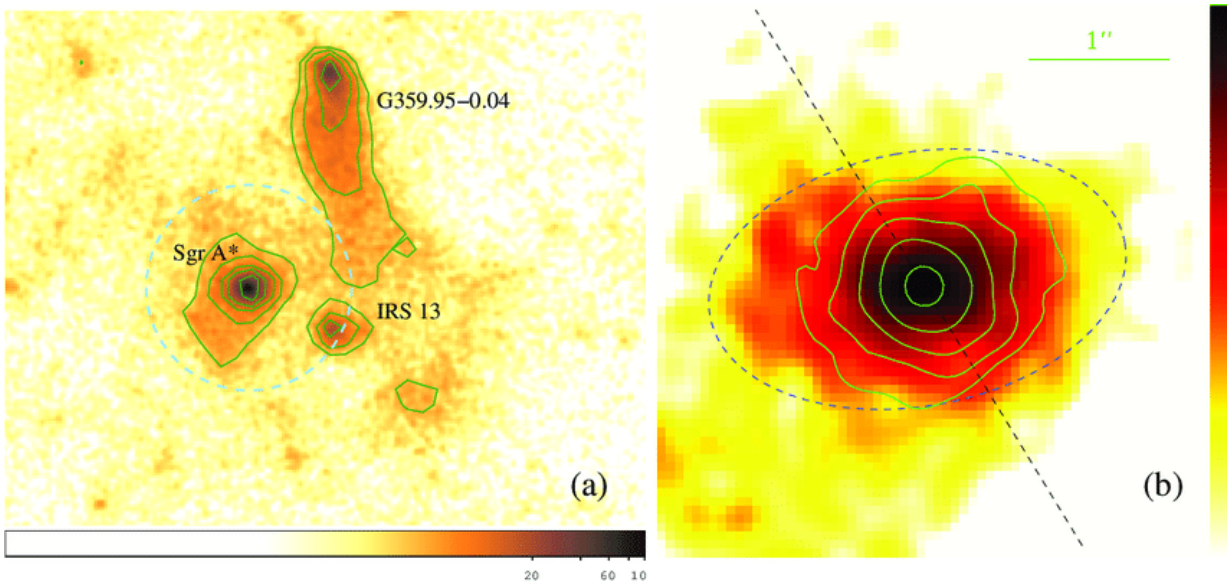

Figure 1.9: Extended X-ray emission from SgrA* region extracted from Wang et al. (2013). The left panel is a CHANDRA observation of the Milky Way central region. On the right, there is a zoom-in into SgrA* region.

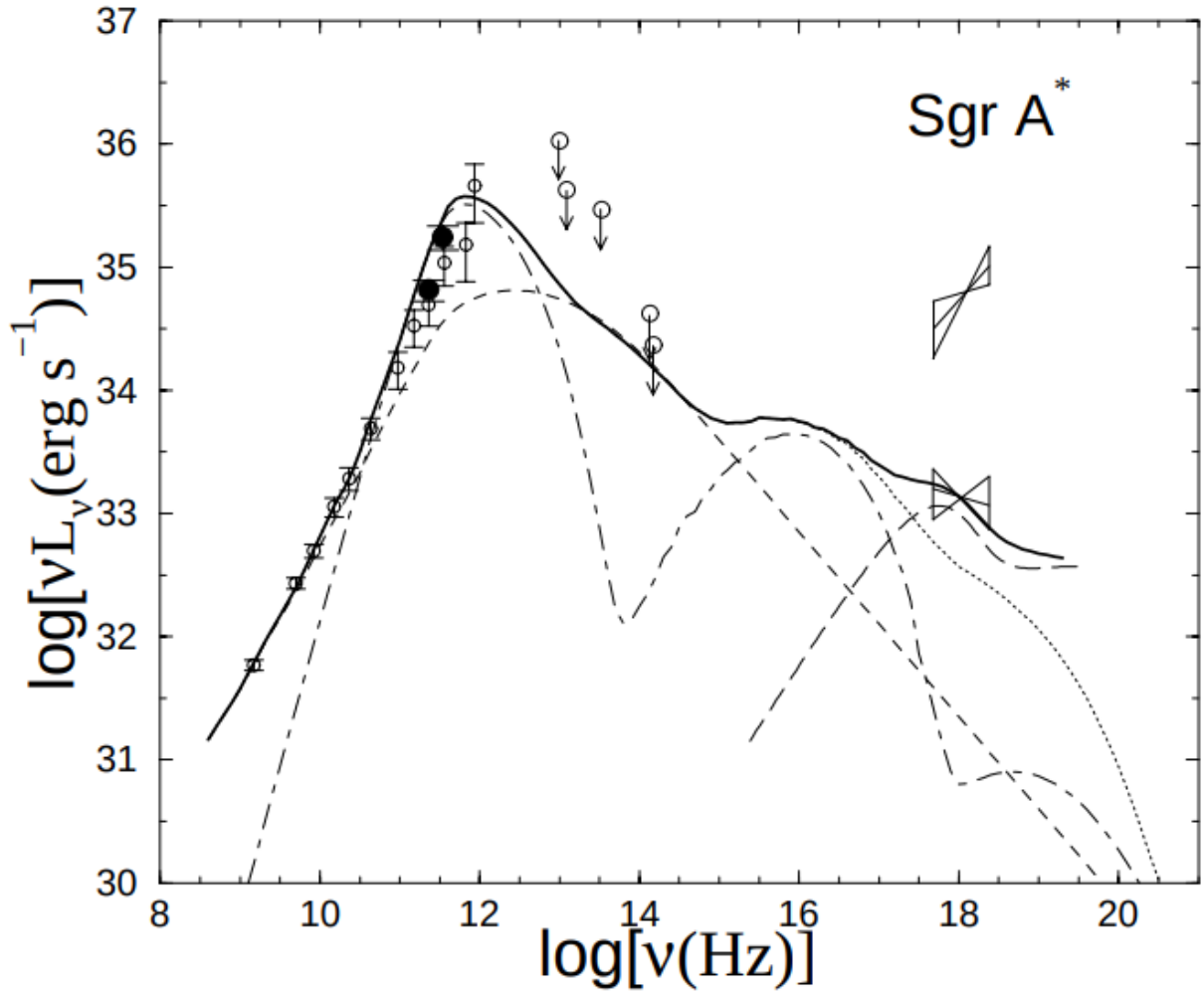

Figure 1.10: SED of SgrA* extracted from Yuan et al. (2003). The solid line is the fit for the quiescent mode, which considered an ADAF scenario dominated by a thermal population of hot electrons, with a small fraction of nonthermal electrons. The dot-dashed line is the synchrotron and inverse Compton emission by thermal electrons; the dashed line is the synchrotron emission by nonthermal electrons; The dotted line is the total synchrotron and inverse Compton emission (thermal and nonthermal); The long-dashed line is the bremsstrahlung emission from the outer parts of the RIAF; The solid line is the sum of all the components.

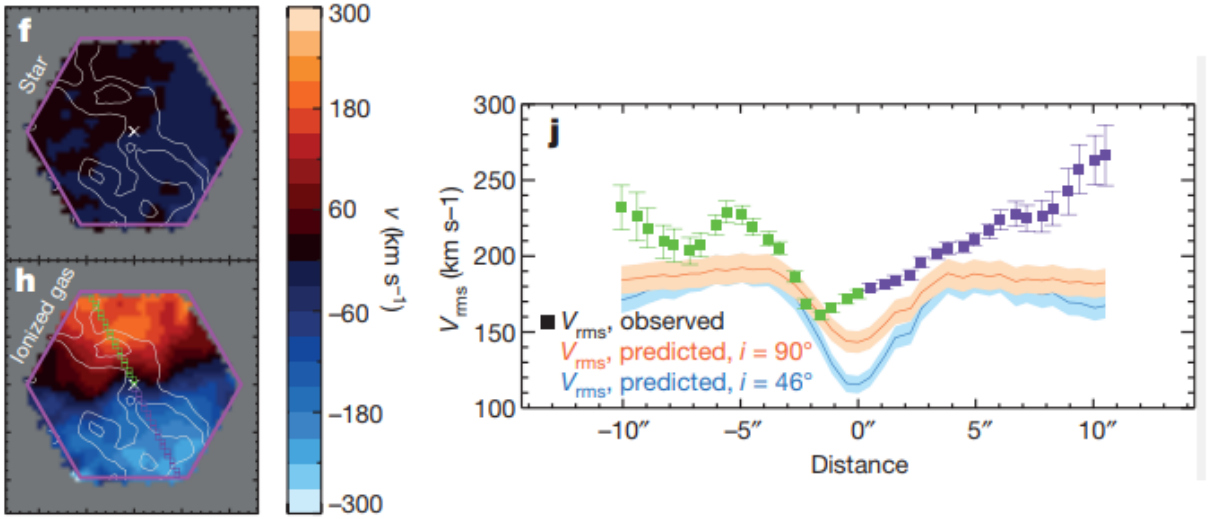

Figure 1.11: Observations of the ionized gas inside the galaxy Akira, extracted from Cheung et al. (2016). On the left side is the velocity map of the stars (top) and the ionized gas (bottom); the contour lines are the map of HII related to the gas. On the right side, models of the expected velocity considering only gravitational effects and inclination are presented in blue and pink. The data points in green and blue show the analyzed velocity excess.

Akira is a red galaxy studied in Cheung et al. (2016). The most surprising feature of this object is a velocity excess in the ionized gas in its interior. The velocity map of Akira is on the left side of figure 1.11. The velocity observations can not be explained only by typical gravitational effects, as shown on the same plot's right side.

Explaining this measurement involves the presence of subrelativistic and non-collimated outflow coming from the galaxy centre. These ejections resemble the winds expected to be launched from hot accretion flow (Yuan et al., 2015; Almeida and Nemmen, 2020). Galaxies with this pattern are called "red geysers" and have an essential role throughout this thesis. This topic is treated in chapter 4.

1.8 AGN feedback

The produced outflows from AGN accretion discs can be summarized in three main channels: radiation, winds and relativistic jet. All these energy injections can go outside the SMBH zone of influence and interact with the host galaxy gas and dust.

This interaction can lead to critical consequences for the interstellar medium, like expelling or heating the galactic gas. Lastly, this can impact the galaxy's star formation rate (SFR), quenching the production of newborn stars. At the same time, a diminution in the

SFR implies fewer stellar winds throughout the galaxy, which can suppress the gas supply to the accretion disc.

The crossed relation between AGN and environment – host galaxy and even the host galaxy cluster – is named "AGN feedback" and can account for the observed proportionality between the central black hole and host galaxy mass called as M-σ (Gebhardt et al., 2000; Kormendy and Ho, 2013). In figure 1.12 from Woo et al. (2019), the correlation between the stellar content of the galaxy and the SMBH mass indicates possible coevolution. The theoretical models (Silk and Rees, 1998; King, 2003) take into account the effect of quasar winds to explain the observational relation $M_{\mathrm{SMBH}} \propto \sigma^{5.1}$ (McConnell et al., 2011). The models cannot fully explain the slope and values but lead to powerful insights about the interaction between the AGN quasar phase and the stellar population.

The AGN feedback can be divided into two modes: radiative (or wind) and kinetic mode (Fabian, 2012). The radiative mode is linked to the quasar activity. It consists of the powerful winds and radiation field produced by the cold accretion flow interacting with the dust and gas of the galaxy. The radiative feedback is strongly related to the aforementioned M-σ relation to high-velocity galactic winds ($v \sim 1000 km/s$) (Rupke and Veilleux, 2011; Greene et al., 2012; Maiolino et al., 2012), the bimodal distribution of galaxies colour –blue star-forming and red quiescent galaxies– with the AGN feedback being a possible mechanism for the transition from blue to red (Fabian, 2012).

The kinetic mode is related to fainter AGN and jet activity. The kinetic mode can be linked to SMBHs surrounded by hot accretion flows. This mode is sometimes called "maintenance mode" because the previous quasar phase did a lot of transformations in the galaxy, like quenching the stellar formation. Observations show that the quasar activity-peak was around $z = 2-3$, and in the local universe we have a few of them (Ho, 2008), and the galaxies are still with low ongoing SFR. Something needs to keep the red galaxies red, preventing them from entering a new starbursting phase. A reasonable possibility is the effect of the AGN in this new mode, marked by the lower luminosity and kinetic feedback. Indeed, this possibility is better explored in chapter 4.

One of the most studied effects of the kinetic mode feedback is the impact of the BCG jet over the galaxy clusters (McNamara and Nulsen, 2007; Rafferty et al., 2006, 2008) – it can happen analogously in groups also. BCGs are giant galaxies in the centre of galactic clusters and are expected to receive strong gas infall. As the intracluster gas cools, it

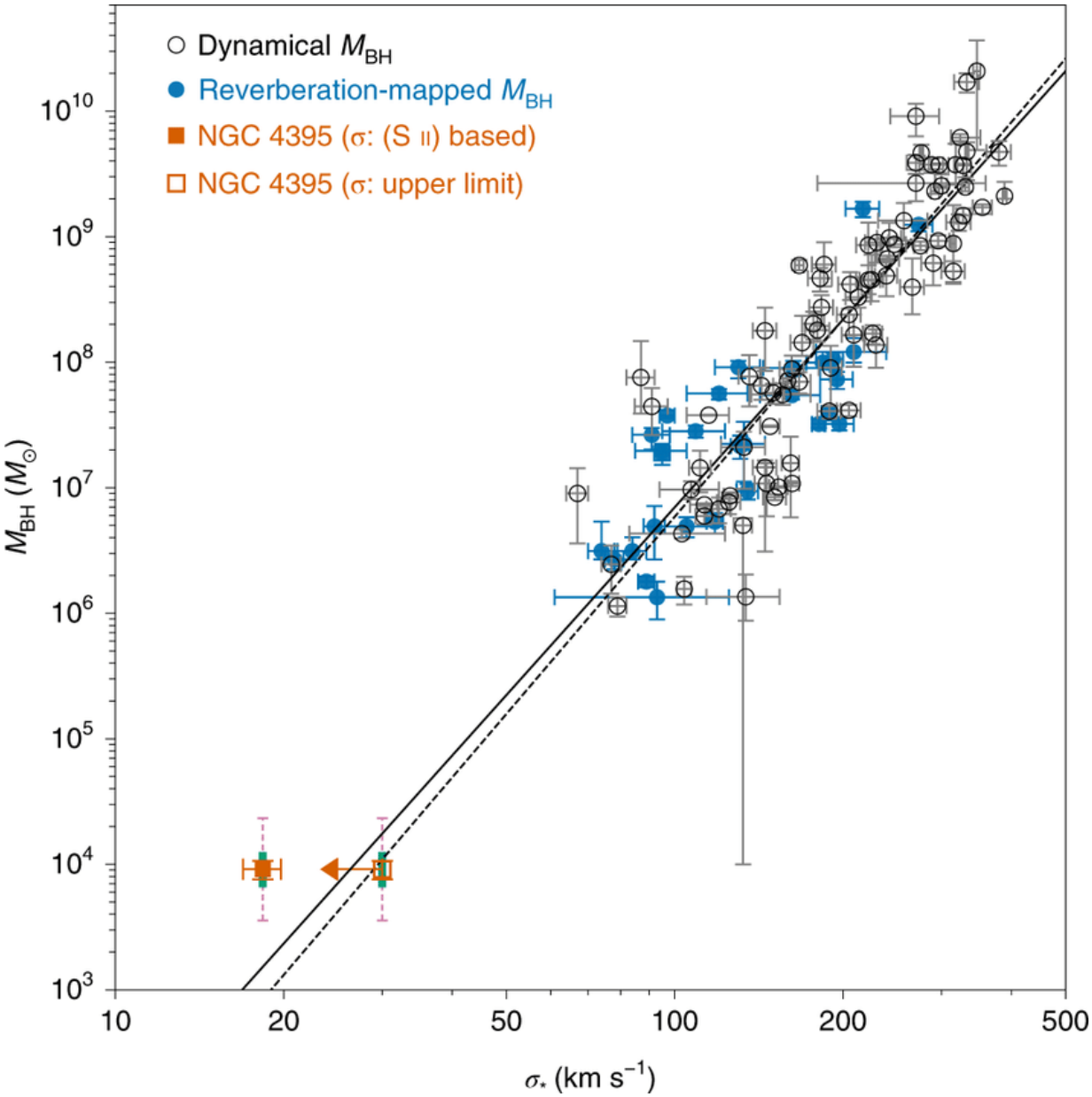

Figure 1.12: Image from Woo et al. (2019) showing the relation between the BH mass and the bulge stars velocity dispersion.

must agglomerate in the central region, where the BCG dwells. However, the observations pointed out that the BCG mass is below the expected from this "cooling flow" of gas. Something keeps the gas hot and prevents such high infalling mass rates. BCGs also present powerful jets, which are the key to keeping the gas hot and preventing the galaxy's overgrowing. Inside the galaxy cluster, it is possible to observe bubbles close to the BCG jet, indicating this energy deposit into the intracluster gas (McNamara et al., 2009).

The feedback mode of biggest interest in this thesis is related to the activity of "red geyser", firstly presented in section 1.7.5. The Akira galaxy reported by Cheung et al. (2016) is the prototypical galaxy of this group. Inside Akira, a large-scale subrelativistic wind (see figure 1.11) can be a source of potential feedback. In chapter 4, we present a more detailed calculation about the possible impact of LLAGN winds similar to Akira winds (Almeida and Nemmen, 2020) over the SFR of the galaxy. The idea is to estimate the effect of the winds over the galactic gas.

1.8.1 Thesis structure

This thesis revolves around three main works connected by hot accretion flows in an astrophysical context. We explore the topic and its potential to be an effective source of AGN feedback inside the host galaxy. These chapters are presented in a paper-like structure because some were published or submitted to MNRAS before this thesis.

In chapter 2, we present a set of GRMHD numerical simulations of hot accretion flow around a rotating SMBH. These simulations aim to constrain the physical mechanisms behind the production of outflows, mainly winds at accretion disc scales ($\lesssim$ 1pc). This work is a direct continuation of the previous work Almeida and Nemmen (2020). Chapter 4 presents a toy model for the galactic-scales winds triggered by an LLAGN like the prototypical galaxy Akira (Cheung et al., 2016). Chapter 3 is a Machine Learning method to calculate LLAGN SEDs, which is essential for constraining the theoretical models presented in the other chapters. In the last chapter 5, I give a compact overview of all works.

Chapter 2

GRMHD numerical simulations

2.1 Introduction

The universe's black holes (BH) are not isolated in a perfect vacuum. Falling material around a black hole forms a disk-like structure around it with a clear observational signature extending from radio to γ-rays. The angular momentum conservation and magnetic stresses inside the ionised plasma are the key to the system's physical properties called accretion flow (Balbus, 2003).

The magnetic stresses inside the accretion flow generate a large amount of thermal energy. How this energy can be radiated away is decisive for the accretion flow properties (Abramowicz and Fragile, 2013). Traditionally we parameterise the observed luminosity as a fraction of the total accreted energy as shown in equation (1.12). In our work, we focused on a system with values of $\dot{M} < 0.01\dot{M}_{Edd}$ – the features of hot accretion flows were discussed in section 1.7.

In the local universe, most AGN are much fainter than a typical quasar or Seyfert. These systems –inactive galaxies and low-luminosity LLAGNS– are underfed SMBH. We believe these systems are sub-Eddington ($\dot{M}_{BH} < 0.01\dot{M}_{\rm Edd}$) and hence in RIAF mode. The SMBH in the Milky Way centre, Sagittarius A* (Sgr A*) with $4 \times 10^6\, M_\odot$, is the most nearby example of a low accretion rate system (Narayan et al., 1995; Yuan et al., 2003; Akiyama et al., 2022b).

An accreting SMBH can affect the whole host galaxy; the energy released by the accretion flow can provide significant feedback even at the sub-Eddington mode. For example, in the centre of galaxy clusters, it was observed the effects of a powerful radio jet create bubbles in the intracluster gas, heating the environment and disallowing cooling (McNa-

mara and Nulsen, 2012). Moreover, there are pieces of evidence of AGN feedback inside individual galaxies without resolved radio jets. In this case, the feedback is provided by a non-collimated wind coming from the galactic centre. These systems are called "red geysers" where the winds carry out mechanical energy and heat the ambient. The hot wind interacts with the galactic cooler gas, suppressing the star formation inside the host galaxy (Cheung et al., 2016; Roy et al., 2018; Almeida et al., 2023).

Indeed, it has been argued that outflows from underfed SMBH accreting at RIAF mode –with mass accretion flow orders of magnitude below the Eddington mass accretion rate– can be essential to explain the observed nearby quiescent galaxies. These outflows can be directly responsible for quenching the star formation (Croton et al., 2006; Bower et al., 2017). Furthermore, one of the most significant results from the *Fermi* Large Area Telescope was the discovery of two giant bubbles over the Galactic plane (on both sides), the *Fermi* bubbles (Su et al., 2010). The bubble's origin is unknown; one possible scenario is that they were created in a past episode of Sgr A* activity. If Sgr A* was active once, it could eject material via powerful outflows for millions of years, generating the Bubbles (Guo and Mathews, 2012). The role of RIAFs in galactic evolution is relevant but not fully understood. More detailed studies are necessary to improve our knowledge about these systems, both observational and theoretical. Modelling feedback from its source is one of our main interests in this work.

The RIAF theory has significantly improved in the last three decades since it was proposed. The first works in the area derived a useful analytical one-dimensional solution for the RIAF equations (Narayan and Yi, 1994, 1995). These works suggest the possibility of material ejection from RIAFs, the aforementioned "winds". Years later, works like Blandford and Begelman (1999); Begelman (2012) proposed a power-law for the inflow mass rate as a power-law with index s (see equation (C.2)) The value of s is directly related to the outflow production. Lower values of s mean a reduction of the inflow mass rate and higher mass losses via outflows.

The early works paved the path to be followed and proved to be very handful. However, one-dimensional models are lacklustre in understanding the details of outflow production. Nonlinearities in the outflow production can not be reproduced with these models, numerical simulations are necessary to understand, and model accretion flows around SMBHs. The first hot accretion flow simulations were executed by (Stone et al., 1999; Igumenshchev

and Abramowicz, 1999, 2000) –their framework was purely hydrodynamic and Newtonian. Other works followed the same structure (Proga and Begelman, 2003; Yuan et al., 2012; Bu et al., 2016; Almeida and Nemmen, 2020), some of them reported winds supporting the scenario proposed by Blandford and Begelman (1999). In particular, Li et al. (2013); Bu and Gan (2018); Bu and Yang (2018) included a cooling mechanism in their work and found thermally-driven substantial winds.

The accreted gas in a RIAF is an extremely hot and magnetised plasma; a purely hydrodynamic simulation overlooks the importance of the magnetic field during accretion. The intrinsic nature of the BHs is relativistic; no Newtonian model can fully imitate it. Performing general relativistic magnetohydrodynamics (GRMHD) accretion flow simulations would be a natural improvement. Since then, several GRMHD simulations modelled RIAFs (De Villiers et al., 2003; Narayan et al., 2012; Tchekhovskoy et al., 2014; Yuan et al., 2015; Yang et al., 2021), these simulations showed the presence of two main outflowing channels:

- A relativistic and very collimated Poynting-flux dominated jets along the poles and,
- coronal matter-dominated nonrelativistic and non-collimated wind that only carries away a fraction of the jet energy.

The jets were thoroughly studied in many works (e.g. Tchekhovskoy et al. 2012; McKinney et al. 2012). The winds are also well studied in literature (e.g. Yuan et al. 2012, 2015; Yang et al. 2021), but their real effect and potential to affect the galaxy is still an open topic. Yuan et al. (2015) reanalysed the simulations from Narayan et al. (2012) and found the wind can carry away $\sim 1\%$ of the accreted rest-mass energy, we can define a parameter η_w as

$$\eta_w = \frac{L_{\rm wind}}{\dot{M}c^2} \tag{2.1}$$

like Yuan et al. (2015), another work with different setups found similar values for the wind power (e.g. Sądowski et al. 2013; Almeida and Nemmen 2020). The main interest in studying winds is because relativistic jets occur in only $\approx 10\%$ of AGNs (Kellermann et al., 1989), so they cannot explain the whole sample of galaxies with low-ongoing star formation. Moreover, the collimated nature of jets did not allow them to interact efficiently with the interstellar medium –we would see an extremely anisotropic star formation rates pattern in galaxies.

After the quick literature review presented, it is clear that the question of winds coming from LLAGNs –accreting in RIAF mode. We still have many open questions: Can the winds produced by underfed SMBHs provoke impactful feedback inside the host galaxy? Do they carry enough energy and momentum to heat up gas and quench star formation rate? Can these outflows, in a broad sense, impact the evolution of galaxies? These are the main general questions that this paper will address.

In this work, we performed multidimensional numerical simulations of hot accretion flows with accretion rates below $0.01\dot{M}_{\rm Edd}$. We did three-dimensional GRMHD simulations of RIAFs under the effect of a Kerr spacetime. We aimed to self-consistently investigate the formation and launching of winds from these systems. We want to characterise these winds and study the possible effects of AGN feedback generated by these outflows.

2.2 HD simulations

In Almeida and Nemmen (2020), we performed a set of hydrodynamical simulations of hot accretion flows trying to model the red geysers galaxies – like Akira (Cheung et al., 2016). In that work, we used the numerical code PLUTO (Mignone et al., 2007, 2012). We performed hydrodynamical simulations and explored different prescriptions of viscosity and angular momentum profiles for the initial thick accretion disc.

In these simulation, we found some interesting results. We found that winds are a generic characteristic of hot accretion flows. The simulations presented powerful thermal winds that can be a mechanism of feedback in LLAGNs without prominent jets. The three main conclusion of that work were

- HD numerical simulations with implemented viscosity can generate powerful winds, with $0.1 - 1\%$ of the accreted energy $\dot{M}c^2$.

- Winds cannot be steady across time, the outflow generation can have times of activity interleaved with non-activity, and winds can be generated as powerful bursts, too, depending on the accretion disc state.

- The ejected particle, analyzing the hole sample of the simulations, comes from the coronal region of the disc, $30^o \lesssim \theta \lesssim 60^o$, which agreed with the scenario in that the main body of the disc is dominated by inflow.

These results supported a deeper investigation of hot accretion flows and their outflows. The next step was increasing the complexity of the models and adding two essential features: magnetic fields and general relativity.

In accretion flows, magnetic fields play an essential role. The mechanism behind the angular momentum transfer is the magnetorotational instability (MRI) (Balbus, 2003). As the accretion disc rotates, it presents a differential rotation radial profile with decreasing angular momentum as the radius increases. As the fluid moves, it constantly suffers the effect of a natural Lorentz force. This force can disrupt the steady motion of the accretion disc and introduce turbulence.

The role of GR is imperative since we are dealing with BHs. The spacetime around a BH, mainly in the inner hundred gravitational radii, is unique and can create some unexpected physical events (see section 1.4).

2.3 General Relativistic Magnetohydrodynamics

The equations of GRMHD are the most suitable for the problem of BH accretion flows. However, this comes with a high computational cost to solve. Numerical methods are necessary if one wants to deal with systems that are not perfectly symmetric.

2.3.1 `H-AMR`

GRMHD codes have been extensively used to solve accretion flow problems in recent decades (Narayan et al., 2012; Sądowski et al., 2013; Yuan et al., 2015; Liska et al., 2018). For example, giant sets of GRMHD simulation were used in the EHT studies to help constrain the properties of the imaged SMBHs M87* and SgrA* (Mościbrodzka et al., 2014; Mościbrodzka, 2017; Akiyama et al., 2019a, 2022a).

One very influential code for solving GRMHD equations was `harm` – *high-accuracy relativistic magnetohydrodynamics* Gammie et al. (2003). `harm` is a GRMHD code that solves the plasma equations for an astrophysical fluid under the effect of a fixed curved spacetime – `harm` does not evolve the Einstein equations, only takes into account a fixed metric $g_{\mu\nu}$.

As time passed, `harm` gained many different versions. This work used the GPU-accelerated version of `harm` called `H-AMR` (Liska et al., 2018). `H-AMR` presents the same

‘Ã¨ssence”as its predecessor, but it has some striking differences. While `H-AMR` and most of its successors were written in `C`, `H-AMR` was written and `C` and in `CUDA` with many routines adapted to be run in GPUs instead of CPUs. The GPU implementation allowed a massive speed-up in the parallel calculations, drastically improving its computing power. I will not enter into the technical differences between `H-AMR` and `harm` because it is outside the scope of our work.

`harm` (and `H-AMR`) solves the GRMHD in a modified set of Kerr-Schild coordinates $[x_0, x_1, x_2, x_3]$ (equations (2.2)). This change introduces the two parameters R_0 e h_0 that can deform the numerical grid making it more populated in the equator and close to the BH. `H-AMR` also presents a dynamical grid that can change as the simulation evolves to improve resolution in the denser regions and decrease the number o cells in areas of no interest.

$$\begin{aligned} t_{KS} &= x_0 \\ r_{KS} &= R_0 + e^{x_1} \\ \theta_{KS} &= \pi x_2 + \frac{1}{2}(1 - h_0)\sin(2\pi x_2) \\ \phi_{KS} &= x_3 \end{aligned} \tag{2.2}$$

2.3.2 GRMHD equations

In this section, I will present the GRMHD equations. In the notation $c = G = 1$, greek indices represent the four-dimensional components, Latin indices stand for purely spatial components, $\eta_{\mu\nu} = (-+++)$ is the Minkowski's metric, all the repeated indices are summed considered the Einstein convention. A more detailed discussion of the equations can be found at Soares (2021); Mewes (2021).

First, we have mass conservation:

$$\frac{1}{\sqrt{-g}}\partial_\mu(\sqrt{-g}\rho u^\mu) = 0, \tag{2.3}$$

where ρ is the mass density, u is the four-velocity, ∇_μ is the covariant derivative operator, and $g = det(g_{\mu\nu})$.

Writing the stress-energy tensor split into the MHD and the electromagnetic components.

$$\begin{aligned} T^{\mu\nu}_{\text{fluid}} &= (\rho + u + p)u^\mu u^\nu + pg^{\mu\nu}, \\ T^{\mu\nu}_{\text{EM}} &= F^{\mu\alpha}F^\nu_\alpha - \frac{1}{4}g^{\mu\nu}F^{\alpha\beta}F_{\alpha\beta}. \end{aligned} \tag{2.4}$$

Being u the internal energy, p the pressure, and the electromagnetic tensor $F^{\mu\nu}$ is

$$\begin{pmatrix} 0 & E_x & E_y & E_z \\ -E_x & 0 & B_z & -B_y \\ -E_y & -B_z & 0 & B_x \\ -E_z & B_y & -B_x & 0 \end{pmatrix} \tag{2.5}$$

The equation of state that relates pressure and internal energy

$$p = (1 - \gamma)u. \tag{2.6}$$

γ is the adiabatic index. In this work $\gamma = 13/9$, corresponding to a population of relativistic electrons and non-relativistic ions.

Relating the eletromagnetic tensor shown in equation (2.5) to a four-vector magnetic field through the relation from Komissarov (1999), we got equation (2.8)

$$\begin{aligned} b^t &= B^i u^\mu g_{i\mu} \\ b^i &= \frac{B^i + b^t u^i}{b^t} \end{aligned} \tag{2.7}$$

$$T^{\mu\nu}_{\text{EM}} = b^2 u^\mu u^\nu - b^\mu b^\nu + \frac{1}{2}b^2 g^{\mu\nu}. \tag{2.8}$$

Writing the MHD stress-energy tensor as the sum of the fluid and electromagnetic components

$$T^{\mu\nu}_{\text{MHD}} = T^{\mu\nu}(\rho + u + p + b^2)u^\mu u^\nu + \left(p + \frac{b^2}{2}\right) g^{\mu\nu} - b^\mu b^\nu \tag{2.9}$$

The stress-energy tension must be conserved

$$\nabla_\mu T^\mu_\nu = 0. \tag{2.10}$$

Another equation is the magnetic induction represented in equation (2.11).

$$\frac{1}{\sqrt{-g}}\partial_i(\sqrt{-g}\ B^i) = 0 \tag{2.11}$$

2.4 Numerical methods

In this section, I will briefly outline the numerical methods behind the code `H-AMR` . `H-AMR` solves the GRMHD presented in previous sections using the Godunov scheme (Godunov and Bohachevsky, 1959), for more details see the Appendice B. The equations are written in the generic form

$$\frac{\partial \mathbf{U}}{\partial t} + \frac{\partial \mathbf{F}(\mathbf{U})}{\partial x^i} = 0 \tag{2.12}$$

and solved in a discretized grid through the finite volumes method. Where $\mathbf{U}$ is the set of conserved variables

$$\mathbf{U} = (\rho u^t, T^t_t, T^t_i, B^i)\sqrt{g}. \tag{2.13}$$

$\mathbf{U}$ is directly related to the set o primitive variables $\mathbf{P}$

$$\mathbf{P} = (\rho, u, v^i, B^i). \tag{2.14}$$

The quantities expressed in equation (2.14) are constantly updated using the fluxes $\mathbf{F}(\mathbf{U}(\mathbf{P}))$ as it is shown in equation (2.12). $\mathbf{F}$ is calculated with an HLL flux (Harten et al., 1983) in the numerical cell boundary – see Appendix B. Summarizing, equation (2.12) means the temporal variation of a conserved quantity is equal to the flux outwards (or inwards) – in `H-AMR` , this is calculated on the numerical cells.

For the numerical solution, boundary conditions are essential. `H-AMR` uses a method called "*ghost cells*". This approach adds fictitious cells to the outer side of the innermost and outermost cells. These fictitious cells have a defined average value for the primitive variables and allow the code to calculate the interested quantities in the boundary cells solving the proper equations for the innermost and outermost cells of the grid.

Moreover, when integrating the equation (2.12), sometimes the code finds negative values for quantities like density or internal energy, which makes no physical sense. When something like this happens, the code assumes a minimum value –very close to zero– called the *floor value*. This is a numerical manoeuvre and slightly adds energy and mass to the system when it happens. It is worth saying that `H-AMR` automatically tries to control the numerical error at a minimum.

2.5 Simulations overview

2.5.1 Initial conditions

Our initial condition consists of a rotating torus in dynamical equilibrium with a specific angular momentum profile $l(R)$ following the same as Fishbone and Moncrief (1976). The torus' inner edge is at $R_{\rm in} = 20 - 30R_G$ depending on the simulation and outer edge $R_{\rm out} \approx 500R_G$. The radius of maximum density R_0 was varied in our models in the range $R_0 = 2R_{\rm in}$. Higher values of $R_{\rm in}$ led to a thicker torus and a more extensive gas reservoir. Our torus is pretty large–larger than most simulations which usually begin with a torus ending at $\approx 40R_S$ (e.g., Mościbrodzka and Falcke 2013; Porth et al. 2017)–since we are interested in both the density profile up to larger scales and whether winds are launched from a range of scales on the disk.

In this work we defined the total torus mass M_0 as $M_0 = \int \rho(\mathbf{x}, t = 0)dV$, with the following normalization: $\max(\rho) = 1$. We neglected any effects from torus self-gravity in our system since $M_{\rm BH} \gg M_0$.

Regarding the computational domain, we used a fixed mesh. Our grid extends to a large radius, 10^4R_G–which is one order of magnitude larger than the outer radius of the disc size–to avoid undesirable boundary effects. Our grid is uniformly distributed in $\log_{10}$(radius) with 512 cells; as such, the inner regions have a higher resolution. The radius of the computational domain begins at approximately $0.87R_G$. We adopted the outflow boundary condition at the inner and outer radii.

In the zenithal angle θ, we set 128 cells uniformly spaced from 0 to π. And in the azimuthal angle ϕ, there were 64 cells uniformly spaced from 0 to 2π.

The initial magnetic field was set in the way the potential vector $|\vec{A}|$ follow the density profile, with a constant

$$\beta = \frac{P_{\rm gas}}{P_{\rm mag}} = 20 \text{ or } 100, \tag{2.15}$$

depending on the simulation.

We also defined an inclination angle (i) between the BH spin vector and the disc angular momentum, the possible values were $i = 0^o$ or 45^o.

We performed a total of 6 simulations exploring the variation of three main properties of the system: spin (a), magnetic strength (β), inclination angle (i), and the gas reservoir

($R_{\rm in}$). The parameter space of simulations is summarized in Table 2.5.1. It is important to investigate different reservoir sizes since the actual profile in nature is not known. In particular, we do not know the initial conditions of SMBH accretion in low-luminosity AGNs, and the long-term evolution of the accretion flow and possible winds could be dependent on these initial conditions.

Sim ID	a	β	$R_{\rm in}$	$\vec{A} \propto$	Inclination angle
gb20a0	0	20	30	$\rho R^3 \sin^3\theta$	45^o
gb20a9	0.9375	20	30	$\rho R^3 \sin^3\theta$	45^o
ib20a0	0	20	20	$\rho R^3 \sin^3\theta$	45^o
ib20a9	0.9375	20	20	$\rho R^3 \sin^3\theta$	45^o
jb20a9	0.9375	20	25	$\rho R^3 \sin^3\theta$	45^o
jb100a9	0.9375	100	25	$\rho R^3 \sin^3\theta$	45^o
lb100a0	0	100	20	$\rho R^3 \sin^3\theta\ e^{-R/400}$	0^o
mb20a0	0	20	20	ρ	0^o
mb20a9	0.9375	20	20	ρ	0^o
nb20a9	0.9375	20	20	$\rho^2 R^5$	0^o

Table 2.1 - Set of simulations and their initial parameters.

The other two parameters–a and β–are responsible for the spacetime geommetry — if it is an highly rotating Kerr BH or a non-rotating Schwarzschild BH. We were binary in the choices of a, being 0 or 0.9375, not exploring a plenty of values because of the computational cost and only comparing a case with rotation or not – which can be understand to a comparison about the impact of a relativistic jet over the wind production. We expect the long-term behavior of the flow to depend on the β, since it is directly related to the magnetic energy available. Moreover, β regulates the strength of the angular momentum removal, since we need the magnetic field to existe the MRI.

To validate if the magnetorotational instability (MRI) is resolved we calculate the parameters

$$Q_\theta = \frac{2\pi}{\Omega dx^\theta}\frac{|b^\theta|}{\sqrt{4\pi\rho}},\ Q_\phi = \frac{2\pi}{\Omega dx^\phi}\frac{|b^\phi|}{\sqrt{4\pi\rho}} \tag{2.16}$$

where dx is the grid cell size and Ω is the angular velocity. For our runs, the gas inside $r = 100$M presented $Q_\theta,\ Q_\phi \geq 20$.

We ran the simulations for a long time–comparable to the viscous time at large radii in the disc–in the hopes that a considerable part of the accretion flow converges. The

individual duration of each model was different based on the numerical development of the simulation.

2.5.2 Lagrangian particle tracking

One technique that we used to identify and characterize outflows–in addition to analyzing the evolution of the mass and energy fluxes across our mesh-based simulations–was to introduce "tracer" particles which are passively advected with the fluid flow and thereby track its Lagrangian evolution, allowing the thermodynamical history of individual fluid elements to be recorded. This technique is called Lagrangian particle tracking and has been used to make sense of several astrophysical simulations (e.g. (Enßlin and Brüggen, 2002; Dubois et al., 2012; Genel et al., 2013; Yuan et al., 2015)). It is advantageous in our simulations since it sums the information previously obtained with the Bernoulli parameter, which is an indirect way of assessing whether outflows were produced, therefore being a more appropriate outflow measure.

We implemented the traditional scheme where the tracer particles are massless particles advected in space using the local velocity field (Harlow and Welch, 1965). To obtain the trajectories of the particles, we did the same procedure as in Almeida and Nemmen (2020). With the velocities from simulation data at a particular time t, we can advance the position of the tracer particle to $t+\Delta t$, which is accurate to first-order, limited by the time resolution of the simulation.

The simulations' time step Δt was chosen to be sufficiently short–approximately the orbital Keplerian period t_K at $R \approx 16R_G$–such that the distance a fluid element can cover over a timescale t_K is much smaller than the size of the disc, $v\Delta t \ll R_{\rm out}$ where in this context v is a typical fluid velocity.

To assess whether outflows are produced from a given simulation and–in case of an outflow–to quantify its properties, we used a set of 5000 tracer particles. We started the particle tracking at the moment when the fluid has reached a stationary net mass accretion rate, i.e. when the value of $\dot{M}_{\rm acc}(R = R_{\rm BH}, t)$

$$\dot{M}_{\rm acc}(R,t) = \oint_{\theta,\phi} \rho u^r dA_{\theta,\phi} \tag{2.17}$$

becomes roughly constant; which is usually around 5000M. The particles were initially randomly distributed in the space delimited by the ranges: $R < 100$M. For $t > 5000$M,

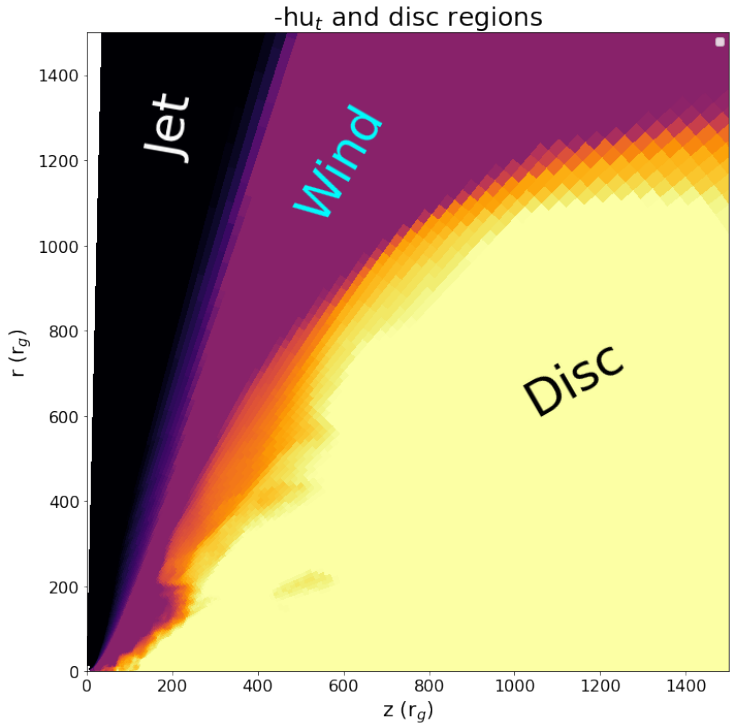

Figure 2.1: Disc regions following the $-hu_t$ criteria from equation (2.18). This is a plot from simulation `gb20a9` averaged between $t = 40000 - 50000$M.

we let the particles be advected by the flow and monitored their positions with time until $t \sim 50000$M.

In this work, we adopted two criteria for identifying whether a tracer particle is part of an outflow based on the $-hu^t$ value (Sądowski et al., 2013), being

$$-hu^t = -\left(1 + \gamma\frac{U}{\rho}\right)u^t \rightarrow \begin{cases} -hu^t \leq 1 & \text{bounded} \\ 1 < -hu^t < 1.02 & \text{wind outflow} \\ -hu^t \geq 1.02 & \text{jet outflow.} \end{cases} \tag{2.18}$$

This division works similarly to the angular division in Almeida and Nemmen (2020), even if it does not consider the angle θ in the definition as it is shown in figure 2.1. The jet outflow zone is roughly delimited in the cone $\theta \lesssim 15^o$ for the case with non-zero spin – when $a = 0$ most of the produced outflows fall into the wind category.

We also look into the particle's final velocity, whether positive or negative and to the ratio $R_{\text{final}}/R_{\text{initial}}$, which indicates how much the particle was ejected compared to its original position.

Figure 2.2 shows an example of the particle trajectories. This set of circuits is from the

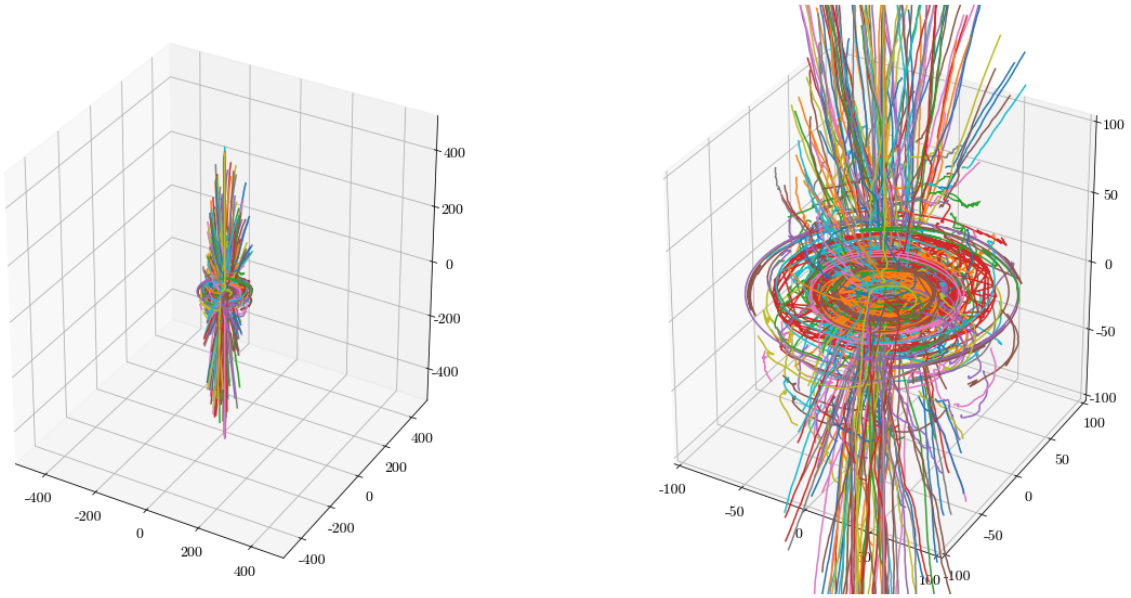

Figure 2.2: The 3D representation of the tracer particles' trajectories analyzed for simulation `ib20a9`. A prominent jet structure and the accretion spiral can be easily saw.

model simulation `ib20a9`. In the figure, the jet-like structure is apparent. In the equatorial zone, the spiral movement traced by the accreted particles can also be seen.

2.6 Simulations results

2.6.1 Accretion flow properties

Figures 2.3-2.4 show snapshots of the density maps of all our models –averaged between $\sim 45000 - 50000$M. Models like `ib20a0` and `nb100a9` presented a diffused distribution of the gas, while `nb20a9` presented a clear empty jet structure. Simulations like `jb100a9` also show a jet hidden during the average process. The simulations with $i = 45^o$ alternated moments of presence and absence of an empty jet's cone and the disc structure is irregular – the comparation of `gb20a9` and `nb20a9` is an example. Sometimes the gas "invaded" the jet zone, and later it was expelled – maybe this could become some blob structure at larger scales. Still, we can not make any strong affirmation about it. The panel has a size of 500M x 500M, roughly the size of the original accretion torus. All panels show the disruption of the original torus, and the velocity lines indicate a constant ejection outwards in regions with $\theta \lesssim 45^o$ and $R \gtrsim 200$M.

Following Stone et al. (1999), we defined the accretion rate as the flux of material through a surface of radius r. We denoted $\dot{M}_{\rm in}$ the mass *inflow* rate and $\dot{M}_{\rm out}$ the mass

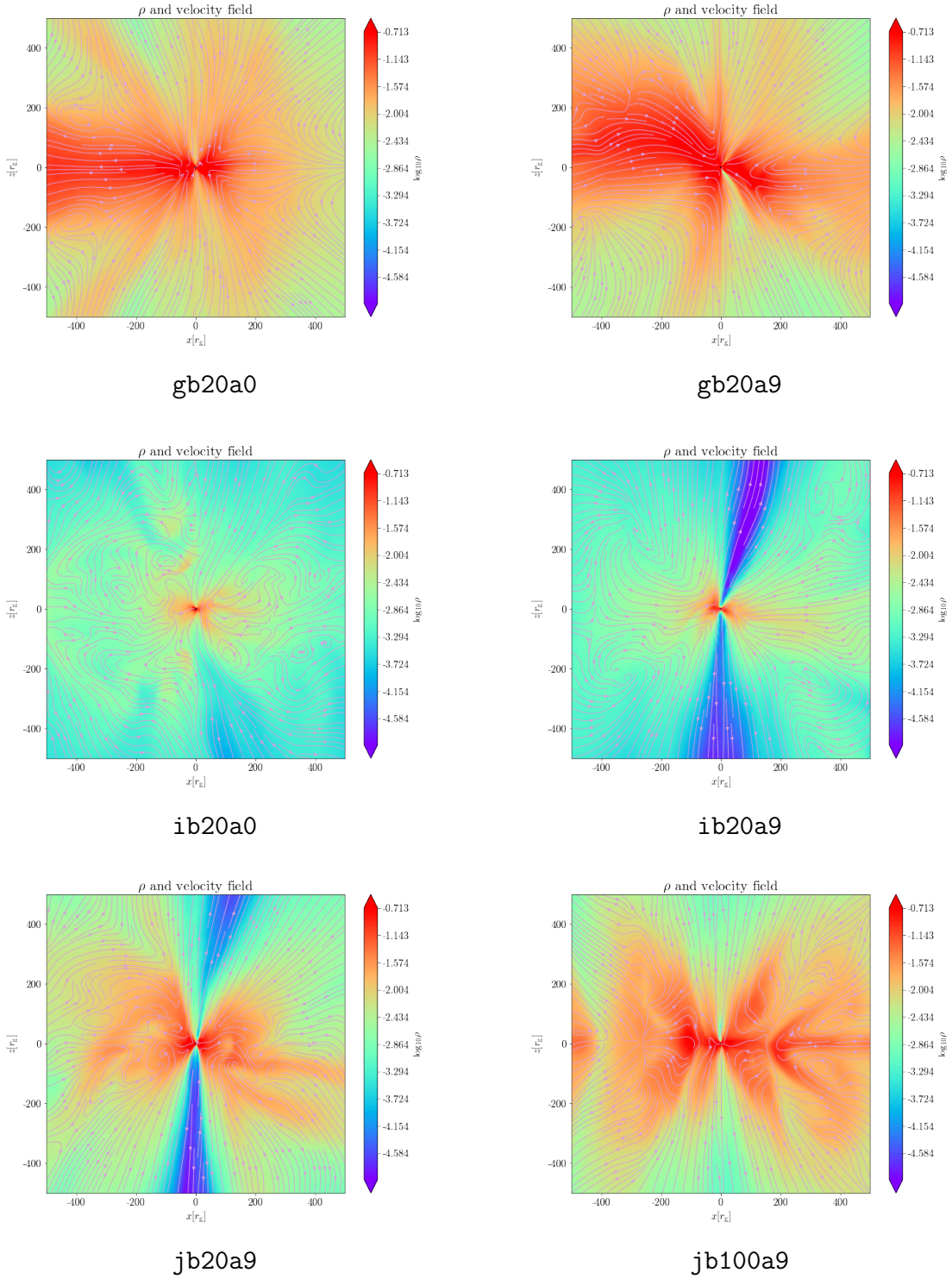

Figure 2.3: Plots showing the density map and velocity field for the simulations. These maps were averaged on time between 45000 GM/c^3 and 50000 GM/c^3.

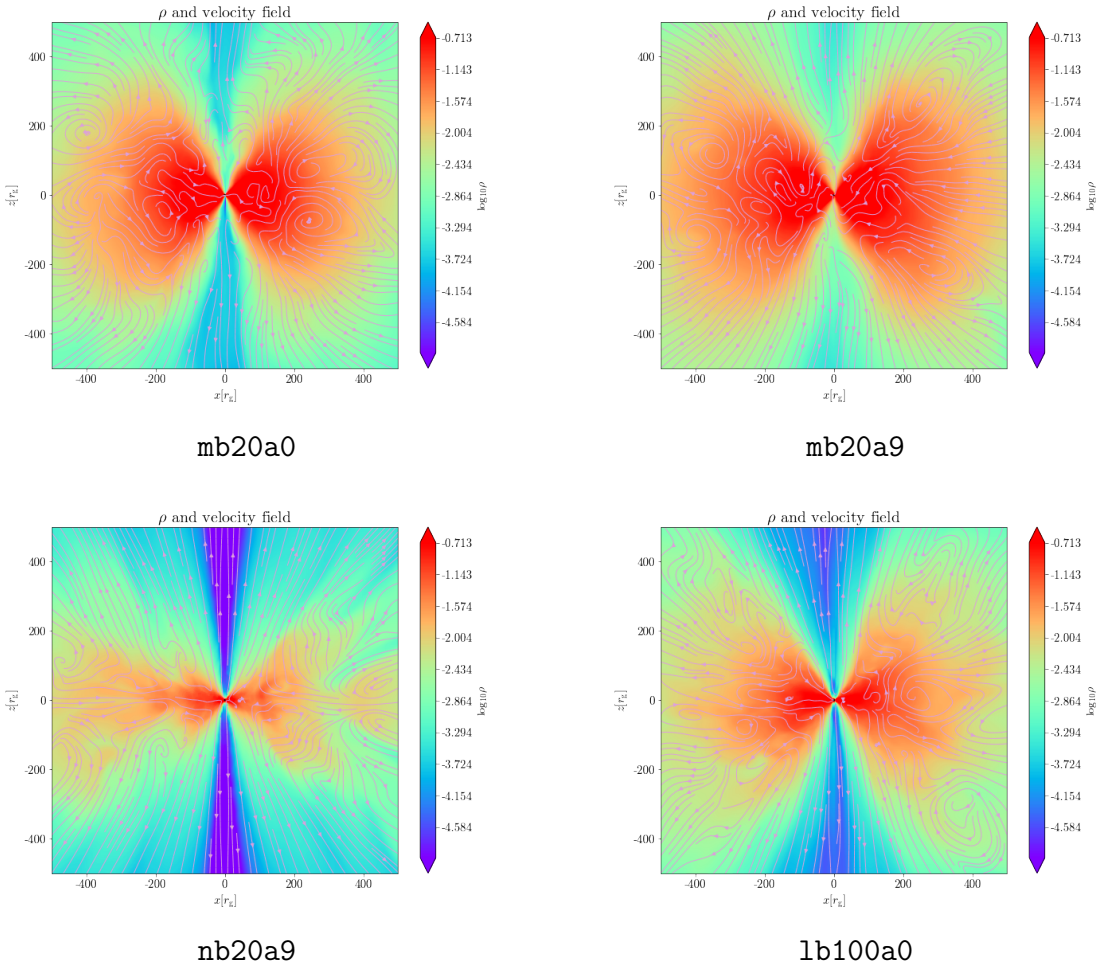

Figure 2.4: Continuation of figure 2.3.

outflow rate, which are defined as

$$\dot{M}_{\rm acc}(R,t) = \oint_{\theta,\phi} \rho \, \min(u^r, 0) dA_{\theta,\phi} \tag{2.19}$$

$$\dot{M}_{\rm acc}(R,t) = \oint_{\theta,\phi} \rho \, \max(u^r, 0) dA_{\theta,\phi} \tag{2.20}$$

The net mass accretion rate is

$$\dot{M}_{\rm acc} = \dot{M}_{\rm in} + \dot{M}_{\rm out}. \tag{2.21}$$

We also calculated the magnetic field flux at the BH horizon as (Narayan et al., 2012; Sądowski et al., 2013).

$$\Phi_{\rm BH}(t) = \frac{1}{2\sqrt{\dot{M}(r_H)}} \int_\theta \int_\phi |B^r(r_H,t)| dA_{\theta\phi}. \tag{2.22}$$

where r_H is the event horizon. The plots of $\dot{M}_{\rm acc}(t)$ and $\Phi_{\rm BH}(t)$ for the simulation set are shown in figures 2.5-2.6.

They show the net mass accretion rate calculated at 2M (black lines and values in the left y-axis) in code units –posteriorly, we can designate a physical value for the accretion rate. Still, at the moment, this is a "*free parameter*". Each figure represents a different simulation and it is not clear the differences in the mass accretion rate; for instance, if we look at the magnetic flux Φ_B (red lines and values in the right y-axis), the decrease after $t \sim 40000$M is more relevant for simulations with lower values of $R_{\rm in}$. Keeping $\Phi_B \gtrsim 30$ –i.e. a MAD (magnetically arrested disc) state Narayan et al. (2012); Tchekhovskoy et al. (2014)– for a long time was a challenging task in our models.

2.6.2 Wind properties

Following Sądowski et al. (2013), we define the total energy flux as

$$\dot{e}_{\rm tot} = -T^r_t, \tag{2.23}$$

being T^r_t a component from the MHD stress tensor (2.9)

$$T^r_t = (\rho + \gamma u + b^2) u^r u_t - b^r b_t. \tag{2.24}$$

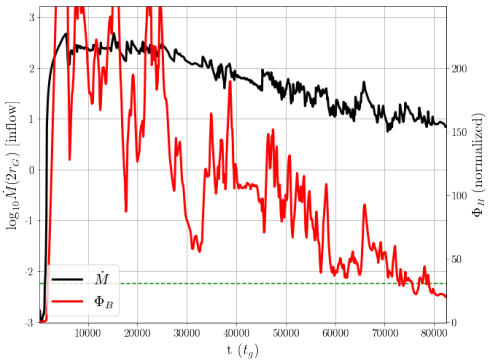

gb20a0

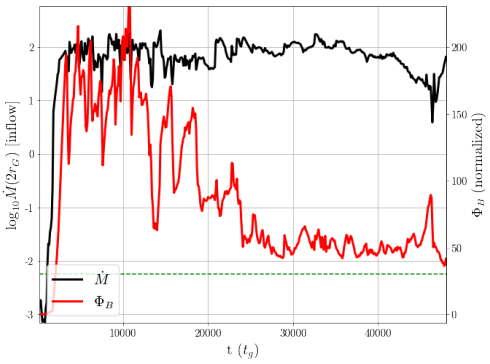

gb20a9

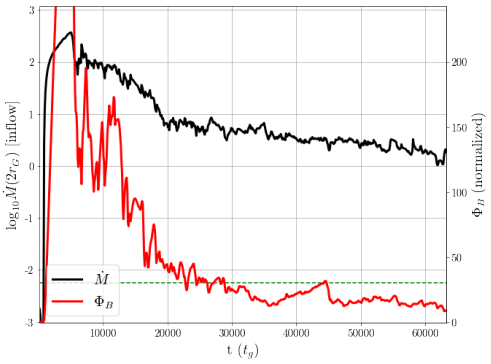

ib20a0

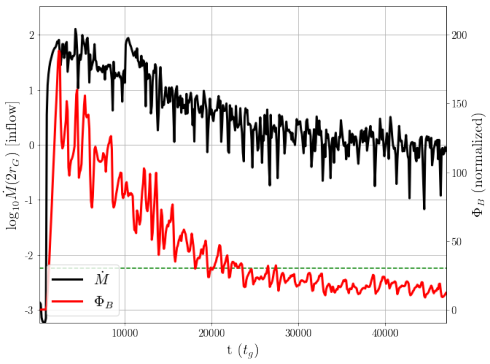

ib20a9

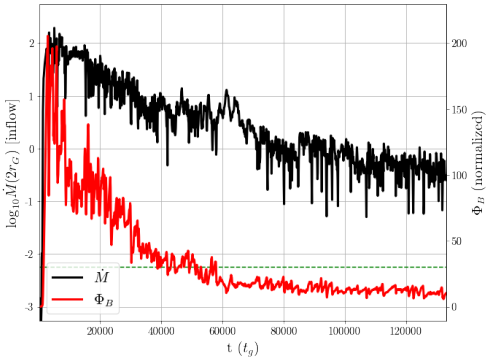

jb20a9

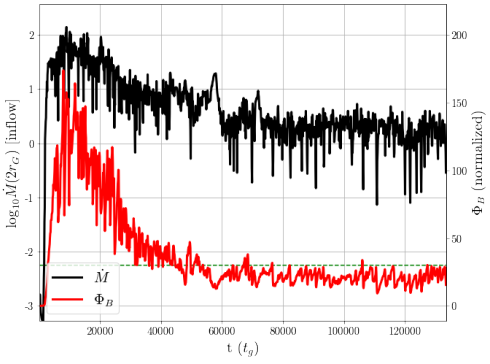

jb100a9

Figure 2.5: Time evolution of the accretion rate and the magnetic flux at r_H for the simulations.

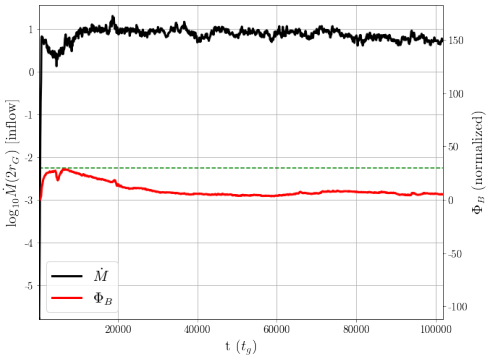

mb20a0

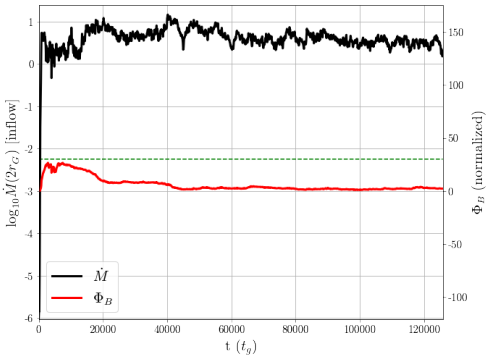

mb20a9

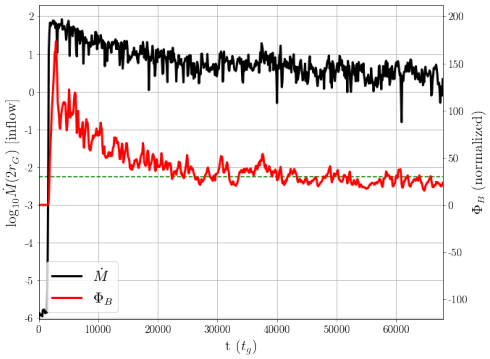

nb20a9

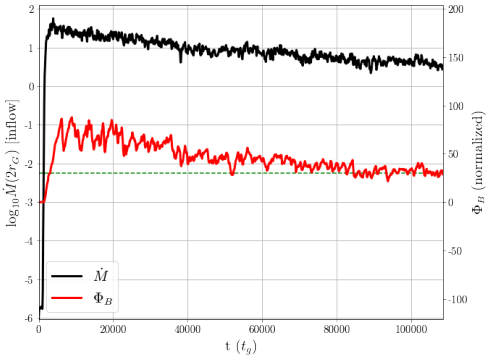

lb100a0

Figure 2.6: Continuation of figure 2.5.

It is not useful considering the rest mass energy in the energy flux, so we define the energy flux as

$$\dot{e} = \dot{e}_{\rm tot} - \dot{m} = -T^r_t - \rho u^r, \tag{2.25}$$

If $\dot{e} > 0$, the energy is being ejected. Integrating over θ and ϕ, we can estimate the ejection efficiency as

$$\eta(r) = \frac{1}{|\dot{M}_{\rm net}(2M)|} \int_\theta \int_\phi \dot{e}\ dA_{\theta\phi}. \tag{2.26}$$

Being $dA_{\theta\phi} = \sqrt{-g} d\theta d\phi$ the area element in the plane $\theta - \phi$.

Considering our definition for winds presented in (2.18), we can set the wind efficiency as

$$\eta_w(r) = \frac{1}{|\dot{M}_{\rm net}(2M)|} \int_\theta \int_\phi \dot{e}[1 < -hu^t < 1.02]\ dA_{\theta\phi}. \tag{2.27}$$

We calculated the wind efficiency for all simulations as shown in figures 2.7-2.8. These figures show the value of the efficiency for three arbitrary radii: $R = 50$M (solid red line), $R = 200$M (cyan dashed line), and $R = 1000$M (yellow dash-dotted line). For all panels, the values are always close, with a slight increase of η_w with the radius. The temporal production of wind during the time range $t \sim 10000 - 50000$M had a median value of 1-10% (except in simulation `mb20a0` that presented very low efficiency). The dependence on spin increases the wind power by a factor of $\sim 2 - 3$.

For each simulation, we analyzed the radial wind efficiency profile averaged during the time $t \sim 45000 - 50000$M and compared it with the radial jet efficiency as it was shown in figures 2.9-2.10.

Figures 2.9-2.10 show the jet power as the dominating channel for simulations with $a = 0.9375$, except for `mb20a9`. Still, for the case of $a = 0$, the jet is much weaker, and most of the outflow power is in the form of winds. Wind production is weakly dependent on the spin, carrying away 1-10% of the accreted energy in all simulations. Also, the jet efficiency is almost independent of the radius, and the wind slightly increases in power with the radius, with $\eta_w \propto r^{0.2-0.4}$ inside $1000 r_G$.

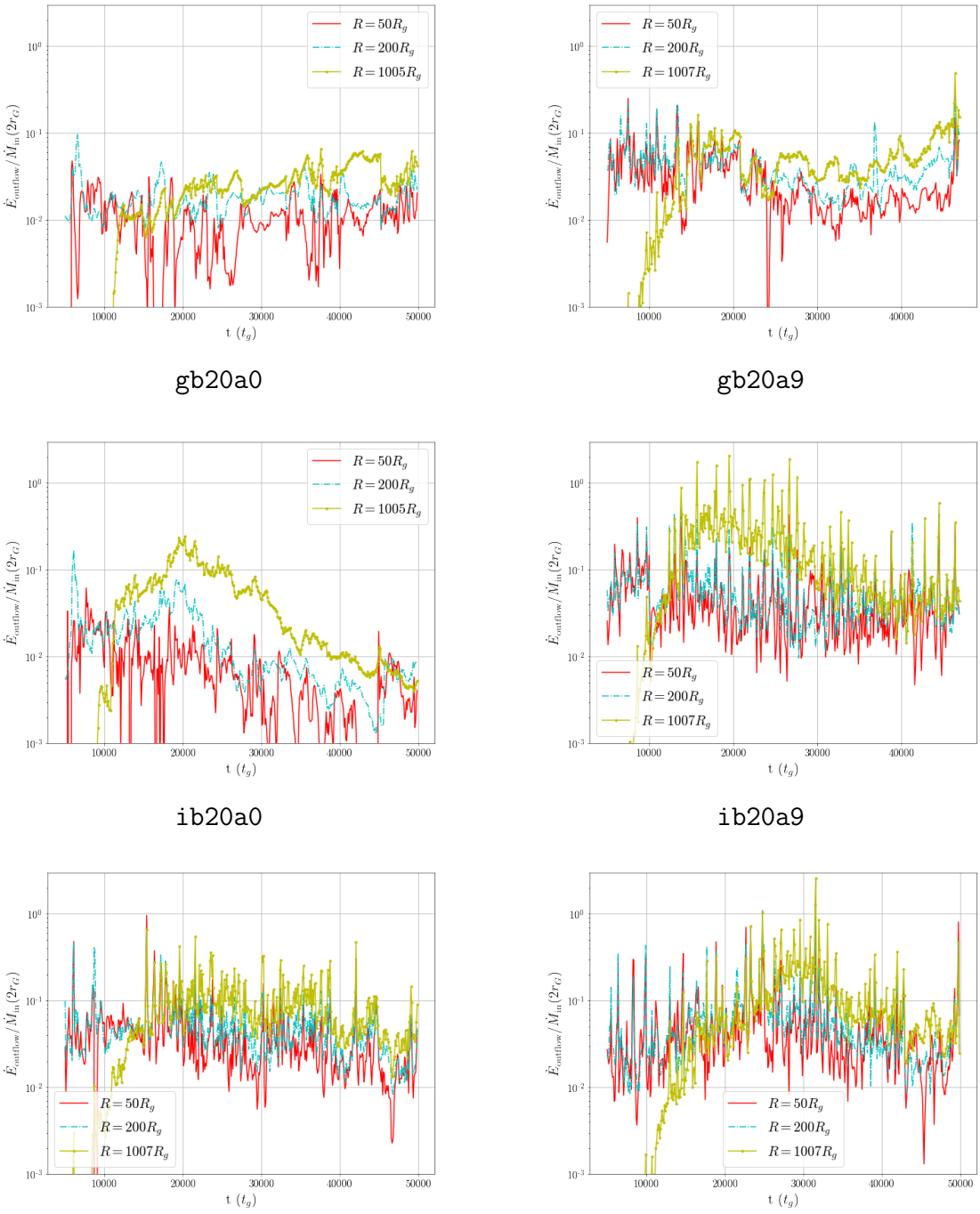

Figure 2.7: Time evolution of the wind efficiency at some radius –R = 50M (red solid line), R = 200M (cyan dashed line), and R = 1000M (yellow dash-dotted line) for the simulations.

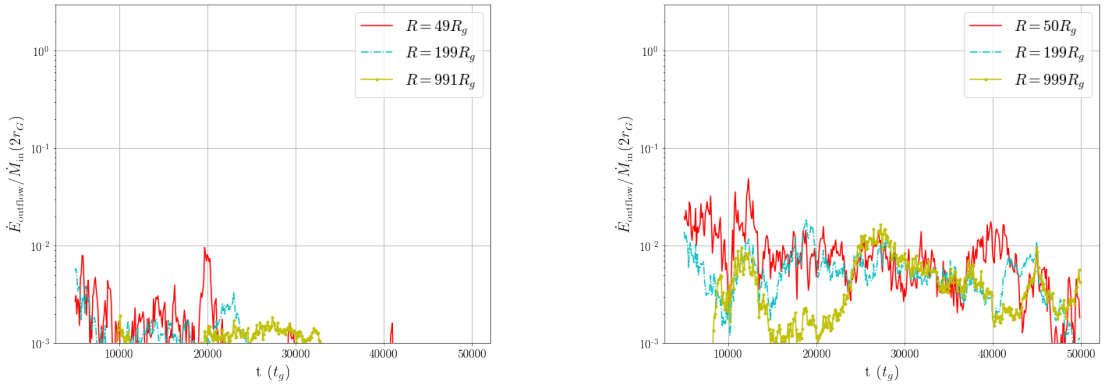

mb20a0

mb20a9

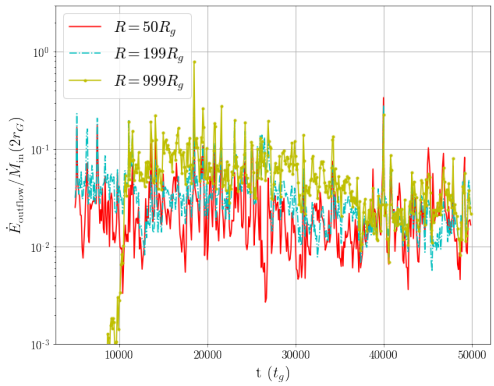

nb20a9

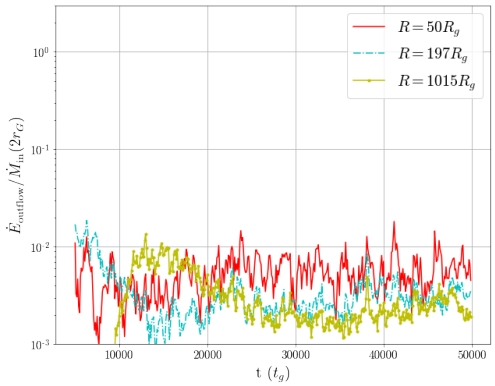

lb100a0

Figure 2.8: Continuation of figure 2.7.

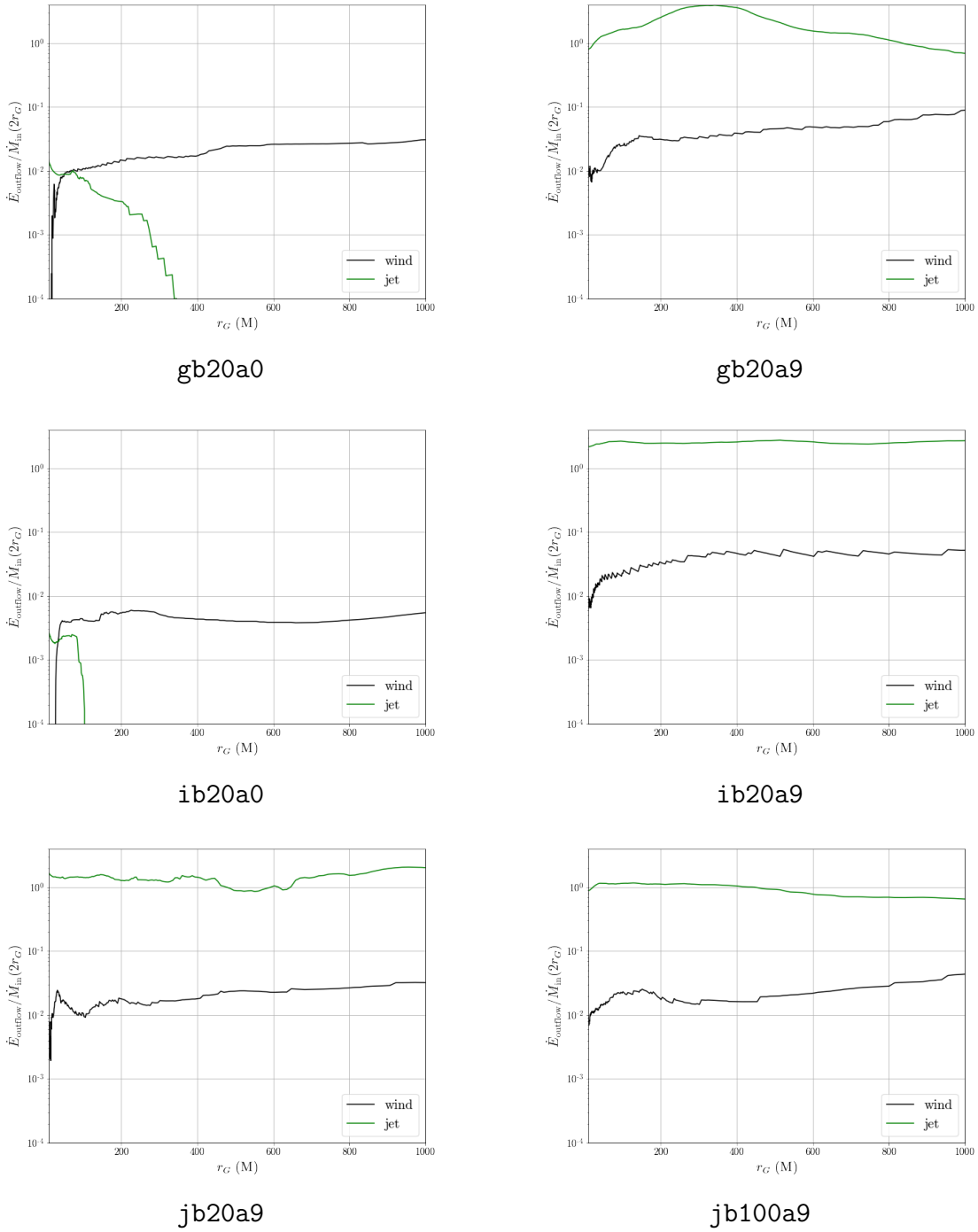

Figure 2.9: The wind (black) and jet (green) efficiency as function of radius averaged between $t \sim 45000 - 50000$M for the simulations.

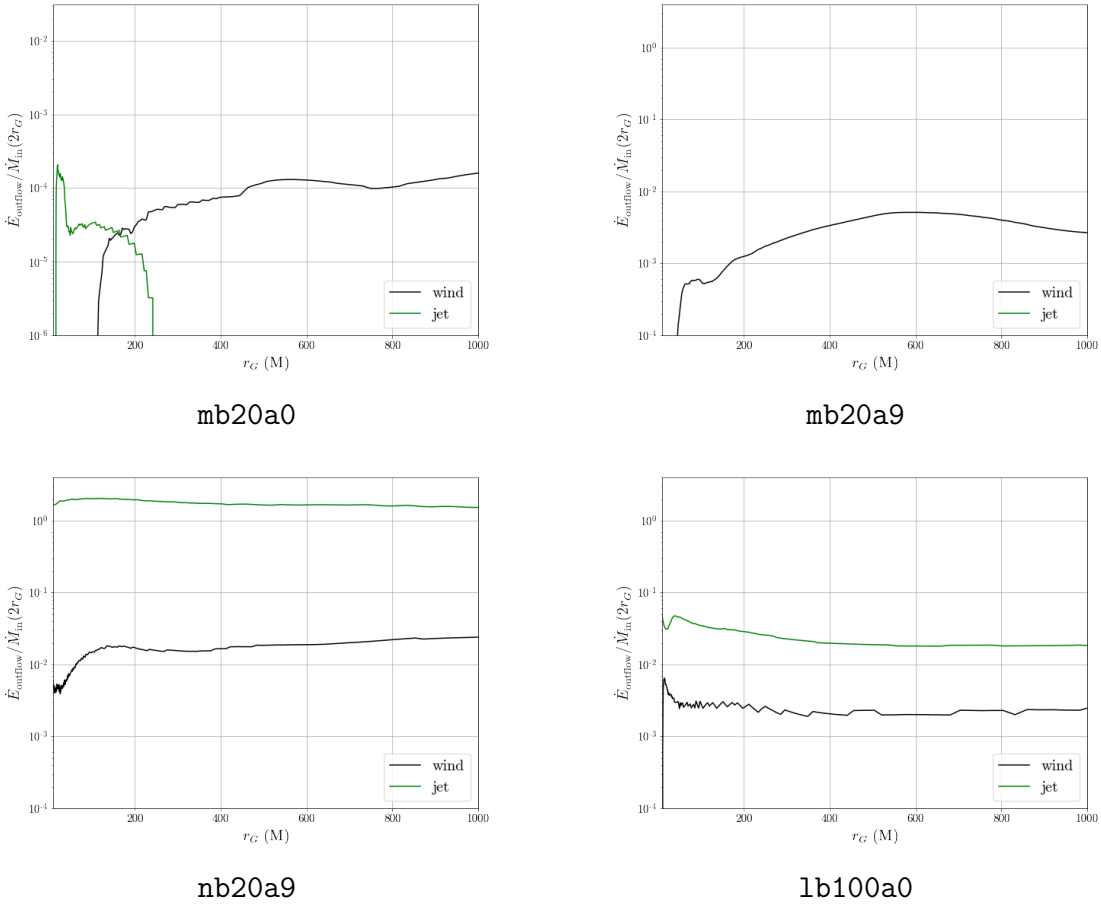

Figure 2.10: Continuation of figure 2.9.

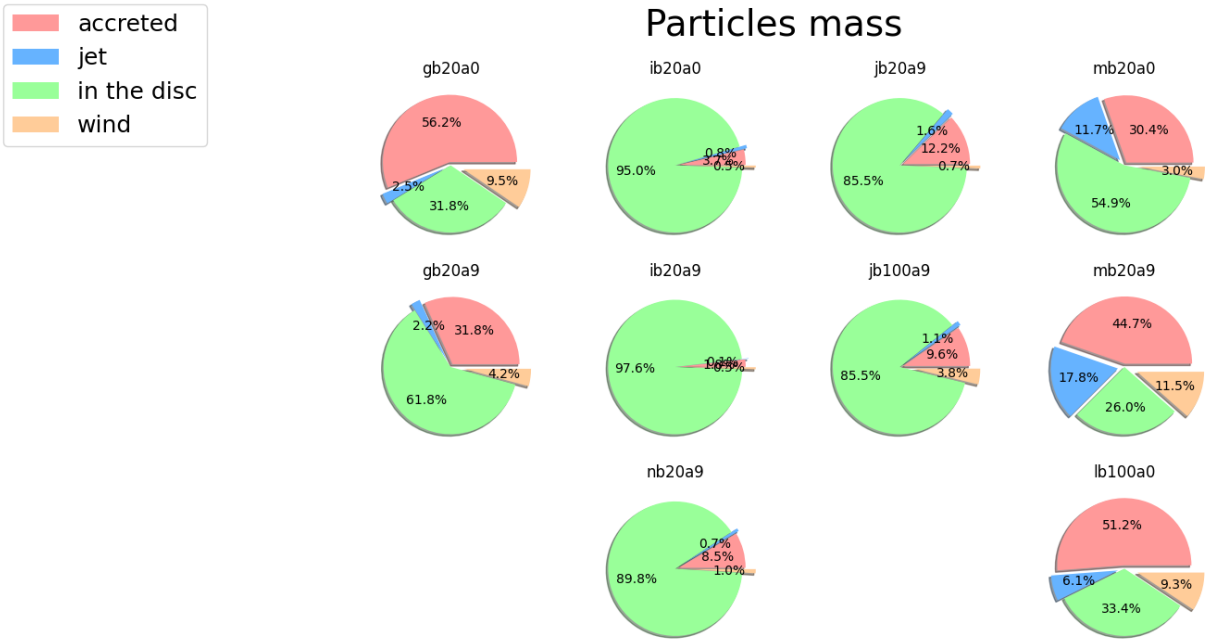

Figure 2.11: Comparison between the ejected particle's mass in the wind and jet, also the mass of the accreted particles from the total for each simulation.

2.6.3 *Analysis using tracer particles*

In Figure 2.11, we show the mass and energy carried away by the outflowing particles following the criteria defined in equation (2.18) for all simulations. The pie charts present some pieces of information.

1. The reservoir of gas is decisive for the simulations with $|\vec{A}| \propto \rho R^3 \sin^3\theta$, and the percentage of accreted particles roughly follows the values of $r_{\rm in}$.

2. For all the models, the mass lost through winds has values between 1-20% values. This is consistent with the plots shown in figures 2.7-2.8.

The particles can be divided in two groups, based on their radial velocity, the particles with $u^r > 0$ or $u^r < 0$. The radial velocity is the average velocity in the last $t \sim 1000$M Positive radial velocity does not mean outflow, but it is a important indicative. In figure 2.12, it is shown the number of particles with positive and negative radial velocities. We also calculated the number of accreted particles – which is a different quantity than the accreted mass since many outflow particles were in lower density regions with $\theta \leq 45^o$.

Figure 2.12 shows a trend linking the spin to the number of accreted particles. Simulations with no spin presented a larger number of accreted particles. While the simulations

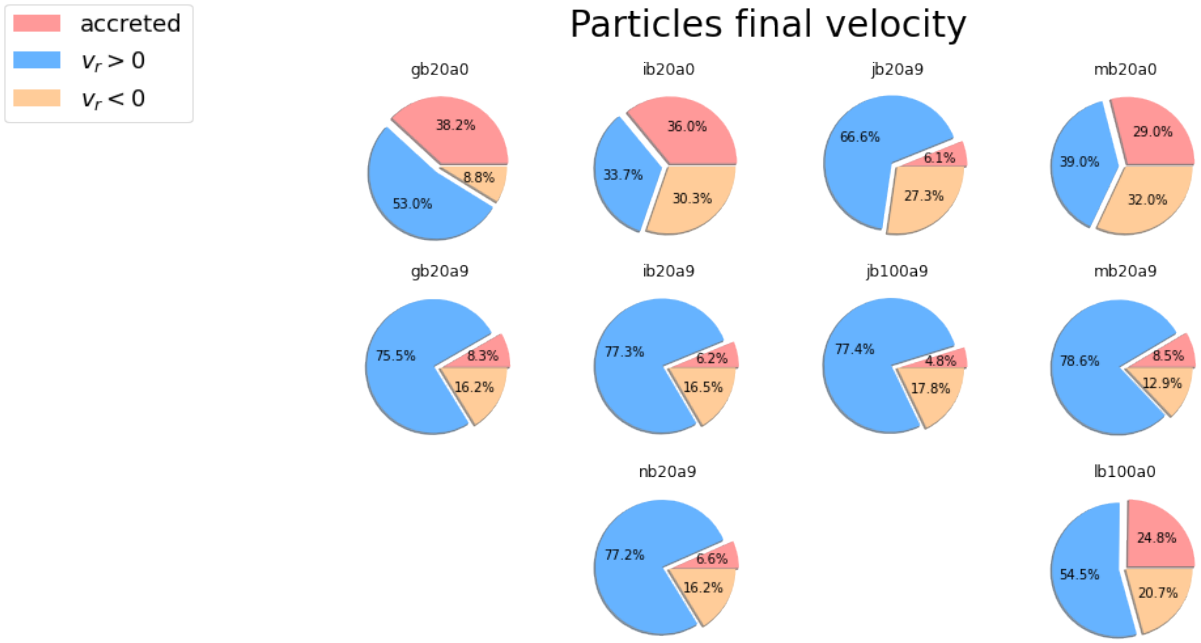

Figure 2.12: The final direction of the particles radial velocity.

with spin $a = 0.9375$ showed almost the same ratios for the number of particles in each category, much lower than the results for $a = 0$. The difference in the number of non-accreted particles and with positive radial velocity is easily explained as the presence of a jet. With higher spin, particles close to the BH can be ejected more efficiently through the intense jet electromagnetic field, preventing them from being accreted.

Looking at the ejected particles' initial and final radius, respectively, $R(t_{\rm initial})$ and $R(t_{\rm final})$. In figures 2.13-2.16, we show how far these particles went. The primary ejection occurred in the polar zones and decreased drastically to $\theta \approx 90^o$. In the middle zone of $\theta \sim 30^o - 45^o$ there are a non-negligible number of outflowing particles also– the outflow zones of jet and wind showed in these plots were based on an approximation of the results from figure (1.4).

2.7 Discussion

2.7.1 Accretion flow and density radial profile

In table 2.6.3, we present the power-law indexes p and s for, respectively, the density radial profile $\rho_{\rm eq} \propto R^{-p}$ and the inflow mass rate radial profile $\dot{m}_{\rm in} \propto R^s$, both averaged over the equatorial region of the accretion flow – between angles 85^o-95^o. From this table,

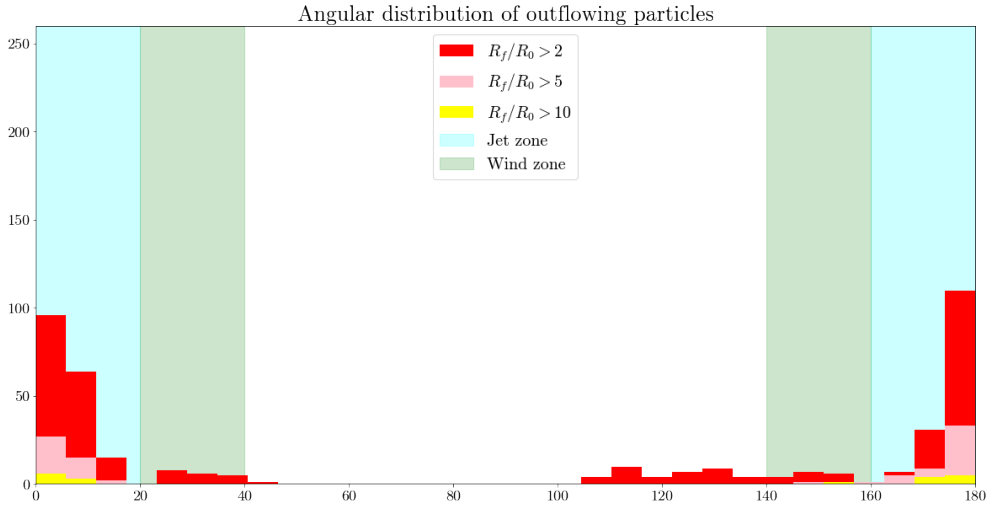

gb20a0

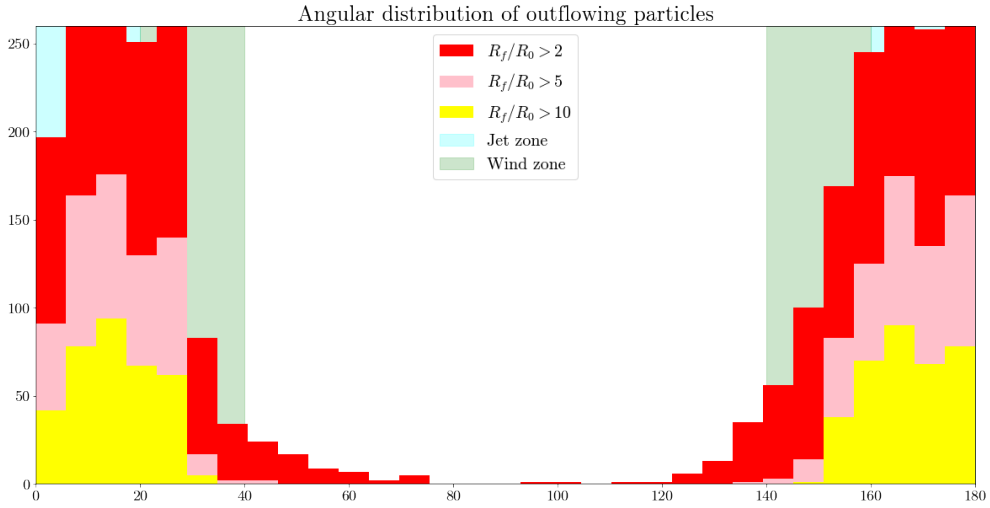

gb20a9

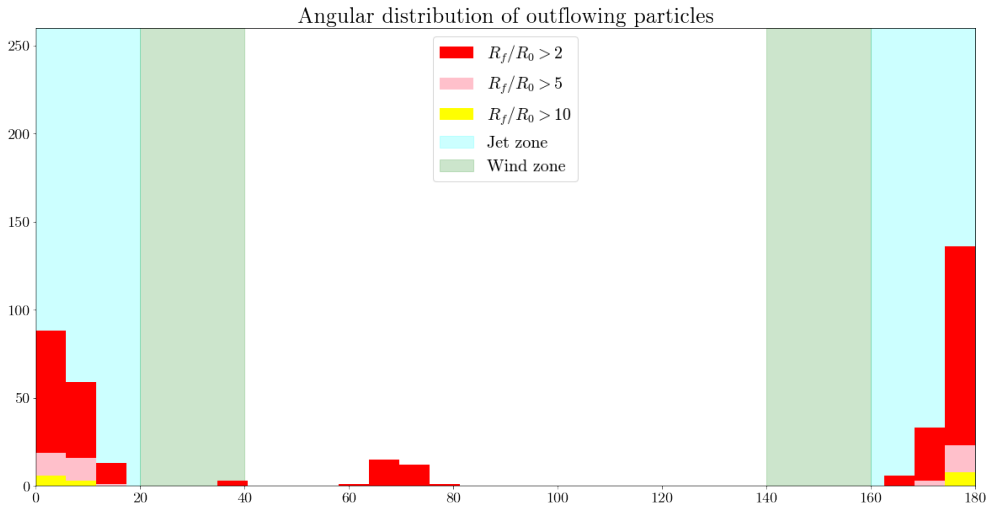

ib20a0

Figure 2.13: Angular distribution of the ejected particles for the simulation set.

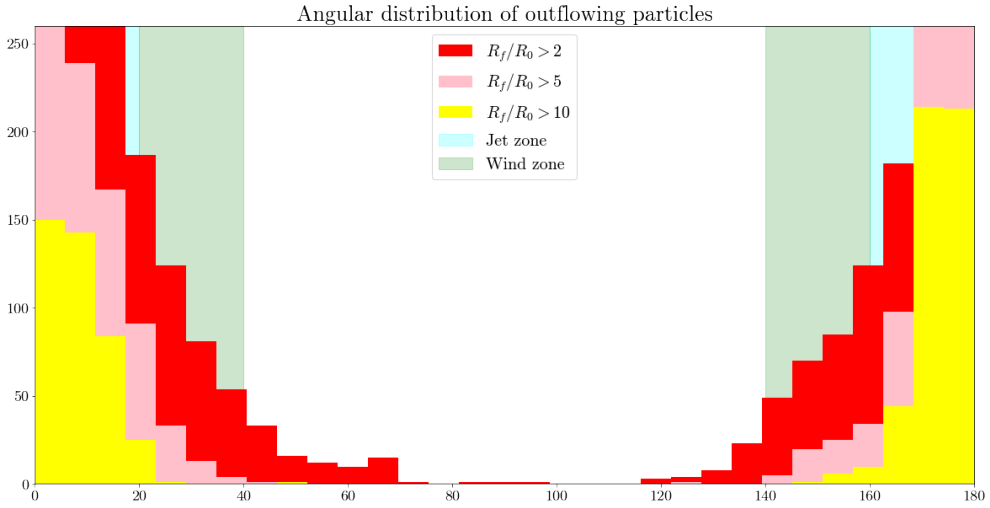

`ib20a9`

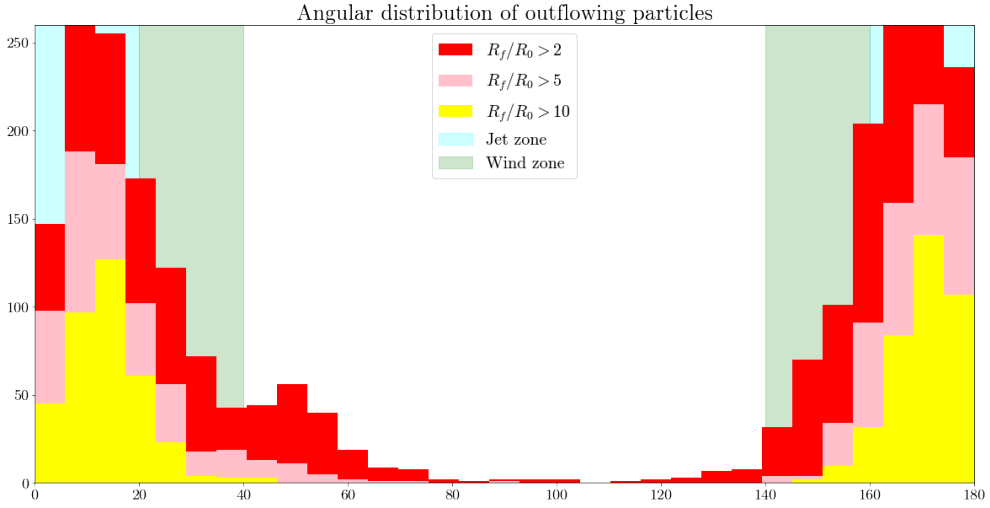

`jb20a9`

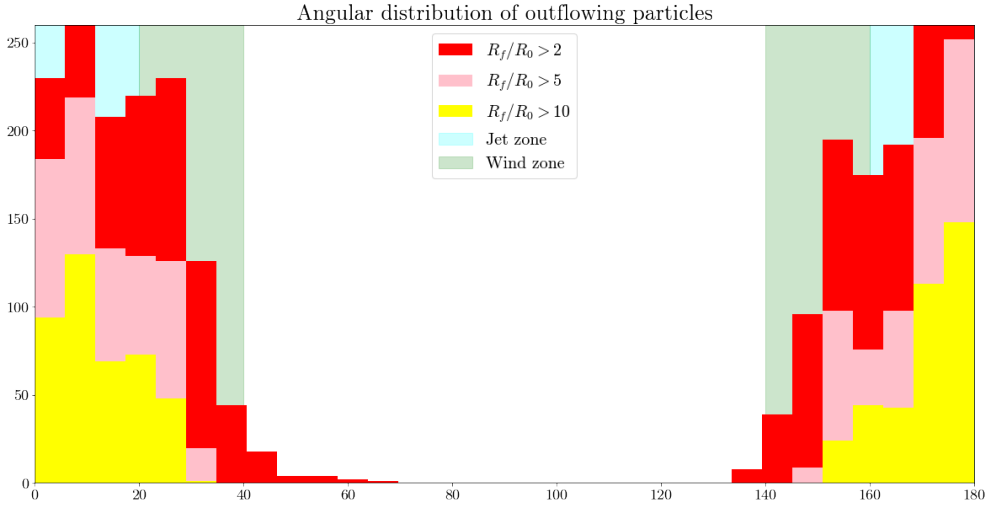

`jb100a9`

Figure 2.14: Continuation of figure 2.13.

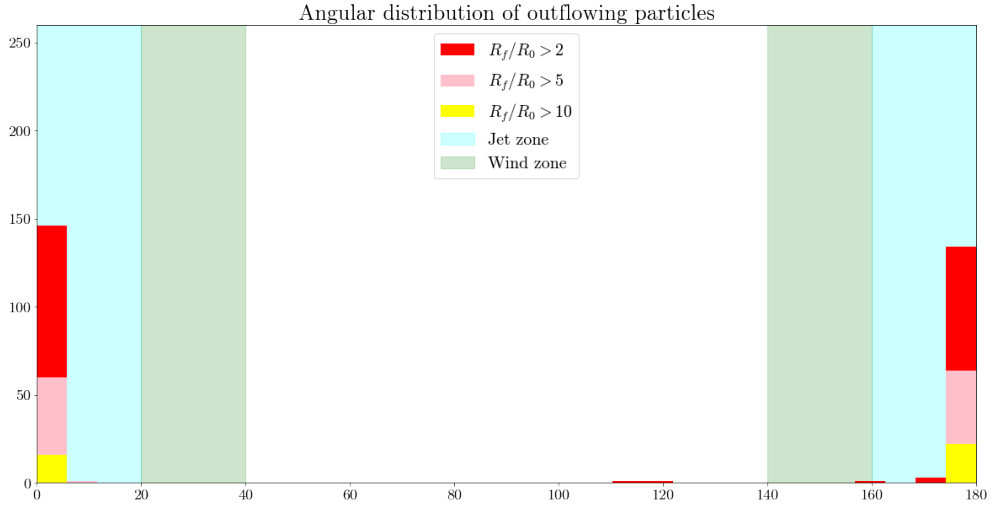

mb20a0

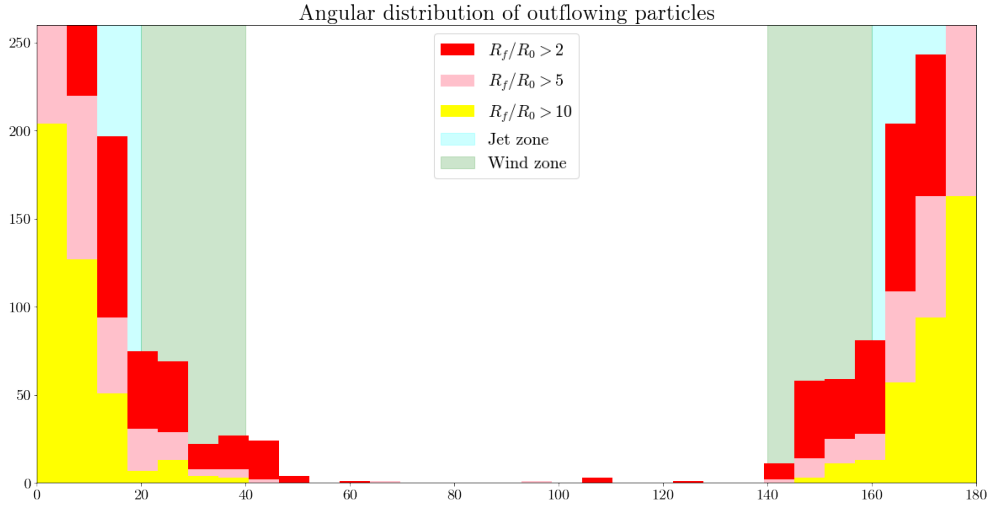

mb20a9

Figure 2.15: Continuation of figure 2.14.

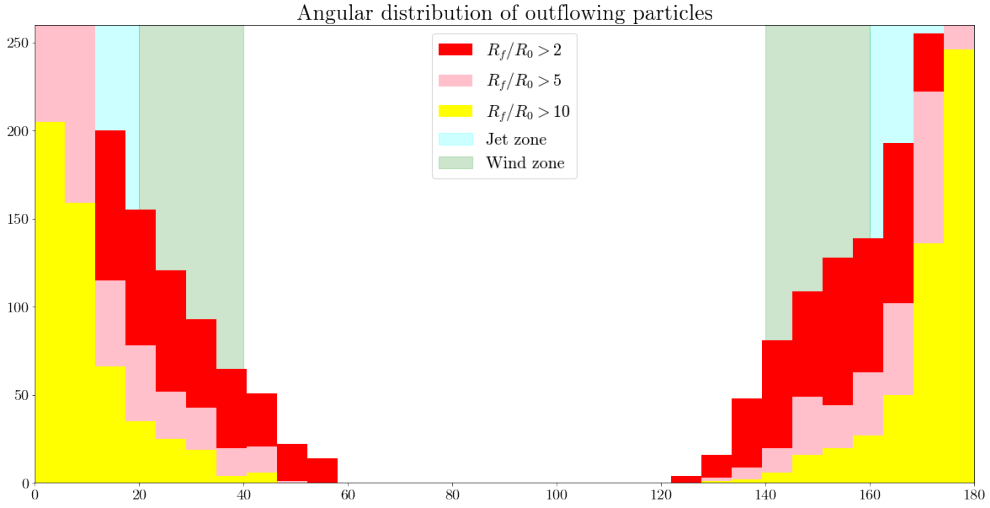

`nb20a9`

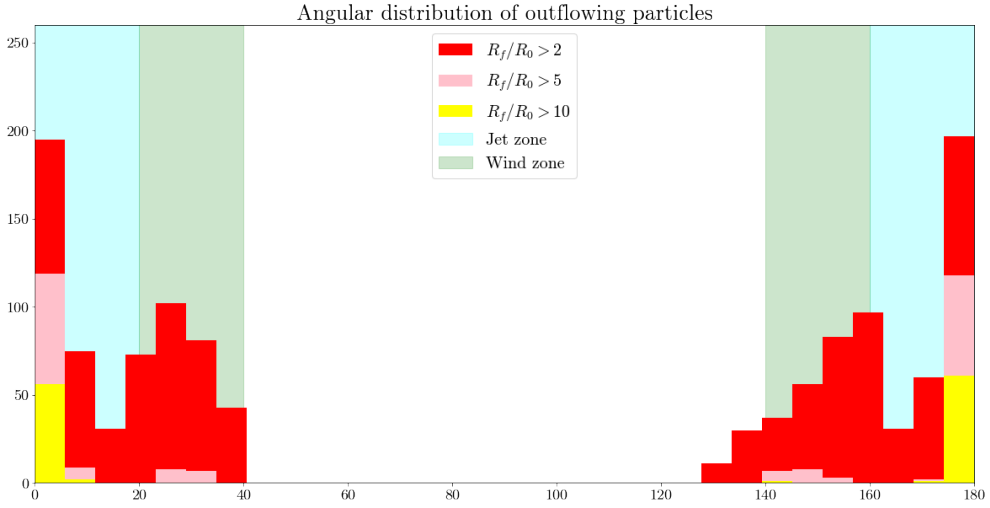

`lb100a0`

Figure 2.16: Continuation of figure 2.15.

Sim ID	$\overline{\Phi}^1_{BH}$	max Φ^2_{BH}	p^3	s^4	$\overline{\eta}^5_w$ (%)	f^6_m (%)	$\overline{v}^7$ ($\times 10^{-3}$)
gb20a0	105	525	1.19	0.42	2.3	9.5	1.1
gb20a9	62	239	1.15	0.68	4.3	4.2	0.9
ib20a0	25	470	0.96	0.21	2.0	0.5	0.3
ib20a9	26	188	1.13	0.59	7.9	0.5	0.5
jb20a9	18	205	1.20	0.09	5.8	0.7	1.3
jb100a9	25	173	0.85	0.51	5.7	3.8	0.9
lb100a0	43	88	1.08	0.10	0.2	9.3	0.7
mb20a0	7	29	1.19	0.18	0.6	3.0	0.1
mb20a9	3	26	1.17	0.69	3.3	11.5	0.1
nb20a9	34	173	1.12	0.40	4.2	1.0	1.5

[1] Median value of the magnetic flux $\Phi_{\rm BH}$

[2] Max value of the magnetic flux $\Phi_{\rm BH}$

[3] Power-law coefficient defined as $\rho_{\rm eq} \propto r^{-p}$

[4] Power-law coefficient defined as $\dot{M}_{\rm in} \propto r^{s}$

[5] Median value of $\eta_w(t)$

[6] Fraction of the mass ejected following the lagrangian particle analysis

[7] Median velocity of the Lagrangian particles

Table 2.2 - Results concerning outflows for all simulations.

we can draw some conclusions:

1. Values of p, in different models, are very close to each other, with $p \sim 1$. The values are slightly above the unity, but the initial conditions did not affect the main behaviour of $\rho_{\rm eq}$.

2. All simulations present a decreasing profile for $\dot{m}_{\rm in}(R)$ in the innermost regions, $R \lesssim 20$M, with a minimum value in $R \sim 20$M. For values of 20M $\lesssim R \lesssim 200$, $\dot{m}_{\rm in}(R)$ is a increasing function.

3. Our results did not present a direct numerical correlation between the value of p and the wind production or s. Their relationship is probably complex and depends on initial condition, spin, and others.

The p in our simulations is not clearly correlated with wind production. No matter the simulation, p is almost unaffected, being impossible to affirm whether winds are being produced only by an inspection of the equatorial density profile. This result does not agree with previous analytical (Blandford and Begelman, 1999; Begelman, 2012) and numerical (Yuan et al., 2012, 2015) work that correlates the values of $\rho(R)$ with mass-loss by outflows.

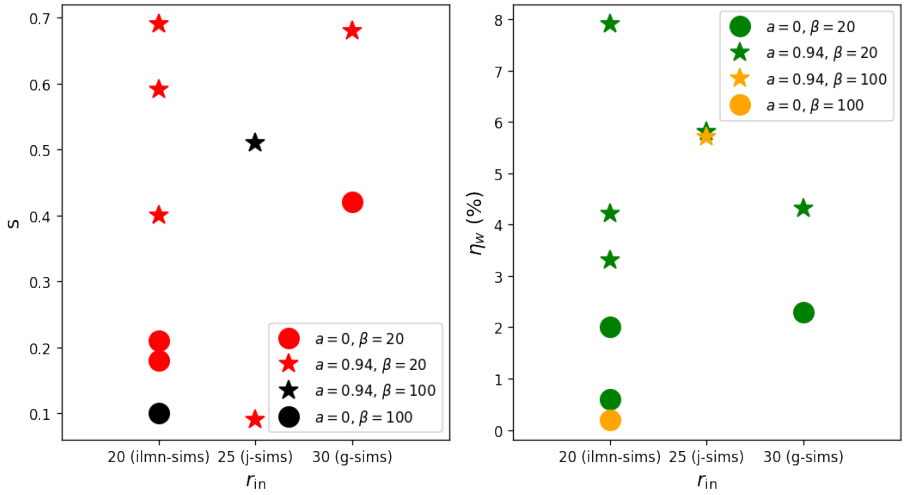

Figure 2.17: Relation of the results for s and η_w with the initial parameters (a, β, and $r_{\rm in}$). The blue circles represent the simulations with no spin ($a = 0$); the stars are for simulations with high spin ($a = 0.9375$), and the star colour is orange for $\beta = 20$ and green for $\beta = 100$.

Our simulations followed the relations between p and s found in our previous work Almeida and Nemmen (2020). The values of s are actually consistent with the whole range $s = 0-1$ (Narayan and Yi, 1994). These results do not agree with the most extreme version of ADIOS models, according to which $s = 1$ and $p = 0.5$ for strong winds. The values we found for s and p are different from these models and still present some powerful outflows. In the same way as Almeida and Nemmen (2020), our conclusion is that we cannot make strong statements about the presence of winds based on the indirect information given by $\rho(r)$ because s and p are probably non-trivial functions of the flow parameters.

Figure 2.17 left panel shows the relations of s with the initial parameters. We cannot observe a visible correlation here. However, in the right panel, the ties between η_w and the spin and $r_{\rm in}$ are easier to be seen. For $a = 0$, we found very similar values of η_w. The differences arise when we take the higher spin. The starred data points present η_w $2-4\times$ higher than the circle data points and a decreasing relation with the gas reservoir size. The connection between η_w and a can be due to our definition of winds using $-hu^t$, since we are not actually distinguishing the origin of the outflow and only considering the final energy of it. We assume that for the wind feedback at larger scales, it does not matter the exact origin of the ejected hot gas.

In this work, we only performed two simulations with $\beta = 100$. Compared to the other simulations, we did not see a distinguishable feature in `jb100a9`, but `lb100a0` presented the lowest value of η_w. Figure 2.17 nor 2.11 did not reveal anything special about this

simulation. Even in the panel for simulation `jb100a9` in figure 2.5 is not very different from the others.

The inclination angle (i) slightly affected the wind production. We noted the highest values of η_w are from simulations with $i = 45^o$. Its effect is more noticeable in the density maps as the jet becomes more unstable, the toroidal disc is torn apart, and the density distribution becomes very uncertain. This behaviour can increase the angular jet zone and probably eject more particles.

2.7.2 Wind launching mechanism

Our previous work Almeida and Nemmen (2020) reported the production of powerful thermal winds (a.k.a. Parker winds) arising from the very hot accretion flow. Our simulations reported here also find temperatures over 10^{11-12}K for $R \sim 100 - 1000$M. Looking at the ratio between gravitational binding energy and thermal energy

$$\Lambda = \frac{2GMm_H}{5rkT(r)} \tag{2.28}$$

where m_H is the hydrogen mass and k is the Boltzmann constant. For $\Lambda \leq 1$, the thermal energy overcomes the gravitational energy and winds can be thermally launched via thermal expansion. In our systems, $\Lambda \gtrsim 1$ in the equatorial zone and $\Lambda \ll 1$ in regions outside the bulk of the mass accretion inflow –$\theta \leq 45^o$–, which means some Parker winds can also be ejected.

However, let's compare the reported simulations with the results from Almeida and Nemmen (2020). We can see a considerable increase in wind efficiency. The lowest value reported here is almost twice that in our previous work, indicating that something in these simulations increases the wind power by one order of magnitude. Qualitatively, the reason is clear: the introduction of magnetic fields and the GR effects. The electromagnetic field adds a new force to the calculation. The rotating gas suffers the impact of the poloidal electromagnetic field, and a Lorentz Force appears over the gas particles. This is the main difference between the simulations and the reason for the one-order-of-magnitude increase in wind power. Whereas the wind in Almeida and Nemmen (2020) is a Parker wind, the winds in the reported simulations fulfil the Parker criteria of $\Lambda > 1$ (see equation (2.28)) also. It seems like these winds are magnetically driven. Also, spin plays a relevant role in producing winds, as shown in figure 2.17. The presence of the jet and the interaction

between the jet border with the gas can be an explanation for enhancing wind production. Especially for the case $i = 45^o$, the jet can directly interact with the thick accretion disc disrupting it and triggering winds.

We also have a persistent wind emission in these simulations, unlike in Almeida and Nemmen (2020). The magnetically-driven winds showed a more consistent production over time, the differences between figures 2.7-2.8 and figure 10 in Almeida and Nemmen (2020) we found. It is worth saying that simulation PLSS.3 is the most similar simulation from Almeida and Nemmen (2020) to our new set of GRMHD simulations.

2.7.3 Comparison with observations

Our simulations resulted in values $p \sim 0.8 - 1.2$. The resulting density profiles are marginally consistent with those constrained from observations of LLAGNs, for instance, NGC 3115 ($p \sim 1$; Wong et al. 2011, 2014; Almeida et al. 2018) and M87 ($p \sim 1$; Kuo et al. 2014; Russell et al. 2015; Park et al. 2019).

We have found that a typical value for the efficiency of wind production in this simulation set η_w is $2 - 8\%$. This value is one order of magnitude above the mechanical feedback efficiency required in cosmological simulations of AGN feedback in the radio mode (Ciotti et al., 2010; Sijacki et al., 2007, 2015). These simulations require an efficiency $10 - 100\times$ smaller to reproduce the observations and prevent the cooling of these systems. As the winds expand, their efficiency can decrease with the interaction with the ISM, so a wind $100\times$ more potent than the necessary at the launching scale can be a good hint these winds can have some impact on galactic scales. Given the typical values of η in our simulations, we can parameterize the wind power from RIAFs using equation 2.27 as

$$\dot{E}_{\rm wind} \sim 5 \times 10^{41} \left(\frac{M}{10^8 M_\odot}\right) \left(\frac{\dot{M}(R_{\rm out})}{10^{-3}\dot{M}_{\rm Edd}}\right) \ {\rm erg\ s^{-1}} \tag{2.29}$$

where $\dot{M}$ is taken as the accretion rate fed at the outer radius of the accretion flow, which we defined as $R_{\rm out} = 1000$M. Here, we assme that $\eta =$ constant. Extrapolating a little our result, supposing the wind power goes as a power-law $\eta_w \propto r^q$, if $q \sim 0.5$ the wind power at larger scales as the Bondi radius ($R \sim 10^5 M \sim 1$pc) will be $\gtrsim 5 \times 10^{40}$erg/s, and for 1kpc the wind would be $\sim 10^{39}$erg/s.

Comparing now the energetics of our modelled winds with observations of LLAGNs. The "Akira" galaxy hosts a $10^8 M_\odot$ SMBH accreting at $\dot{M} \sim 10^{-4}\dot{M}_{Edd}$ (Cheung et al.,

2016). Applying equation (2.29) to Akira, we obtain $\dot{E}_{\rm wind} \sim 5 \times 10^{40}$ erg s^{-1}. The wind kinetic power derived from integral field unit observations of the ionized gas is $\approx 10^{39}$ erg s^{-1}, this difference, can be explained by an attenuation of the wind as it flows through the galaxy medium. The results estimated from our simulations agree with the "Akira"case –considering the wind can lose part of its energy as it propagates through the galaxy. A wind with such power can inject sufficient energy to impact Akira. Still, this topic will be better discussed in chapter 4. Moreover, the simple wind model of Cheung et al. (2016). gives a constant radially-outward velocity of 310 km s^{-1} in a wide-angle cone in Akira. From our simulations, the average velocity of the outflowing particles was $\sim 10^{-3}c \approx 300$ km s^{-1}, which is in excellent agreement with the observations reported by Cheung et al. (2016). In conclusion, the wind properties observed in the Akira galaxy are well explained as winds from a RIAF as modelled in this work.

The SMBH at the center of Our Galaxy–Sgr A*–is accreting with a Bondi rate of $\dot{M}_{\rm Bondi} \approx 10^{-5} M_{\odot}/yr \approx 10^{-4}\dot{M}_{Edd}$ (Baganoff et al., 2003) and at the horizon scales $\dot{M}_{\rm EHT} \approx 5 - 9 \times 10^{-9} M_{\odot}/yr \approx 10^{-7}\dot{M}_{Edd}$ (Akiyama et al., 2022b). Taking into account the RIAF solution gives $\dot{M} \sim 0.1\dot{M}_{\rm Bondi} \approx 10^{-5}\dot{M}_{Edd}$. Putting on equation 2.29 we got $\dot{E}_{wind} \approx 2 \times 10^{38}$ erg s^{-1}. This estimate is similar to the power estimated by some authors and, more recently, by the EHT collaboration (Falcke et al., 2000; Merloni and Heinz, 2007; Akiyama et al., 2022b). Such winds can be relevant in studying the Pevatron observations by the High Energy Stereoscopic System collaboration (HESS Collaboration et al., 2016) and the *Fermi* bubbles (Su et al., 2010) in our galaxy.

Shi et al. (2021) reported observing a hot flow inside the inner regions of the M81 –a galaxy that hosts an LLAGN (Bietenholz et al., 2000; Ho et al., 1996; Young et al., 2018). Using `Chandra` high-resolution X-ray spectroscopy, they analyzed Fe XXVI and Ly α lines. They found a high-temperature and high-velocity plasma that stellar origin cannot explain. Their analysis agrees with the scenario of a wind coming from the LLAGN. They estimate, with simulations, the wind power output of 2×10^{40}erg/s at 20pc, which agrees with equation (4.5), considering the wind will lose power as it expands.

Considering the energetic output of our winds, they could be agents of AGN feedback in galaxies hosting LLAGN. Such feedback would be neither in the radio mode nor in the quasar mode since we are modelling SMBHs accreting at low rates. One class of galaxies which could be subject to this type of feedback–in fact, it seems to be required to explain

them–are LLAGNs in the proposed "red geyser" mode (Cheung et al., 2016; Roy et al., 2018; Roy et al., 2021). In red geysers, we observe large-scale periodic low-power winds from the central region, $R \lesssim 3$kpc (Ilha et al., 2022), with velocities $v_r \sim 200 - 300$km/s (Roy et al., 2021) –possibly related to the LLAGN activity. These outflows could heat the surrounding gas, preventing any substantial star formation and maintaining the quiescence in typical galaxies. We treated the topic in more detail with an analytical model in Almeida et al. (2023) (chapter 4).

2.7.4 Comparison with previous numerical simulations

Our simulations produced efficient winds with values of $p \sim 0.8 - 1.2$, which is below the self-similar, no-wind ADAF solution (Narayan and Yi, 1994), $p < 1.5$ is in general agreement with expectations of the ADIOS model (Blandford and Begelman, 1999). Our simulations are in marginal agreement with previous hydrodynamical simulations (Stone et al., 1999; Yuan et al., 2012), with higher values. Our simulations did not display any correlation between p and s as in Almeida and Nemmen (2020).

On average, the efficiency of the winds in our models is in the range $\eta_w \sim 2 - 8\%$, which is in agreement with the typical values of $\eta_w = 3\%$ found by Sądowski et al. (2016) in their GRMHD simulations of RIAFs around nonspinning BHs and close to one order of magnitude higher than the thermal Parker winds reported in Almeida and Nemmen (2020). Actually, had some bursts of wind, with values of $\eta_w \gtrsim 10\%$ for a particular time in the simulations, showing the possibility of winds being variable in time –we did not find any defined variability, so these variations are probably stochastic.

The recent work of Yang et al. (2021) studied wind production using GRMHD and found similar results. They performed three simulations with a duration larger than ours and characterized the outflows. This work found a relation a ratio between the jet and wind power of $P_{\rm jet}/P_{\rm wind} \sim 10$ for the case with maximum spin $a = 0.9375$, with the ratio slightly increasing with the radius. This is in good agreement with what we found (figures 2.7-2.10). We also agree with Yang et al. (2021) for $a = 0$, where the wind dominates the energy of the outflows.

2.7.5 Shortcomings

Our simulations did not consider the effects of radiation pressure. We assumed RIAFs are low-density, optically thin systems, with the radiation field only interacting very weakly with the gas. This is a good approximation, but it neglects any effect from cooling –cooling also can be implemented as a source term for removing energy for the gas, following some prescription (Xie and Yuan, 2012). It is known that cooling can have significant effects like the state transitions in high-massive X-ray binaries (Esin et al., 1997; Vemado, 2020; Liska et al., 2022), which can also be relevant for LLAGN in the cases of higher accretion rates (Yuan et al., 2009; Bu and Gan, 2018).

Another problem of our model regards the jet nature. Our jets are empty funnels filled with electromagnetic energy. The jet carries away an amount of mass much lower than the wind, even tough it carries out energy two orders of magnitude more energy than the wind. In nature, however, jets are not entirely empty. This is a problem of the GRMHD models that cannot treat self-consistently the matter content of the jet. To solve this issue, we need to solve the Vlasov equation, which is out of our work's scope.

Our simulations explore outflows produced in a hot accretion flow (Yuan and Narayan, 2014). This model is recently confronted by a highly magnetized model consisting of a magnetically dominated "ergomagnetosphere" that can transport electromagnetic angular momentum and energy outwards through a large-scale magnetic torque and some small-scale instabilities (Blandford and Globus, 2022). Only observational tests can rule out one of the two theoretical models.

Some of the simulations presented an unusual behaviour of the jet, simulations like `ib20a9` and `jb20a9` (see figure 2.3) had a non-aligned jet axis with the simulation poles due to the inclination angle $i = 45^o$.

In the density map of simulation `gb20a9` (figure 2.3), there is no jet to be seen. At some point in the accretion flow evolution, the disc "invaded" the jet zone, increasing the density value in the region when we took the time average to create the figures. The average procedure hid the jet, but it can be seen if you analyze a video of the simulation – the same happened in `jb100a9`. The same jet is not easily seen in the density map of simulation `gb20a0` and `ib20a0`, but in this case, the spin is $a = 0$ the jet is not prominent as in the other simulations.

2.8 Summary

In this work, we performed three-dimensional numerical GRMHD simulations of radiatively inefficient accretion flows onto BHs. Our models evolved for up to $5 \times 10^4 GM/c^3$. Our initial conditions involved large tori extending to 500-1000M radii. Given that the initial conditions of accretion flows are poorly constrained, we explored some variations of disc size and magnetic field strength. We tried two different types of BH regarding the spin ($a = 0$ or 0.9375. Our main goal was to investigate the properties of the outflows emanating from these large, hot accretion flows and compare the properties of these winds with those of low-luminosity AGNs–clarifying along the way their potential for AGN feedback. In our definitions, winds are non-relativistic non-collimated outflows, and we did not differentiate a wind from a jet from a wind from the accretion flow. We were only interested in the overall energetics of these ejections. Here we present a brief summary of our main results:

- Our accretion flows produced powerful subrelativistic, magnetically-driven winds reaching velocities of up to $0.01c$.
- The wind powers correspond to $2 - 8\%$ of the rest-mass energy associated with inflowing gas at large distances, $\dot{E}_{\rm wind} = (0.02 - 0.08)\dot{M}c^2$.
- The properties of our simulated winds largely agree with constraints for the prototypical example of LLAGN wind–the Akira galaxy–and can explain how red geysers can heat ambient cooler gas and thereby suppress star formation.
- The equatorial density profile of the accretion flow $\rho(r, \theta = 90^o)$ displayed a complex behaviour which follows the general expectations from the ADIOS models. However, we could not make strong statements about the presence of winds based on the indirect information given by $\rho(r)$.
- We found the spin has a noticeable impact on the wind efficiency η_w. Simulations with spin $a = 0.9375$ presented a wind efficiency increase by ~ 2.
- Most winds generated were continuous winds the whole simulation time. Sometimes winds produced powerful bursts with η_w reaching $\gtrsim 10\%$.

We adopted two approaches in analyzing our simulations: (i) looking at the energy and mass fluxes between spherical shells and (ii) using Lagrangian tracer particles to track the wind. The results given by both techniques were consistent, with both approaches supporting the scenario of winds as a generic feature of hot accretion flows. These thermal winds can be a mechanism of feedback in LLAGNs.

We propose two improvements to our simulations: adding a cooling prescription and improving the resolution. The cooling can affect hot accretion flows with accretions flows $\dot{m} \gtrsim 10^{-2}$ and can be dynamically relevant in some cases.

Chapter 3

AGNNES

3.1 Introduction

Present-day galaxies host a population of underfed supermassive black holes (SMBHs) in low-luminosity AGNs (LLAGNs). Some notable examples are Sagittarius A* (Sgr A*; Narayan et al. 1995; Yuan et al. 2003), NGC 3115 (Wong et al., 2014), and M87 (Akiyama et al., 2019b). The observational properties of LLAGNs are quite unlike those of more luminous Seyferts and quasars (e.g. Ho 2008). These properties can be nicely explained by SMBHs accreting at rates $\dot{M} < 10^{-2}\dot{M}_{\rm Edd}$ ($\dot{M}_{\rm Edd}$ is the Eddington accretion rate). As a consequence of such low mass accretion rates, these SMBHs convert a much smaller fraction of the accreted rest mass to electromagnetic radiation compared to the canonical 10% typical of thin accretion disks.

The resulting radiatively inefficient accretion flows (RIAFs) explain the low-luminosity of such LLAGNs, their spectra and many other properties (e.g. Yuan and Narayan 2014). RIAFs are extremely hot, optically thin, and geometrically thick. Due to hot electrons in such flows, they have an emission peak in the radio via synchrotron emission (e.g. Narayan et al. 1998). These electrons also upscatter the radio photons via inverse Compton scattering (IC), producing X-rays. RIAFs are prone to producing relativistic jets (e.g. Tchekhovskoy 2015) and indeed the emission from a jet is required to explain the radio observations of most LLAGNs (e.g. Yu et al. 2011; Nemmen et al. 2014).

Modeling the radio to X-rays spectral energy distributions (SED) of LLAGNs has been the poor man's way of testing accretion flow scenarios and estimating the mass accretion rate $\dot{M}$, density profile and electron heating properties (e.g. Yuan et al. 2003; Nemmen et al. 2006; Markoff et al. 2008; Nemmen et al. 2014; Mościbrodzka et al. 2014; Almeida

et al. 2018; Bandyopadhyay et al. 2019), given that the luxury of resolving and modeling near-horizon emission is currently limited to a few object (Akiyama et al., 2019a, 2022a).

All such SED models suffer from one main shortcoming: they are computationally expensive, due mainly to the numerical treatment of the Compton scattering. In a typical multicore workstation, calculating one single model for a given set of input RIAF parameters takes about one minute. This renders statistical fitting of the models to data impractical, since a typical fitting procedure (e.g. least-squares fitting or Markov chain Monte Carlo (MCMC) methods) makes thousands of model calls. This is the reason why virtually all comparisons of RIAF and jet SED models to LLAGN observations are not actual fits, since the goodness of fit is judged by eye rather than using a statistical technique (e.g. Nemmen et al. 2014) (hereafter, N14). These limitations motivated us to explore alternative routes for SED models.

Artificial neural networks (NN) are a promising supervised machine learning method with an almost endless potential for applications (George and Huerta, 2018; Thuerey et al., 2021). NNs are nonlinear functions inspired by the brain, consisting of "neurons" and connections between them. Each neuron has a activation function $f(\sum(w_i x_i))$ associated with it which maps inputs x_i and weights w_i to the neurons in the layers that follow (Leshno et al., 1993). When there are many layers involved, we call this function deep learning (DL) (e.g. LeCun et al. 2015).

In a typical DL workflow, the DL model is trained (or fitted in astronomical jargon) in an iterative manner with many input-output examples. This procedure updates the weights of the deep neural network via gradient descent. Once the DL model is trained, it usually results in an excellent approximator for whatever function is originally responsible for mapping inputs into outputs in the training data set (Cybenko, 1989; Zhou, 2020) — even if the function is too complex to have an analytical form as is the case in computer vision problems (e.g. Krizhevsky et al. 2017). Effectively, this makes DL models excellent interpolators for functions which are computationally expensive and depend on a large number of input parameters. It is for this reason that we have chosen a deep learning model for approximating RIAF and jet SEDs.

Our approach can be summarized as follows. First we train a DL model on a grid of dozens of thousands of SEDs generated across the relevant parameter space for RIAFs and jets in LLAGNs. Once we have a trained model, we couple it to a MCMC ensemble sampler

that allows us to perform Bayesian fits to observations, obtaining the posterior distributions of the parameters. Other authors have also followed this path, though for different astronomical applications (e.g. Asensio Ramos and Ramos Almeida 2009; Pacheco-Sanchez et al. 2019; Fathivavsari 2020). For example, Asensio Ramos and Ramos Almeida (2009) used a technique based on the combination of two ML methods: principal analysis component (PCA) and NNs — PCA for dimensionality reduction and the NNs are used to interpolation, similarly to our case.

Our framework combines deep learning (which accelerates model computations) and MCMC (which provides posterior probability distributions for the many parameters involved). For the first time, this allows RIAF and jet models to be fitted to the observed multiwavelength LLAGN SEDs. We call it `AGNNES`: **A**ctive **G**alactic **N**uclei **Ne**ural network **S**ED generator.

This paper is structured as follows. In section 3.2, we present the details of the methods. In section 3.2.2, we present the NN architecture, its training and validation. In section 3.3 we present the results, which include a test of the model using Mock data, its performance for recovering the parameters of accreting SMBHs and applications to observations. We compare our results to the literature in section 3.4. Finally, section 3.5 presents a summary and some perspectives.

3.2 Methods

3.2.1 RIAF and jet

We used a semi-analytical approach to treat the RIAF radiation (N14) and included the contribution of synchrotron emission due to a relativistic jet, given that LLAGNs are usually radio-loud (e.g. Eracleous et al. 2010). In our model, we also included the synchrotron emission from a relativistic jet. We followed the same approach as N14 for the RIAF and jet calculations, in order to generate our training sample of SEDs[1]. Henceforth we will call this model as the fiducial one.

[1] The N14 source code can be found in: `https://github.com/rsnemmen/riaf-sed`

3.2.1.1 RIAF

We considered the calculation of an optically thin and geometrically thick two-temperature accretion flow with outer radius $r_0 = 10^4 R_S$ (R_S is the Schwarzschild radius; e.g. Narayan et al. 1998). Our assumptions to calculate its electromagnetic emission follow those of N14: (i) stationarity, (ii) a Shakura and Sunyaev (1973) α-viscosity, (iii) gravity is described with a pseudo-Newtonian potential (Paczyński and Wiita, 1980). The radiative transfer is treated carefully taking into account synchrotron, inverse Compton scattering (IC), and bremsstrahlung processes in the accretion flow.

RIAFs are prone to wind-launching (e.g. Yuan et al. 2012, 2015; Almeida and Nemmen 2020). We parameterize mass-loss in the wind as $\dot{M} = \dot{M}_0 (r/r_0)^s$ where s is related to the wind strength (higher values of s mean stronger winds) and $\dot{M}_0$ is the accretion rate at r_0. Following N14 we assume that s is limited to the range $0 \lesssim s \lesssim 1$ and $\dot{M}_0 < 0.01 \dot{M}_{\rm Edd}$. Of all the RIAF parameters, the ones that we vary in the training sample are the black hole mass M, fraction of turbulence energy transferred to the electrons δ, s and $\dot{M}_0$. The other parameters are fixed to $\alpha = 0.3$, $\beta = 0.9$ and $\gamma = 1.5$ (cf. N14 for more details).

We generated about 13000 RIAF SEDs, randomly sampling the parameters in the following ranges: $10^6 M_\odot \leq M \leq 10^{10} M_\odot$, $0.01 \leq \delta \leq 0.3$; $0 \leq s \leq 1$; $-5 \leq \log_{10}\left(\dot{M}_0/\dot{M}_{\rm Edd}\right) \leq -2$. When fitting a given source, however, we fixed the mass at the measured value, leaving only three free parameters in the fitting.

3.2.1.2 Jet

The jet component follows the treatment of N14. In brief, it consists of a stationary conical jet for which we compute the synchrotron emission, neglecting any self-synchrotron Comptonization. We vary the following parameters across the training data set: mass outflow rate $\dot{M}_j$, the leptonic energy distribution power-law index p and the fraction of energy density stored in electrons ϵ_e and magnetic field ϵ_B. We fix the remaining parameters to the following values: half-opening angle of 0.1 rad, bulk Lorentz factor $\Gamma = 2.9$ and line-of-sight angle 30°.

We generated about 130000 jet SEDs, randomly varying the above parameters in the following ranges: $2 \leq p \leq 3$, $-7 \leq \log_{10}\left(\dot{M}_j/\dot{M}_{\rm Edd}\right) \leq -2$, $-5 \leq \log_{10}\epsilon_e \leq -1$; $-5 \leq \log_{10}\epsilon_B \leq -1$.

3.2.2 Neural network

Our NN consists of a multilayer perceptron composed of neurons with weights structured in several layers (LeCun et al., 2015). The first layer has four and five neurons corresponding to the RIAF and jet cases, respectively. The number of neurons in the first layer matches the number of parameters that vary across the training dataset.

We built the architecture using the `GridSearch` technique (Bergstra and Bengio, 2012), which optimizes for the best hyperparameter values: the number of neurons in each hidden layer and the number of layers. We chose R^2 as the error function to quantify the training performance,

$$R^2 = 1 - \frac{\sum_j (P_j - T_j)^2}{\sum_j (P_j - \overline{P})^2}, \tag{3.1}$$

where T and P are the target and prediction values that will be compared, respectively. These values are summed over the index j, related to frequency bins. The model stops training when the lowest value of R^2 is found. We use this value for the final, best-fit DL model.

We adopt 3 hidden layers with 56, 60, and 99 neurons respectively for the RIAF model, and 4 hidden layers with 10, 44, 66, and 99 respectively for the jet one. Figure 3.1 summarizes the NN architecture. The number of neurons in the output layers — the last layer in the neural network — were chosen to match the number of frequency bins in the training datasets SEDs: 99 and 130 bins for the RIAF and jet, respectively. These numbers were defined in Almeida et al. (2018) and provide an adequate coverage of the radio-to-X-rays spectrum, which spans the range $\log(\nu/\mathrm{Hz}) = 9.12 - 20.88$.

During the training procedure, the NN prediction (i.e. the values of the output layer) is compared with the target values (i.e. the fiducial model) using the loss function $\mathcal{L}$ which gives the discrepancy between the target and prediction as a mean absolute error, $\frac{1}{n}\sum_i^{i=n} |x_i - x|$ The training uses backpropagation via gradient descent (Kelley, 1960; Ruder, 2016) to find the weights w_{ij} which minimize $\mathcal{L}(w_{ij})$. We use ReLU activation functions with the exception of the last layer, for which we adopt a linear activation. We adopt the Adam optimizer (Kingma and Ba, 2014).

We divide the training, validation and test sets as outlined in Table 3.1. We tested other architectures with different hyperparameters. However, we only present here the best model.

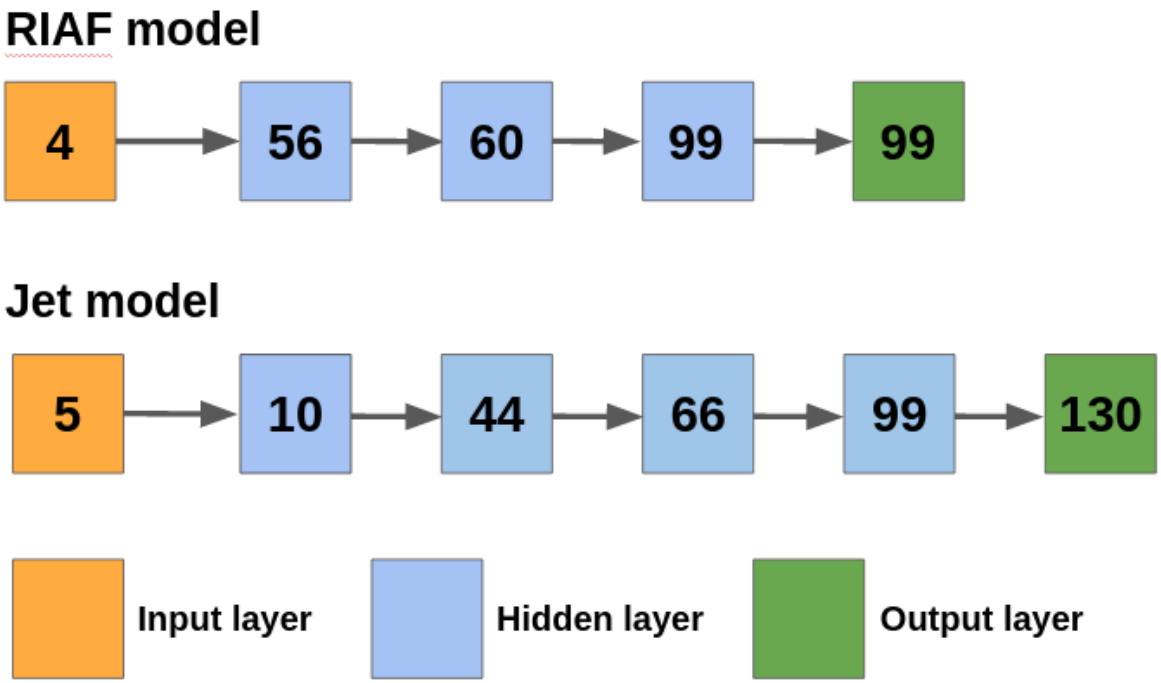

Figure 3.1: Overview of the neural network architecture. Squares represent layers: orange for input, blue for hidden and green for output. Numbers indicate the number of neurons in each layer. Arrows show the forward propagation or the direction of data flow.

	Percentage	RIAF SEDs	Jet SEDs
Training	70%	13377	92295
Validation	15%	2866	19777
Test	15%	2867	19777

Table 3.1 - Separation of dataset into training, validation, and test.

3.2.3 AGNNES's performance

LLAGN SED calculations are reasonably expensive. The fiducial code takes about a minute per RIAF spectrum[2]. AGNNES calculates the same SED in 0.3 ms, in other words a factor of 4×10^5 acceleration compared to the original RIAF code. The corresponding speedup factor for jet calculations is about 500. This allowed us to implement more robust statistical methods to LLAGN SED fitting compared to previous approaches.

We stress that AGNNES should be regarded as an interpolator which approximates the results of the fiducial models. The trade-off for the huge speedup in the computations is the introduction of systematic, small errors in the SEDs. In order to compare AGNNES' predictions with the validation data set, we defined ΔSED as the "distance" between the target (the fiducial models) and prediction (AGNNES results) at a specific frequency,

$$\Delta\,\mathrm{SED}(\nu) \equiv \log_{10}(\nu L_\nu)_{\mathrm{target}} - \log_{10}(\nu L_\nu)_{\mathrm{AGNNES}} \tag{3.2}$$

Averaging over all frequencies, we find $\langle \Delta\,\mathrm{SED} \rangle_\nu = 0.05$ and 0.01 dex for the RIAF and jet cases, respectively. These values quantify AGNNES' systematic uncertainty in predicting SEDs. In practice, though, AGNNES' systematic uncertainties will not be relevant in real applications since those are smaller than the usual uncertainties affecting LLAGN flux measurements.

Further comparisons of AGNNES predictions with instances of the validation set demonstrated that our approach reproduces very well the fiducial model, on average (cf. Appendix A.2).

3.2.4 Fitting Method

Most of previous work comparing SED models and observations does not consist of actual model fitting. For instance, Yu et al. (2011); Nemmen et al. (2014); Almeida et al. (2018) determine the best match between model and observations visually after a certain number of attempts. Such approaches judge the goodness of fit by eye rather than using a statistical technique and do not provide any likelihood distributions on the similarity between model and data. The main reason is that SED calculations are computationally

[2] This depends of course on the specific hardware and parameters set. The different desktop workstations that we used took between 0.5 and 2 minutes.

expensive, as mentioned before. This prevents a thorough exploration of the vast multidimensional parameter space of the models, which is required in most fitting methods such as maximum likelihood or Bayesian inference. For instance, generating 10^5 SEDs would require approximately two months of wall time with serial model calculations. Faster SED calculations allow robust fits thereby bringing RIAF and jet models to the realm of statistics. This was the main motivation behind this work.

We implemented the fitting procedure using the MCMC ensemble sampler `emcee` (Foreman-Mackey et al., 2013). `emcee` estimates the posterior distributions for the parameters given the observations, **where we adopt the likelihood function**

$$\Theta = \sum_i \frac{[\log_{10}(L_i) - \log_{10}(L_{\rm NN}(\nu_i))]^2}{\sigma_i^2}. \tag{3.3}$$

with ν_i and L_i being the frequency and luminosity; $L_{\rm NN}(\nu_i)$ is the luminosity calculated by the NN model for a given frequency ν_i; σ_i is the observed uncertainty. We adopted flat priors on all parameters within the parameter ranges described in section 3.2.1. Our MCMC chain starts with 300 walkers with over 30000 steps. We neglect the initial 20% steps as burn-in. The exact value of N depends on the type of model (RIAF or jet). We estimated the MCMC convergence using the integrated autocorrelation time (τ) implemented in `emcee` following the Goodman and Weare (2010) method, such that $N/50 \gtrsim \tau$.

3.3 Results

In this section, we first present detailed tests demonstrating the ability of `AGNNES` of accurately recovering the ground truth parameters from a sample of fiducial SEDs. We then present three observational applications of the method for M87, NGC 315 and NGC 4261, aiming at constraining the RIAF and jet parameters that best-fit the observed SEDs.

3.3.1 Tests

We tested the hability of `AGNNES` for recovering the ground truth parameters from known SEDs, randomly selected from the test set. Here we present the results of two tests for the RIAF and jet. For each case, we selected a random SED from the test set and from this SED selected only eleven different points, equally spaced in log frequency. For the first test (Test 1), we did not perturb the luminosities and considered a Gaussian uncertainty of

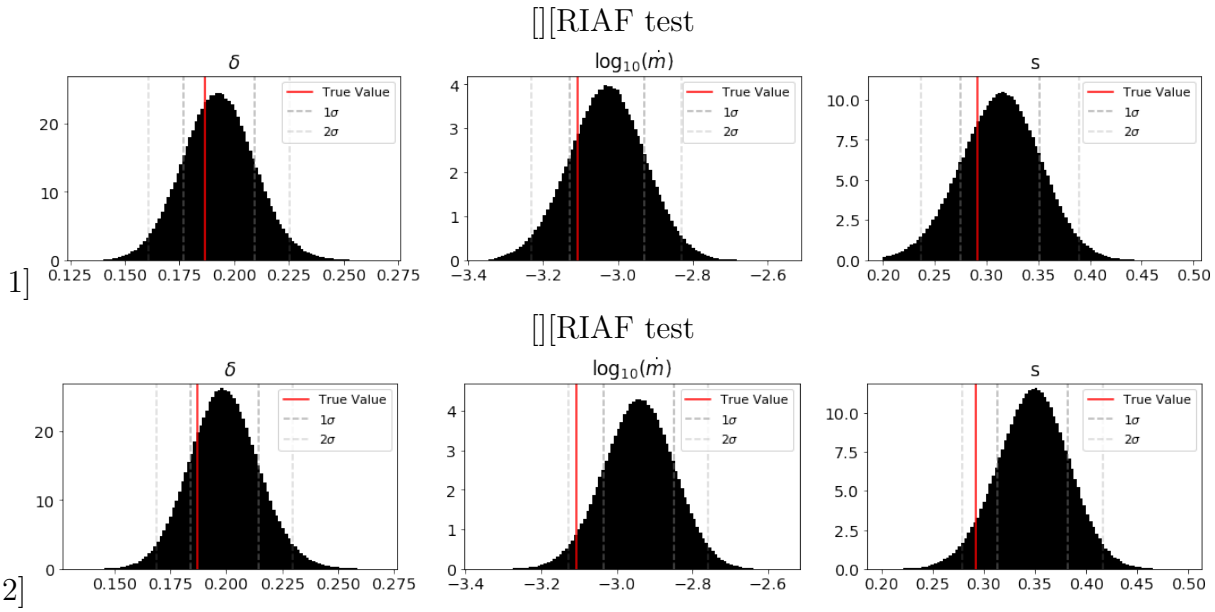

Figure 3.2: Posterior distribution of parameters for the RIAF model tests. The dashed vertical lines indicate the 1σ and 2σ confidence bands. The vertical solid red lines indicate the ground truth.

20%. In the second test (Test 2), we perturbed the luminosities by up to 30% of its value (i.e. we introduced an intrinsic dispersion) and also considered Gaussian uncertainties of 20%.

We show the posterior probability distributions of parameters resulting from these tests in Figures 3.2 and 3.3 for the RIAF and jet. See Table 3.2 for the corresponding values and standard deviations.

As can be seen in the figures, `AGNNES` successfully recovers the true values with different levels of accuracy. For the RIAF case, the posterior distributions are consistent with the ground truth values within 1σ for the Test 1, and 2σ for the Test 2. We deem the results of Test 2 acceptable in face of the considerable intrinsic dispersion introduced. For the jet test case, our method recovers the ground truth values within 1σ.

`AGNNES` displays a systematic bias towards larger values of the RIAF parameters. This bias is likely due to the fact that `AGNNES` systematically overpredicts the fiducial SEDs by 0.02 dex which then gets translated to slightly biased posteriors. However, this bias should be negligible in the face of observational uncertainties of real LLAGN SEDs.

3.3.2 Applications to observations

For all sources, we assume flat priors on all parameters and fix the mass to the best measurement available in the literature. Whenever we have a specific luminosity without

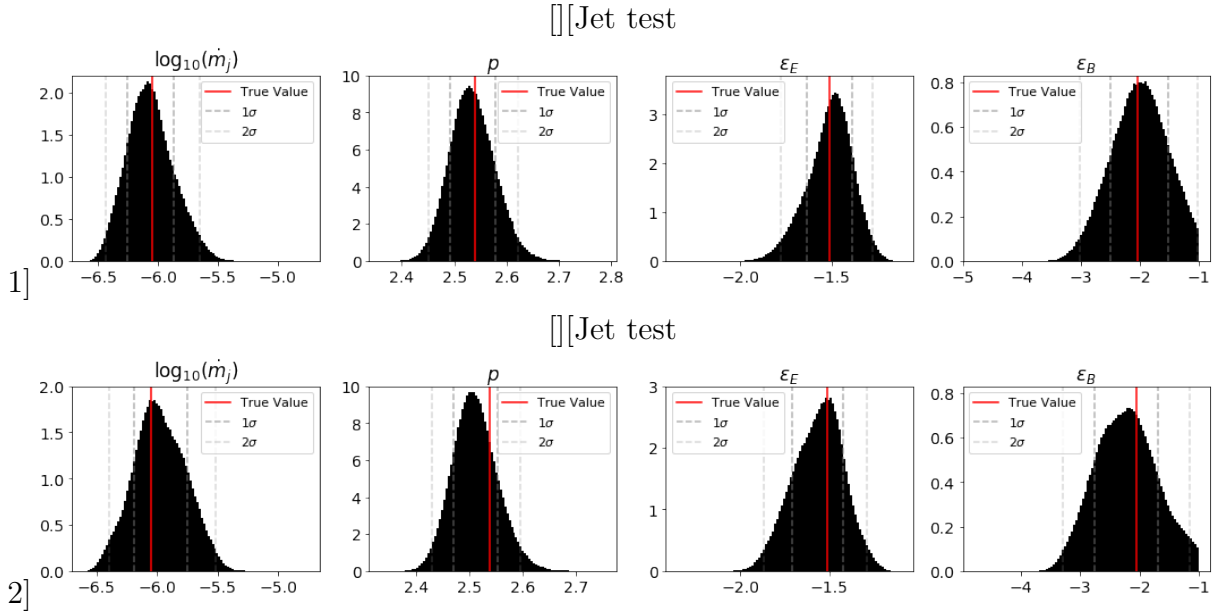

Figure 3.3: Posterior distribution of parameters for jet model tests. The notation is the same as in Figure 3.2.

Test	δ	$\dot{M}_0$ ($\dot{M}_{\rm Edd}$)	s
Ground truth	0.19	-3.11	-0.29
RIAF 1	$0.19^{+0.02}_{-0.02}$	$-3.04^{+0.10}_{-0.10}$	$0.31^{+0.04}_{-0.04}$
RIAF 2	$0.20^{+0.02}_{-0.02}$	$-2.94^{+0.09}_{-0.09}$	$0.35^{+0.03}_{-0.04}$

Test	$\dot{M}_j$ ($\dot{M}_{\rm Edd}$)	p	ϵ_e	ϵ_B
Ground truth	-6.05	2.54	-1.51	-2.04
Jet 1	$-6.07^{+0.21}_{-0.18}$	$2.53^{+0.04}_{-0.04}$	$-1.50^{+0.11}_{-0.14}$	$-1.99^{+0.48}_{-0.51}$
Jet 2	$-5.99^{+0.23}_{-0.21}$	$2.51^{+0.04}_{-0.04}$	$-1.55^{+0.13}_{-0.16}$	$-2.23^{+0.54}_{-0.53}$

Table 3.2 - `AGNNES` test results. Error bars correspond to 68% confidence intervals.

a corresponding uncertainty, we assume it to be 0.05 dex. Appendix A.1 lists the corresponding data for all sources considered. Table 3.3 displays all the fits. The last column corresponds to the reduced χ^2, or χ^2_ν.

Object	δ	$\dot{M}_0$ ($\dot{M}_{\rm Edd}$)	s	$\dot{M}_j$ ($\dot{M}_{\rm Edd}$)	p	ϵ_e	ϵ_B	χ^2_ν
M87	–	–	–	$6.6^{+0.7}_{-0.8} \times 10^{-7}$	$2.54^{+0.04}_{-0.04}$	$4.7^{+0.4}_{-0.3} \times 10^{-2}$	$1.2^{+0.3}_{-0.2} \times 10^{-5}$	10.0
NGC 315	$0.30^{+1\times10^{-4}}_{-2\times10^{-4}}$	$9.98^{+0.02}_{-0.04} \times 10^{-3}$	$0.582^{+0.002}_{-0.002}$	$1.5^{+0.2}_{-0.2} \times 10^{-5}$	$2.6^{+0.1}_{-0.1}$	$5.4^{+1.3}_{-1.3} \times 10^{-3}$	$1.1^{+0.2}_{-0.1} \times 10^{-5}$	9.4
NGC 4261	$0.30^{+2\times10^{-4}}_{-3\times10^{-4}}$	$9.99^{+0.01}_{-0.01} \times 10^{-3}$	$0.731^{+0.006}_{-0.005}$	$1.0^{+2.1}_{-1.0} \times 10^{-5}$	$2.4^{+0.4}_{-0.3}$	$2.4^{+4.6}_{-2.4} \times 10^{-4}$	$1.3^{+3.4}_{-1.3} \times 10^{-4}$	54.3
NGC 4261 (No UV)	$0.30^{+2\times10^{-4}}_{-3\times10^{-4}}$	$9.91^{+0.07}_{-0.15} \times 10^{-3}$	$0.645^{+0.003}_{-0.004}$	$8.9^{+18.6}_{-8.9} \times 10^{-6}$	$2.4^{+0.4}_{-0.3}$	$3.3^{+6.4}_{-3.3} \times 10^{-4}$	$1.3^{+3.3}_{-1.3} \times 10^{-4}$	115.3 ($9.1^{\dagger}$)

Table 3.3 - Resulting parameters from fitting `AGNNES` to our LLAGN sample. † Neglects UV observations.

3.3.2.1 M87

The elliptical galaxy M87 harbours a SMBH of $6.5 \times 10^9 M_\odot$ at a distance of 16 Mpc of distance from us (Akiyama et al., 2019b). The source presents strong radio emission due to a prominent relativistic jet. We took the SED data for this source from Prieto et al. (2016) (cf. their Table 4). We treated observations with lower spatial resolution as upper limits. Figure 3.4 displays the observations.

We tested models considering both the RIAF and jet emission, but in the end we achieved the best results when we considered only the jet. This is not surprising, since the jet emission is a known feature of M87 (Doeleman et al., 2012). It was not possible to produce an acceptable fit to the SED using the RIAF model for this source. The resulting posterior distributions on the jet parameters is shown in Figure 3.5 and listed in Table 3.3.

For M87 and the other sources, we obtained a high value for χ^2_ν. A value of $\chi^2_\nu \approx 1$ indicates a good match between the model and observation within the uncertainties. In our models, we have found $\chi^2_\nu \gg 1$. There are two main reasons for these high reduced chi-squared values. First, the observational data has considerable amounts of intrinsic scatter. Second, by assuming an uncertainty of 0.05 dex for the many observations without errors obtained in the literature, we are likely underestimating the errors thereby leading to increased χ^2_ν values. Finally, our model is subject to many simplifications, thus the value of χ^2_ν should be taken with a grain of salt.

3.3.2.2 NGC 315 and NGC 4261

NGC 315 is an elliptical galaxy at a distance of 64 Mpc, located at the Pisces constellation. It contains a SMBH of $2.08 \times 10^9 M_\odot$ (Boizelle et al., 2021). NGC 4261 is another elliptical galaxy at a distance of 30 Mpc, located at the Virgo cluster.It harbours a SMBH with $1.67 \times 10^9 M_\odot$ (Boizelle et al., 2021). de Menezes et al. (2020) presented the observations for both LLAGNs and a performed similar modelling for the this source, though without a proper statistical fit.

For both sources, we treated the optical data as upper limits due to the high likelihood of contamination by stellar populations (e.g. N14) which are not the focus of the present work. Figures 3.6 and 3.8 display the SEDs for NGC 315 and NGC 4261, respectively. The posterior distributions for the parameters are shown in Figures 3.7 and 3.9. The data

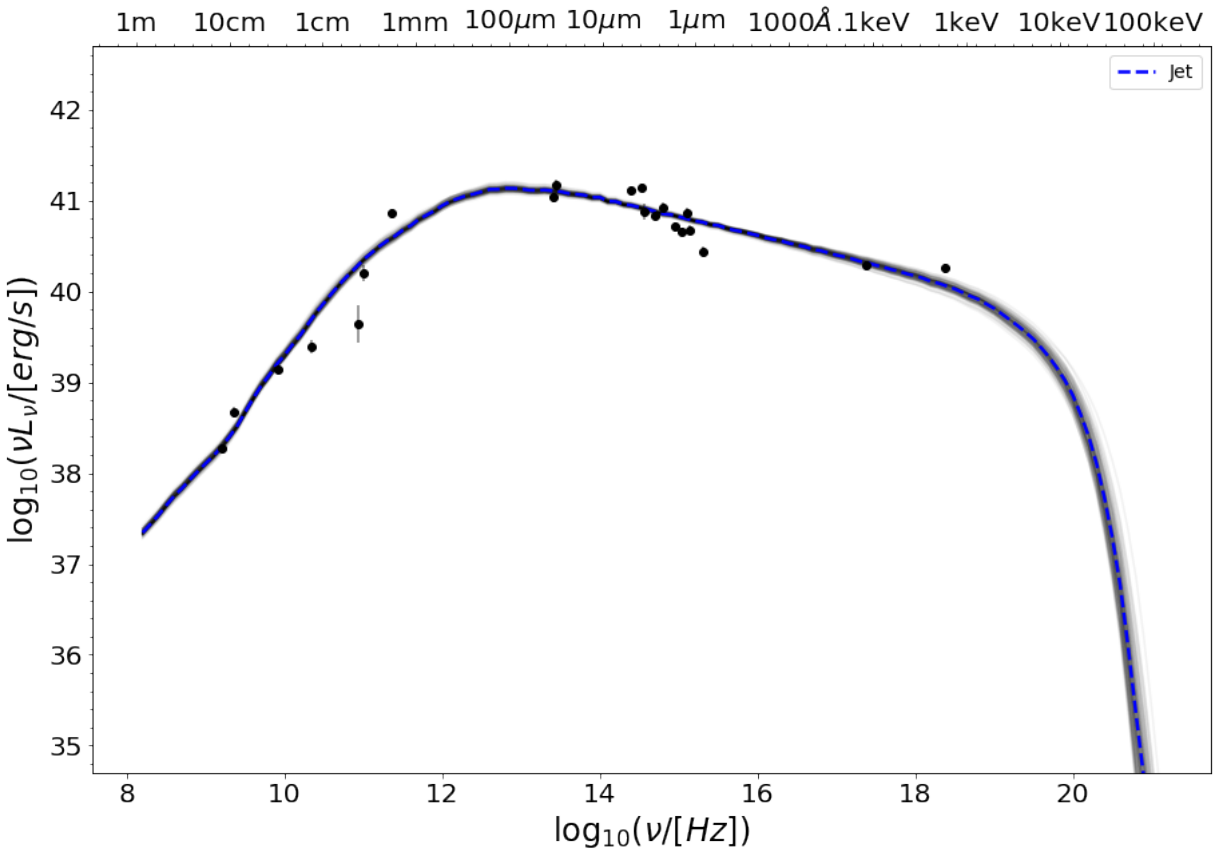

Figure 3.4: M87 SED best fit. We fit the data using only the jet model. The grey shaded area is a set of one hundred curves generated by the MCMC method and illustrates the uncertainties in the fit.

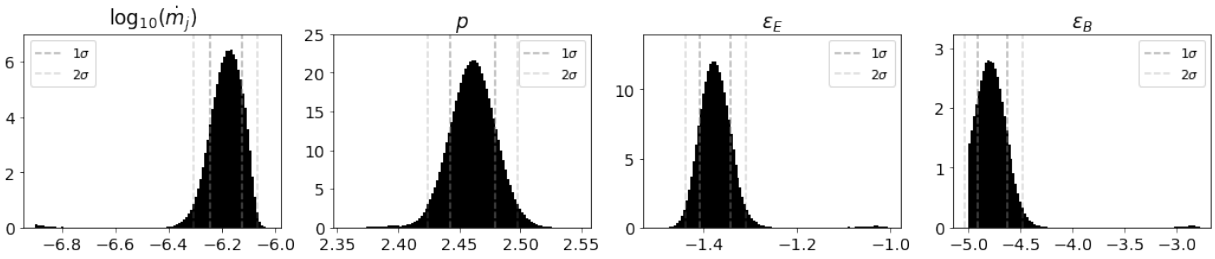

Figure 3.5: Posterior distributions of the fitted parameters for M87. The vertical lines delimit the 1σ and 2σ regions.

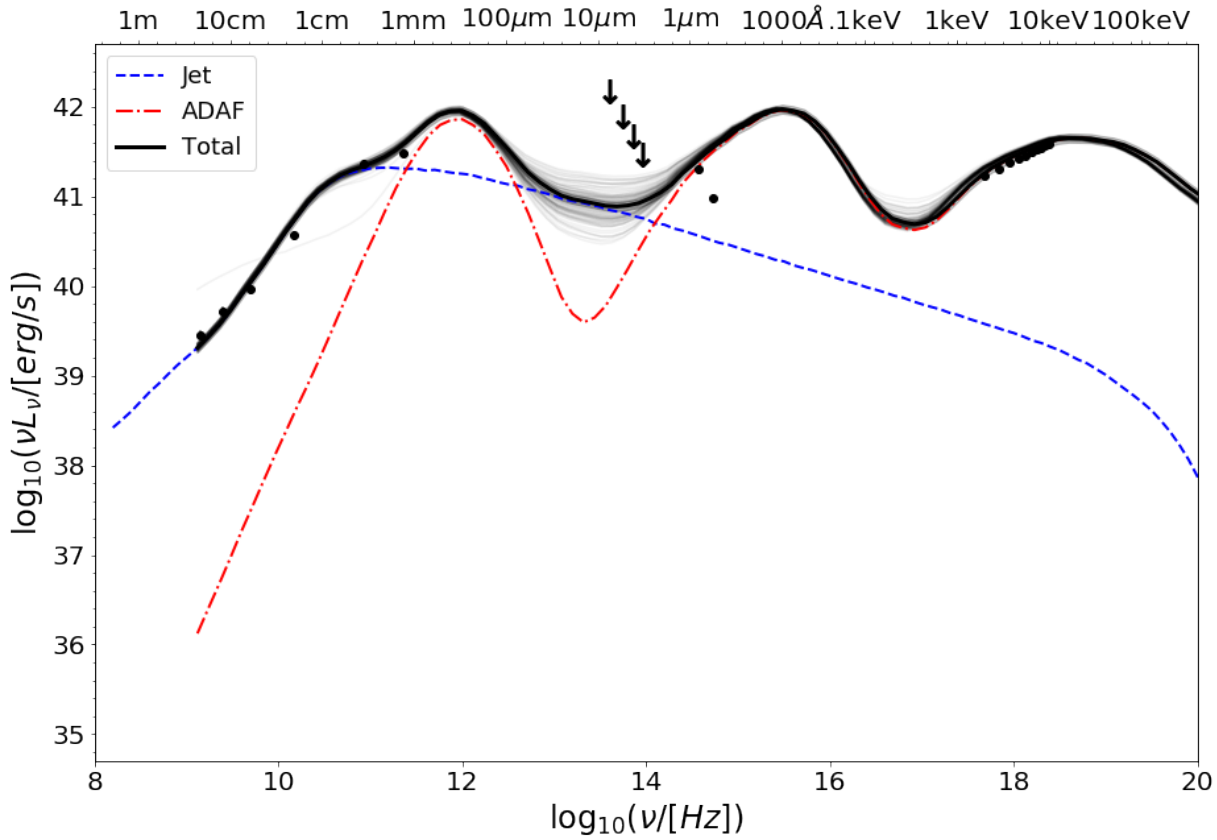

Figure 3.6: NGC 315 SED best fit. The red dashed line corresponds to the RIAF model; the blue dash-dotted line represents the synchrotron jet contribution; the black solid line is the sum of the two components.

points used in the fits are listed for completeness in Tables A.2 and A.3.

Given the hardness of the X-ray spectrum of NGC 315 and NGC 4261, it was not possible to obtain an acceptable fit to these SEDs with a pure jet model since the jet predicts softer emission (e.g. Wu et al. 2007; N14). Therefore, we treated the jet as the subdominant component. Because only a few radio data points are anchoring the jet emission, the number of free parameters is comparable to the number of points thus this component is underconstrained. This translates into broad posteriors for most of the jet parameters, especially in the case of NGC 4261 where p and ϵ_B are poorly constrained.

Both sources prefer higher mass accretion rates, as can be seen in the $\dot{M}_0$ posterior distributions in Figures 3.7 and 3.11, which are skewed towards the maximum value of the training set, $\max\left(\dot{M}_0\right) = 10^{-2}\dot{M}_{\rm Edd}$. We chose this value of $\max\left(\dot{M}_0\right)$ in this work because this is close to the critical accretion rate above which the RIAF solution ceases to exist, transitioning to a cold thin disk (e.g. Done et al. 2007). This is the reason why the posterior distributions for $\dot{M}_0$ are truncated. A future analysis should allow for larger

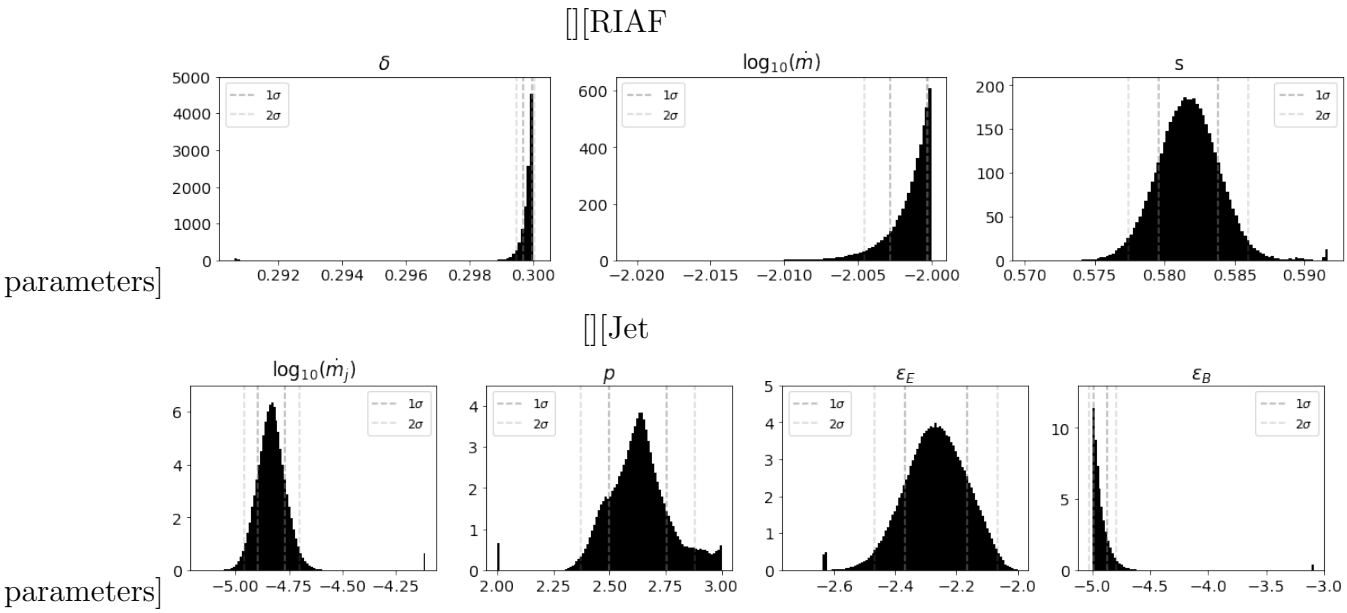

Figure 3.7: NGC 315 SED posterior distribution of the fitted parameters. Conventions are the same as in Figure 3.5.

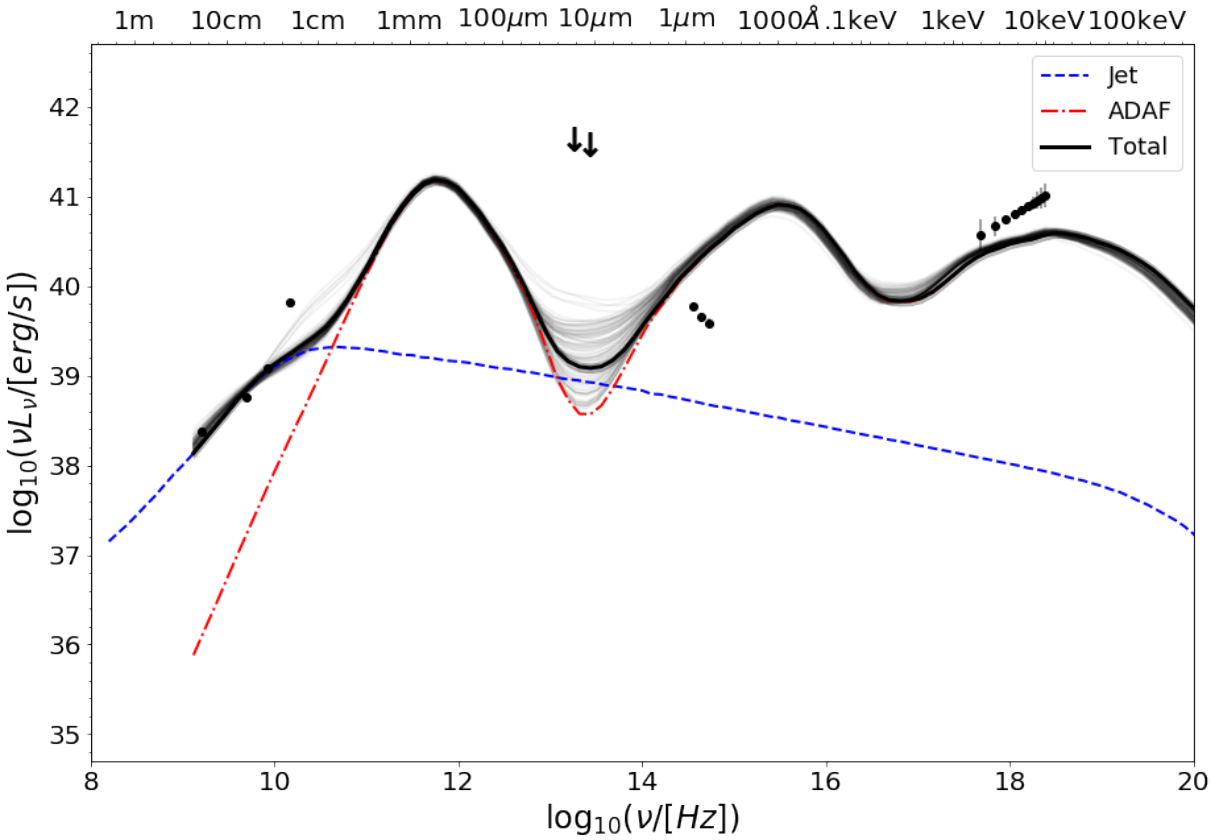

Figure 3.8: NGC 4261 SED best-fit. Conventions are the same as in Figure 3.6.

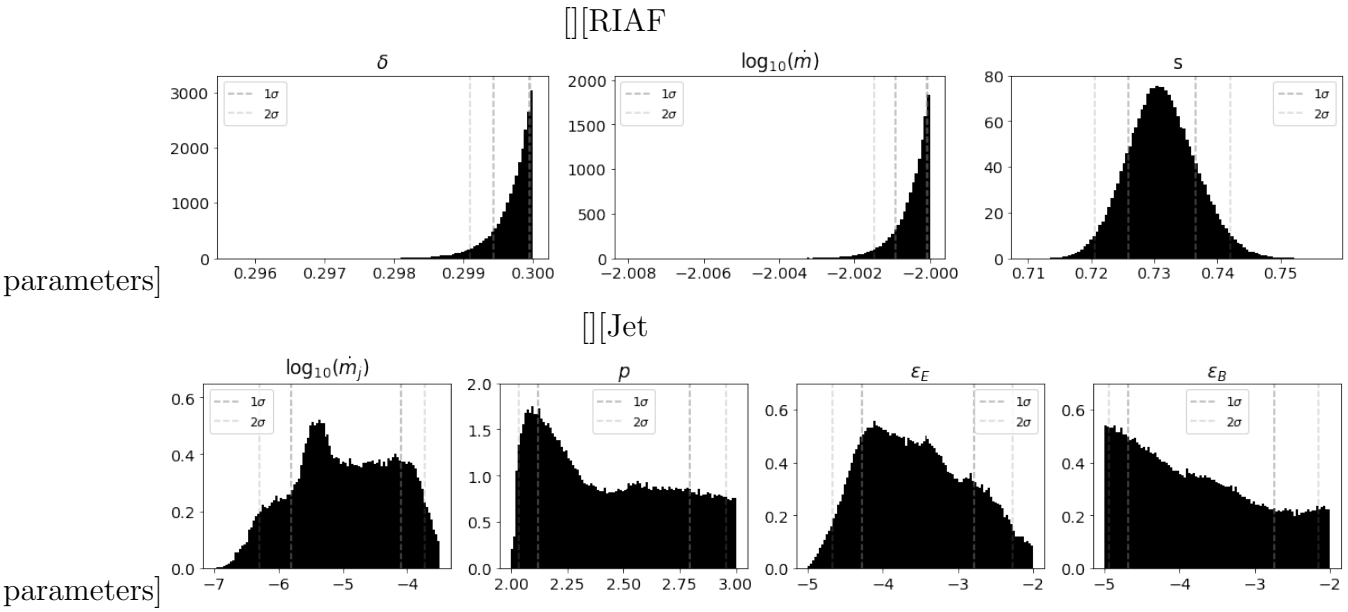

Figure 3.9: Posterior distributions of parameters for NGC 4261. Conventions are the same as in Figure 3.5.

accretion rates and also include the thin disk component in the trained spectral model. This will allow the modeling of brighter AGNs with larger accretion rates. In particular, the X-ray emission for NGC 4261 could be better described with $\dot{M}_0 = 3.2 \times 10^{-2} \dot{M}_{\rm Edd}$ (de Menezes et al., 2020).

For both NGC 4261 and NGC 315, the models were not able to fully explain the optical-UV emission. In both cases, the RIAF emission severely overpredicts the optical-UV observations. This disparity is probably due to strong extinction due to dust affecting the optical-UV band. The observations in this band do not capture the true emission of the central engine (e.g. N14).

For NGC 4261, the X-ray observations are visibly offset from the model (Figure 3.8). If one tries to reproduce both the optical-UV and X-ray observations for this source then the X-ray band is underpredicted. On the other hand, when we ignore the optical-UV data during the modeling—similarly to N14—then the goodness-of-fit of the X-ray band improves significantly, as shown in the new Figure 3.10.

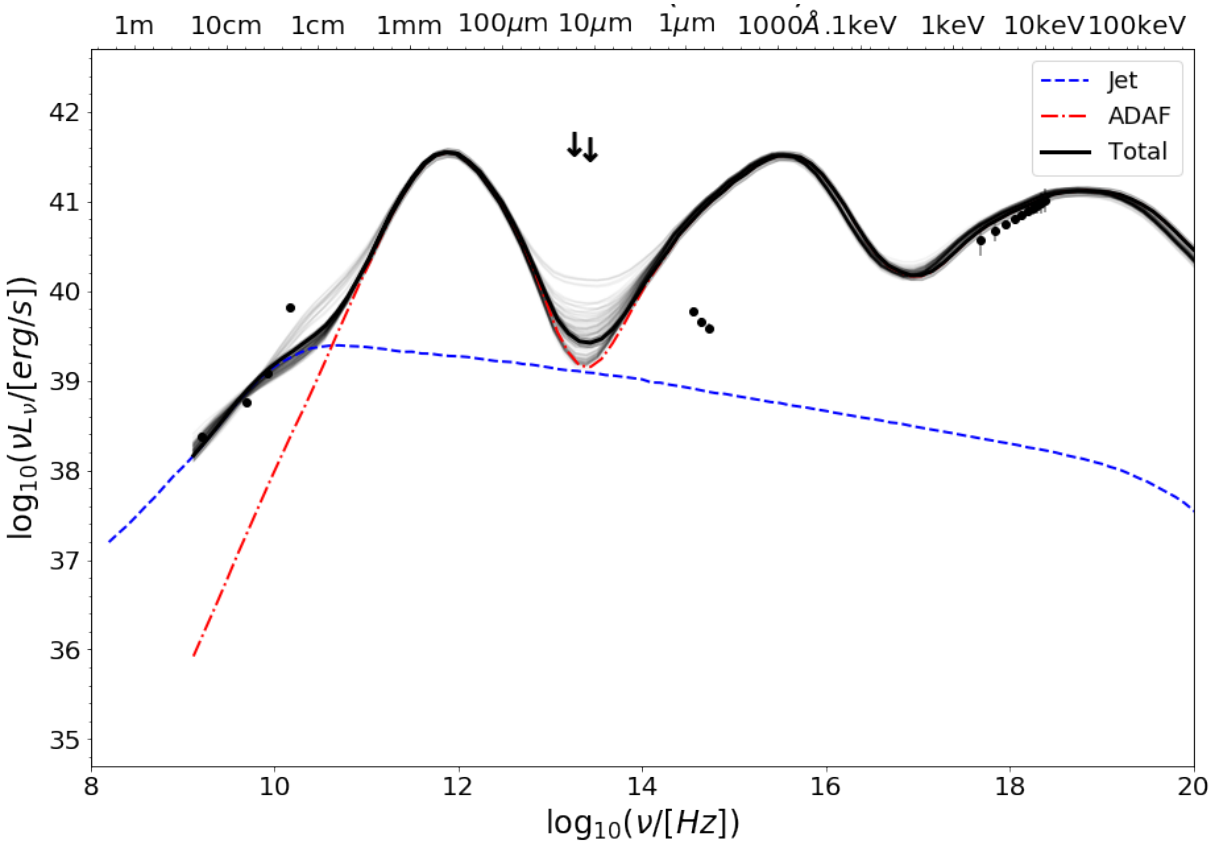

Figure 3.10: NGC 4261 SED model that does not take into account the optical-UV observations. Conventions are the same as in Figure 3.6.

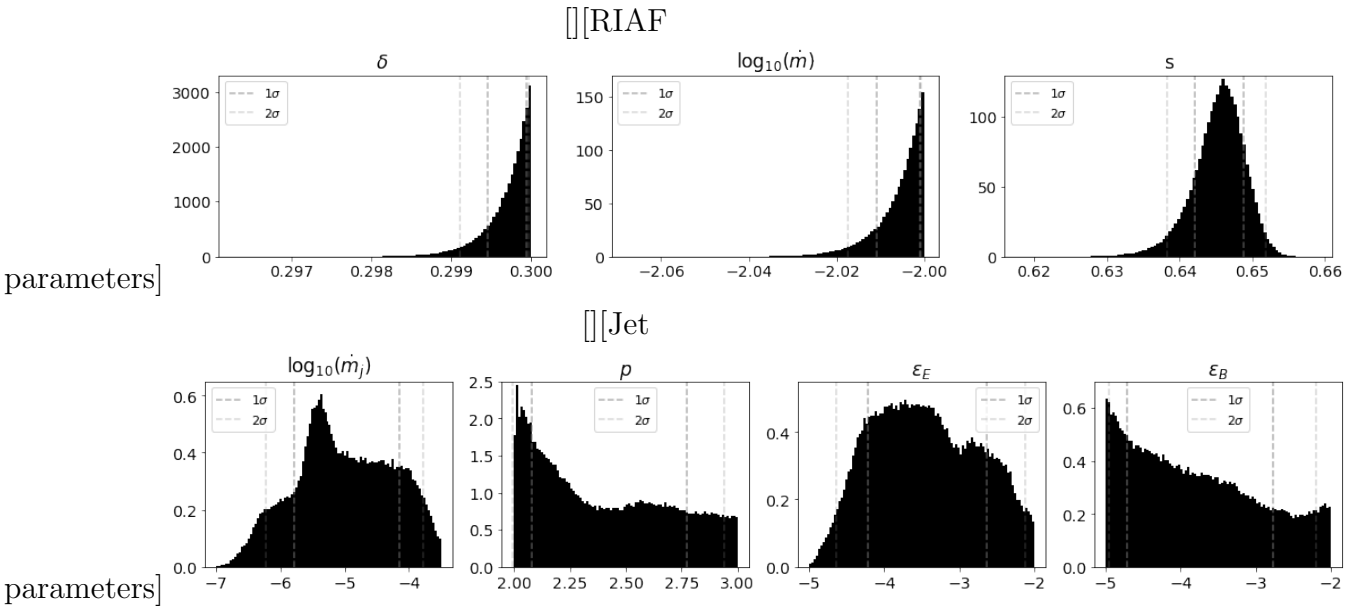

Figure 3.11: NGC 4261 SED (neglecting the UV data points) posterior distribution of the fitted parameters. Conventions are the same as in Figure 3.5.

3.4 Discussion

3.4.1 Model accuracy

It is not worth accelerating calculations that give incorrect results: one will only arrive faster at the wrong answers.

With this is mind, accurate spectral models is an essential feature of `AGNNES`. Figure 3.12 is another demonstration of its accuracy. We took the best-fit parameters obtained in section **??** and computed the SEDs using the fiducial models. As can be seen in the figure, `AGNNES`'s models are virtually indistinguishable from the fiducial ones, with only small deviations of typically less than 0.1 dex in luminosity.

3.4.2 Comparison with previous work

It is worth comparing the parameters computed from the SED fits of M87, NGC 4261 and NGC 315 in section **??** with previous studies.

Abdo et al. (2009) modelled the source considering the synchrotron self-Compton emission from a jet blob, which is a different approach than the route followed in the present work. They adopt a broken power-law energy distribution for the electrons as opposed to single power-law used in this work. Nevertheless, they find roughly a similar ratio of the electron to magnetic field energy densities. They also agree that M87's observations are well described by a jet-dominated model.

Recently, Bandyopadhyay et al. (2019) modelled M87 with a RIAF and jet combination. They included a population of nonthermal electrons in the RIAF (we did not) and thereby managed to fit the $\approx$ 100 GHz bump. Bandyopadhyay et al. found $\dot{M}_j/\dot{M}_{\rm Edd} = 10^{-8}$, $p = 2.5 - 2.6$, $\epsilon_E = 9 \times 10^{-4}$, and $\epsilon_B = 6 \times 10^{-4}$. Their parameter estimates are in severe disagreement with ours. For instance, while p presents a 2σ tension, $\dot{M}_j/\dot{M}_{\rm Edd}$ is at a $> 5\sigma$ tension with our result. The reason for the disagreement is that their modelling approach is quite different from ours. While we imposed that the jet dominates the emission at all energies, in Bandyopadhyay et al. the jet is subdominant, with an energetically relevant RIAF component.

de Menezes et al. (2020) carried out the NGC 4261 and NGC 315 modelling using the same fiducial models as the present work, though adopting iterative procedures and fitting by eye. They found the following RIAF parameters for NGC 315: $\delta = 0.3$, $\dot{M}/\dot{M}_{\rm Edd} =$

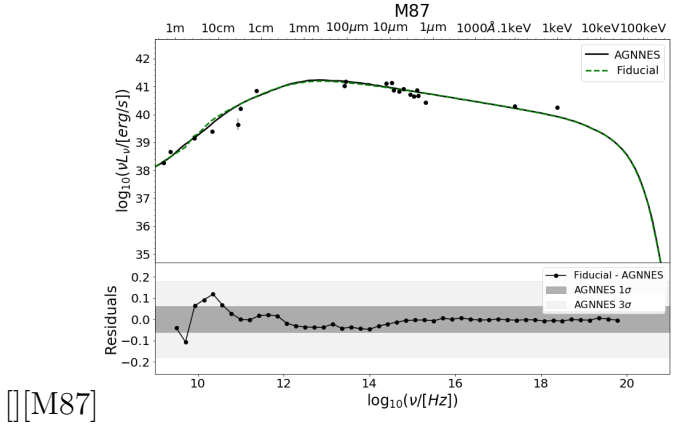

[][M87] [][NGC

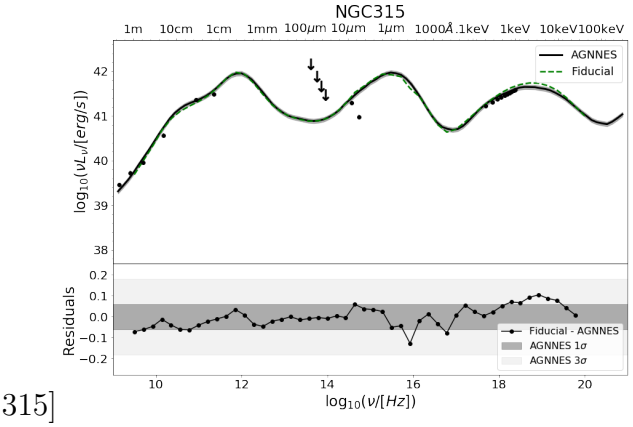

315] [][NGC

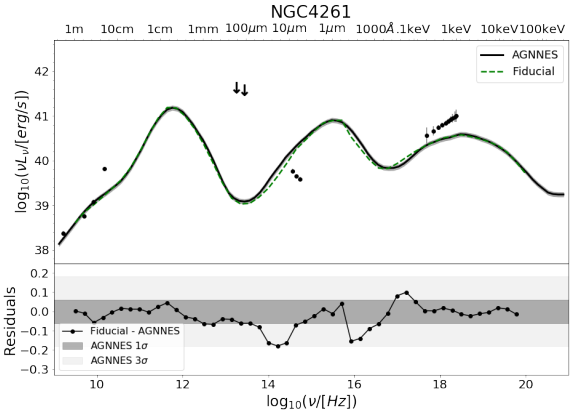

4261] [][NGC 4261 (No

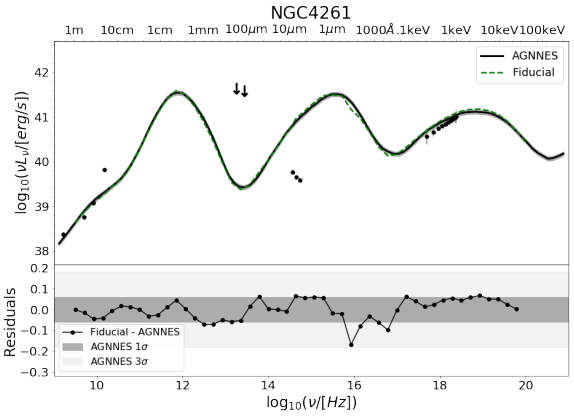

UV)]

Figure 3.12: Comparison between the SEDs calculated with `AGNNES` and the fiducial model for each of the cases presented in section **??**. The figure in lower right corner corresponds to the NGC 4261 model not taking into account the optical-UV data. In each figure, the top panel compares the `AGNNES` (solid black line) and the fiducial model (dashed green line) while the bottom panel shows the residuals. The darker gray and light gray regions indicate the 1σ and 3σ systematic uncertainty of the fits.

8.9×10^{-3}, and $s = 0.50$. The values of $\dot{M}$ and s do not agree with ours even though both approaches reproduce the observations. We think that De Menezes et al. found a point in the parameter space close to a different local minimum in the likelihood function than what `AGNNES` found.

For NGC 4261, de Menezes et al. (2020) reported the values $\delta = 0.3$, $\dot{M}/\dot{M}_{\rm Edd} = 3 \times 10^{-2}$, and $s = 0.91$, i.e. an accretion rate much higher than our results. Similarly to the case of NGC 315 discussed in the paragraph above, it is likely that the likelihood function is non-convex. Our fit converged to one of the local minima in this surface, and De Menezes et al. may have found an entirely different minimum corresponding to their larger value of s, which implies larger accretion rates in order to account for the same luminosity.

NGC 4261 was also modelled by N14 with the same fiducial model used here. Most of their parameter estimates are at a $> 5\sigma$ tension with the `AGNNES` fit reported here, with the exception of δ, $\dot{M}_j$, p and ϵ_e which agree with our estimates within 2σ. The reason for the mismatch are the different modelling approaches: Nemmen et al. fix the value of s to 0.3 and they only use the radio emission to constrain the jet whereas we used all wavebands.

3.4.3 Shortcomings

The fiducial models used to to train `AGNNES` have several shortcomings; `AGNNES` inherited all of them. For instance, both the RIAF and jet models are severe simplifications to the turbulent reality of jets and accretion flows: the RIAF is assumed to be axisymmetric and stationary; the RIAF magnetic field only contributes through an isotropic, magnetic pressure. We have neglected the self-synchrotron Comptonization in the jet, although there is some evidence for its relevance in LLAGNs (Nagar et al., 2005; Finke et al., 2008; Takami, 2011).

Another shortcoming is related to the non-simultaneity of the observations modelled in section **??**. Variability certainly has an impact on the resulting parameters, though this is hard to quantify without a detailed monitoring campaign for each source

Finally, `AGNNES`' performance shines when used within the parameter space of the training set. Some sources require the exploration of values outside the set, such as Sgr A*. In this particular case, the mass accretion rate is too small and outside the $\dot{M}$-range of the present work. As such, `AGNNES` is unable to fit Sgr A*'s SED. `AGNNES` best reprodu-

ces LLAGN SEDs with $(\nu L_\nu)_{\rm peak} > 10^{36}$ erg/s. In the future, we may explore expanded training sets with broader ranges of accretion rates and black hole masses.

3.5 Summary

We have developed a deep learning method capable of computing radio-to-X-rays spectra of RIAFs and relativistic jets much faster than previous approaches. Combining this fast and accurate DL interpolator with a Markov chain Monte Carlo ensemble sampler enables Bayesian parameter inference for LLAGN spectral energy distributions: the `AGNNES` model. We demonstrated that the method can successfully recover the ground-truth parameters of a Mock set of SEDs, such as the mass accretion rates. We used `AGNNES` to fit the SEDs of three LLAGNs: M87, NGC 315 and NGC 4261. The posterior distributions of parameters are largely consistent with previous models.

Those interested in using this method should keep firmly in mind the following points:

(i) `AGNNES` works for black hole masses in the range $10^6 M_\odot \leq M \leq 10^{10} M_\odot$ and mass accretion rates in the range $-5 \leq \log_{10}\left(\dot{M}_0/\dot{M}_{\rm Edd}\right) \leq -2$ ranges. These ranges encompass the training data set.

(ii) `AGNNES` was trained on electromagnetic spectra generated from RIAF and jet models subject to several simplifications, most importantly their simplified dynamics and geometry.

(iii) `AGNNES` should work best when the SED includes observations from radio to X-rays, even if just a handful of data points. Our model was not tested when there is a lack of radio observations for example, or when there is missing X-ray data. We cannot guarantee the performance of the model in such conditions.

Future works should expand the training data set to encompass broader ranges of masses and lower accretion rates. Another possibility in the future is to improve the physics of the flows and radiation. For example, one could train a deep neural network on SED models from general relativistic magnetohydrodynamic simulations (e.g. Ryan et al. 2015; Akiyama et al. 2019a). Despite its limitations, we hope `AGNNES` will be useful for astronomers looking forward to better understand underfed SMBHs. This is another demonstration of the power of deep learning algorithms for astrophysical problems.

Chapter 4

RIAF winds and Feedback

4.1 Introduction

Once an early-type galaxy forms, that does not mean it will remain quiescent forever and ever. Early-type galaxies have abundant gas (e.g. Binette et al. 1994) and should also accrete fresh amounts of it. If all this gas cooled and led to star formation, the global stellar mass density should currently be larger than observations by a factor of a few (Benson et al., 2003). Furthermore, the number of galaxies in the red sequence is steadily growing since the peak epoch of quasars and starbursts (e.g. Bell et al. 2004; Bundy et al. 2006). This implies that galaxies are still transitioning to quiescence. Taken together, these are evidence for an unceasing feedback process which suppresses star formation in red sequence galaxies and keeps it quenched.

In this work, we explore the possibility that the feedback mechanism keeping these galaxies quiescent is due to winds from accreting supermassive black holes (SMBH) hosted in low-luminosity active galactic nuclei (LLAGN). This idea is quite promising because most SMBH activity in the nearby universe is happening in LLAGNs (e.g. Ho 2008). These SMBHs are weakly accreting via radiatively inefficient accretion flows (RIAF; Yuan and Narayan 2014). RIAFs are prone to producing profuse winds (e.g. Yuan et al. 2015; Almeida and Nemmen 2020; Yang et al. 2021). In addition, there is increasing evidence of a new class of early-type galaxies hosting galaxy-scale LLAGN winds from spatially resolved spectroscopy (Cheung et al., 2016; Roy et al., 2021; Sánchez et al., 2021) and radio observations (Roy et al., 2018).

Given the potential importance of AGN winds in quenching star formation at late times, here we perform an analytical study of LLAGN winds as a feedback mechanism.

We build a simplified model of RIAF winds based on the latest results from numerical simulations and analyze how the presence of an LLAGN could impact the gas and stellar content of a galaxy.

RIAF winds are very hot, subrelativistic and non-collimated. They carry considerable energy, with powers up to 1% of the rest mass energy $\dot{M}c^2$ associated with accretion (Almeida and Nemmen, 2020). The kinetic and thermal energy of the ejected wind must be deposited in the environment, and its most plausible fate is depositing its energy in the interstellar medium. By exploring the properties of these winds and their impact on the host galaxy, we tackle the following questions: Are LLAGN powerful enough to quench star-formation in an early-type galaxy? Can LLAGN winds keep a red-and-dead galaxy quiescent?

This paper is structured as follows. In section 4.2, we present the details of the model. In section 4.3 we present the results, which include the predicted relation between LLAGN power and star-formation quenching. We compare our results to the literature in section 4.4. Finally, section 4.5 presents a summary and some perspectives.

4.2 Model

In order to quantify the effect of LLAGN feedback, we approximated a galaxy as an isothermal sphere of dark matter with a fixed fraction of gas. The wind itself is an expanding sphere. In the following subsections, we describe our model in more details.

4.2.1 Galaxy

We followed Silk and Rees (1998) and modelled the galaxy as an isothermal sphere characterized by a velocity dispersion σ. Stars dominate the total mass of the galaxy's central region, and only a small fraction is gaseous corresponding to a fraction $f_g \approx 0.05 - 0.1$ of the total mass. The gas density profile is described as

$$\rho(R) = \frac{f_g \sigma^2}{2\pi G R^2}. \tag{4.1}$$

The total gas mass enclosed in a radius R is

$$M_{\rm gas}(R) = \int_0^R 4\pi r^2 \rho(r) dr = \frac{2 f_g \sigma^2 R}{G}$$
$$= 9.6 \times 10^9 f_g \left(\frac{\sigma}{200\,{\rm km/s}}\right)^2 \left(\frac{R}{1\,{\rm kpc}}\right) M_\odot \tag{4.2}$$

and is in the form of atomic hydrogen. The gravitational binding energy $E_{\rm gal}$ is

$$E_{\rm gal}(R) = \frac{3 G M_{\rm total} M_{\rm gas}}{5R} = \frac{6 M_G \sigma^2}{5}. \tag{4.3}$$

Adopting $f_g = 0.05$ and replacing equation (4.2) in (4.3) gives

$$E_{\rm gal}(R) = 4.5 \times 10^{56} \left(\frac{\sigma}{200\,{\rm km/s}}\right)^4 \left(\frac{R}{1\,{\rm kpc}}\right)\ {\rm erg}\ . \tag{4.4}$$

The system is isothermal with a temperature of $T_{\rm Gal} = 1.5 \times 10^6 \sigma_{200}^2$ K where $\sigma_{200} \equiv \sigma/200\,{\rm km/s}$.

4.2.2 LLAGN Energy Output

The LLAGN is able to inject a ΔE amount of energy into the galaxy via thermal winds given by $\Delta E = L_w \Delta t$ where L_w the wind power and Δt is the LLAGN lifetime. We parameterise the wind power as a fraction of the Eddington luminosity, $L_w = \eta L_{\rm Edd}$. Following Almeida and Nemmen (2020), the wind power is $\sim 0.1 - 1$ per cent of the rest-mass energy $\dot{M}c^2$ accreted by the SMBH. Given that for a LLAGN we expect $\dot{M} \lesssim 10^{-3} \dot{M}_{Edd}$ and $L_{\rm Edd} \equiv 0.1 \dot{M}_{\rm Edd} c^2$, we have $\eta \lesssim 10^{-4}$. Thus, in our calculations we assume $\eta = 10^{-4}$ and thereby

$$\Delta E = 4 \times 10^{56} \left(\frac{\eta}{10^{-4}}\right) \left(\frac{M_{\rm BH}}{10^9\,{\rm M}_\odot}\right) \left(\frac{\Delta t}{1\,{\rm Myr}}\right)\ {\rm erg}. \tag{4.5}$$

With these considerations, the impact of the AGN on the host galaxy increases trivially with its lifetime and decreases with the distance from the SMBH, as can be seen by taking the ratio of the LLAGN energy output with the galactic gravitational binding energy,

$$f_{\rm AGN} \equiv \frac{\Delta E}{E_{\rm gal}} = 0.24 \left(\frac{\Delta t}{1\,{\rm Myr}}\right) \left(\frac{R}{1\,{\rm kpc}}\right)^{-1} \left(\frac{M_{\rm BH}}{10^9\,{\rm M}_\odot}\right)^{0.22}, \tag{4.6}$$

where we have used the $M - \sigma$ relation of McConnell et al. (2011). As we will see, the LLAGN energy output can be comparable to the galactic gravitational binding energy.

4.2.3 Star-formation

Star formation usually occurs in giant molecular clouds (GMC), massive reservoirs of cold gas prone to star formation.

In our model, we assume that the entirety of the wind kinetic power couples to GMCs and is converted to thermal energy. This approximation amounts to $f_{\rm AGN}$ translating directly into the fractional temperature increase caused by AGN feedback.

We describe the protostellar core mass function as

$$\frac{dN}{dlnM} = N_0\Big(\frac{M}{M_0}\Big)^{-\xi}, (M \lesssim M_0). \tag{4.7}$$

following Rosolowsky (2005); Dib et al. (2008). Equation (4.7) gives the distribution of protostellar cores inside GMCs as a function of mass and sizes. We considered in our model dense clouds with $M_0 \lesssim 100 M_\odot$ and $0.3 \leq \xi \leq 2.7$.

Cores able to generate stars are those with masses exceeding the Jeans mass

$$M_J = 20M \odot \Big(\frac{T}{10\ \rm K}\Big)^{1.5}\Big(\frac{n}{100\ \rm cm^{-3}}\Big)^{-0.5}. \tag{4.8}$$

Assuming a constant external pressure around the cloud and $n = 100\ \rm cm^{-3}$, this simplifies to $M_J = 20 M_\odot (T/10\ \rm K)^2$.

4.3 Results

4.3.1 Energetics

Figure 4.1 illustrates the characteristic values of $f_{\rm AGN}$ for a range of AGN timescales and distances. The figure indicates that an LLAGN can inject a significant amount of energy into the inner 10 kpcs of the host galaxy. The effect is more prominent in galaxies with more massive SMBHs. For instance, a galaxy hosting a $10^8 M_\odot$ SMBH can undergo a 10% temperature increase in the innermost 2 kpc in one million years; a $10^9 M_\odot$ SMBH active over 2 Myr with achieve a heating fraction higher than 50%. Moreover, if the LLAGN is active for 5 Myr or longer, the galactic heating within 5 kpc will be energetically relevant regardless of the mass.

4.3.2 How far does the wind reach?

Simulations suggest strong thermal winds coming from RIAFs, with powers reaching up to one percent of the rest mass associated with accreted gas (Almeida and Nemmen,

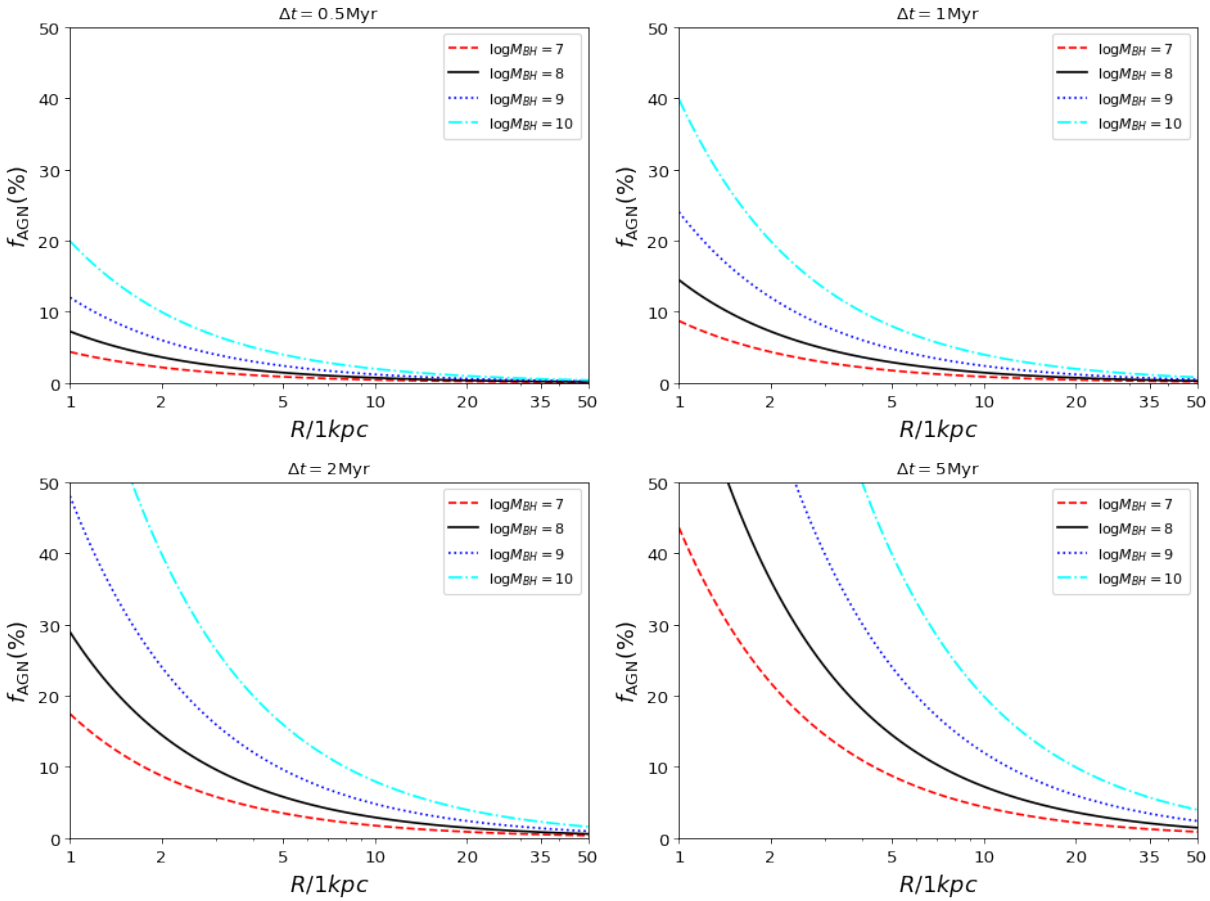

Figure 4.1: Energy injected by LLAGN winds scaled by the galactic binding energy as a function of distance to the supermassive black hole, based on equation 4.6. Different AGN durations and black hole masses are displayed in the different panels, with the mass in solar masses.

2020). These winds have thermal energies greater than the gravitational binding energy, which means they have enough energy to escape the black hole's gravitational sphere of influence. Nevertheless, the spatial extent of these winds remains an open question. We investigated the wind extension using two different approaches. In the first one, we model the wind as expanding bubble which cools via bremsstrahlung. In the second one, we consider a central heating source and a heat transfer through the gas—here, the wind carries only energy and not mass. The calculations are better described in Appendix C.

In the first scenario, we computed the distance travelled by the bubble front over the cooling time, $R_{\rm wind} = vt_{\rm cool}$, where we assume $v = 300$ km s^{-1} (Cheung et al., 2016; Almeida and Nemmen, 2020) and that the density follows $\rho_{\rm wind} \propto r^{\alpha}$. The resulting expression is

$$R_{\rm wind} = \left(\frac{5.9 \times 10^{-5} \eta^{-1} \sigma_{200}^2 M^{\alpha}}{10^{7\alpha}\sqrt{1-\alpha}} \right)^{\frac{1}{1+\alpha}} \text{ kpc} \tag{4.9}$$

where we assume $\eta \sim 10^{-4}$, related to the efficiency of the wind production. This is roughly

$$R_{\rm wind} \gtrsim \begin{cases} 3 \text{ kpc}, \alpha < -0.1 \\ 100 \text{ kpc}, \alpha < -0.3 \end{cases} \tag{4.10}$$

We find that for $\alpha < 0$, the wind can reach distances larger than ten kpc which are beyond the visible size of most galaxies.

For the second case, we numerically solve the one-dimensional radial heat transfer equation for a sphere made of hydrogen with a central heat point source,

$$\frac{1}{r^2}\partial_r(r^2 \partial_r T) = \frac{\rho c_P r^2}{\kappa} \partial_t T + Q_{\rm AGN} \tag{4.11}$$

We modelled the AGN impact as a spherical boundary with constant temperature and hotter than the medium. This can be translated as the boundary condition in equation (4.12) and initial condition in equation (4.13). For practical reasons, we assumed $r_{\rm AGN} = 0$ since the AGN scales are too small compared to the galaxy.

$$T(r = r_{\rm AGN}) \leq T_{AGN}, \tag{4.12}$$

$$T(t = 0, r) = \begin{cases} T_{\rm AGN}, & r \leq r_{\rm AGN} \\ T_{\rm gal}, & r > r_{\rm AGN} \end{cases}. \tag{4.13}$$

Solving equation (4.11) and assuming the characteristic values from Fabian et al. (2005) (their equation 4), we found that the resulting temperature profile follows $T(R) \propto R^{-1}$. This is the same radial dependence as in equation (4.6). After about 5 Myr, even gas at kiloparsec scales will undergo a 20% temperature increase. For this model $R_{\rm wind}$ is the radius at which $\lim_{r \to R_{\rm wind}} T(r) = T_{\rm gal}$. We find that typically $R_{\rm wind} \gtrsim 1$ kpc.

Both models indicate that winds can get to the galactic outskirts, reaching distances up to kpc. We stress that the multiscale physics of the ISM and its interaction with hot winds is quite complex. We leave the numerical modeling of these phenomena for a future work.

4.3.3 Star formation quenching

The number of protostellar cores able to collapse and form stars can be calculated using equations 4.7 and 4.8 as

$$\mathcal{N}(M \geq M_J) = \int_{M_J}^{M_0} N(M) dM. \tag{4.14}$$

We use $\mathcal{N}$ to quantify the impact of LLAGN feedback in quenching star formation by computing it in two different ways: $\mathcal{N}_0$ is the number of protostellar cores able to collapse into stars when the AGN effect is not taken into account, whereas $\mathcal{N}_{\rm AGN}$ is the corresponding quantity with the AGN turned on. In particular, we are interested in comparing how much lower $\mathcal{N}_{\rm AGN}$ is compared to $\mathcal{N}_0$ as a function of the main accreting BH parameters: the BH and mass accretion rate. When estimating $\mathcal{N}_0$, we consider a temperature $T_{\rm PC} \sim 10$K and corresponding Jeans mass is denoted by M_J (see equation (4.8)); for $\mathcal{N}_{\rm AGN}$, we adopt $T_{\rm PC}^{\rm AGN} = (1 + f_{\rm AGN}) T_{\rm PC}$ as the AGN increase the average temperature and the appropriate Jeans mass is $M_J^{\rm AGN}$. This implies that $M_J < M_J^{\rm AGN}$. Protostellar cores with masses in the range $M_J < m < M_J^{\rm AGN}$ will suffer gravitational collapse when the impact of the AGN is not considered; they would not if the LLAGN is taken into account.

We define the fraction of star formation quenched by the LLAGN—the quenching fraction Q—as

$$Q \equiv 1 - \frac{\mathcal{N}_{\rm AGN}}{\mathcal{N}_0} = 1 - \frac{1 - (M_J/M_0)^{1-\xi} (1 + f_{\rm AGN})^{2-2\xi}}{1 - (M_J/M_0)^{1-\xi}}. \tag{4.15}$$

where ξ is a power-law index and M_0 is the mass scale related to the protostellar core mass distribution, (see equation (4.7)). The meaning of Q is the following: in the extreme case when $Q = 1$, the entirety star formation is aborted due to AGN feedback; on the other

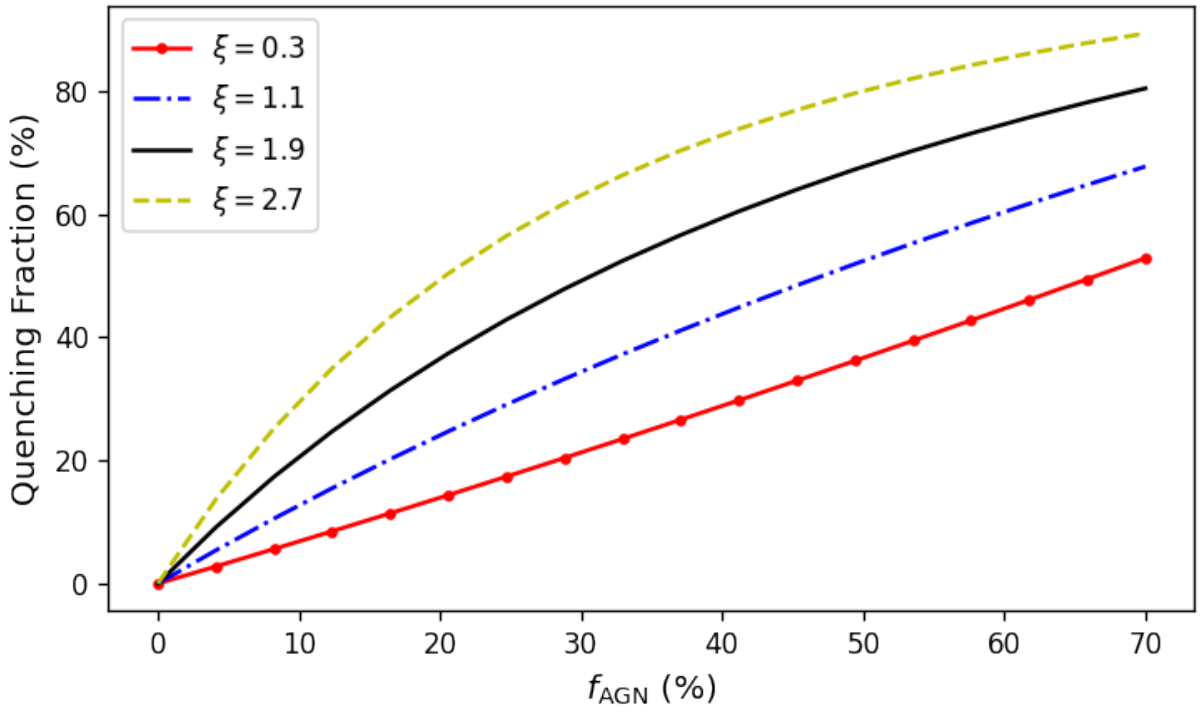

Figure 4.2: The quenching fraction as a function of the average heating of the region. As the temperature increases, the fraction of shut-down stellar formation sites increases. The different lines represent the different distribution possibilities for the protostellar cores (see equation (4.7)).

hand, when $Q = 0$ there is no quenching at all. Therefore, Q and the star-formation rate are inversely correlated.

We plot in figure 4.2 the relation between star formation quenching and the AGN heating fraction $f_{\rm AGN}$, where we explore the dependence on the parameter ξ (equation (4.7)). As expected, quenching becomes more pronounced as the amount of energy dumped by the LLAGN increase though this proceeds in a nonlinear fashion.

Figure 4.3 illustrates the dependence of quenching on the SMBH mass accretion rate. Each shaded region with a different color corresponds to a given SMBH mass, with the interior spanning all allowed ξ values assuming $R = 20$ kpc (a typical galaxy size). The different panels explore the impact of the duration of the LLAGN activity varying from 1 Myr (upper left panel) to 50 Myr (bottom right panel). For illustration, let's consider a SMBH accreting at the $10^{-3}\dot{M}_{\rm Edd}$ level. If its mass is $10^8 M_\odot$ ($10^9 M_\odot$) and the wind is produced for only 1 Myr, it can quench less than one per cent (5%) of star formation in the host galaxy; now, if the LLAGN is active for 10 Myr, it can quench up 10% (30%); moreover, if it is active for 50Myr, the quenched grows to 40% (60%).

Figure 4.4 displays the SMBH activation function for effective AGN feedback, as pre-

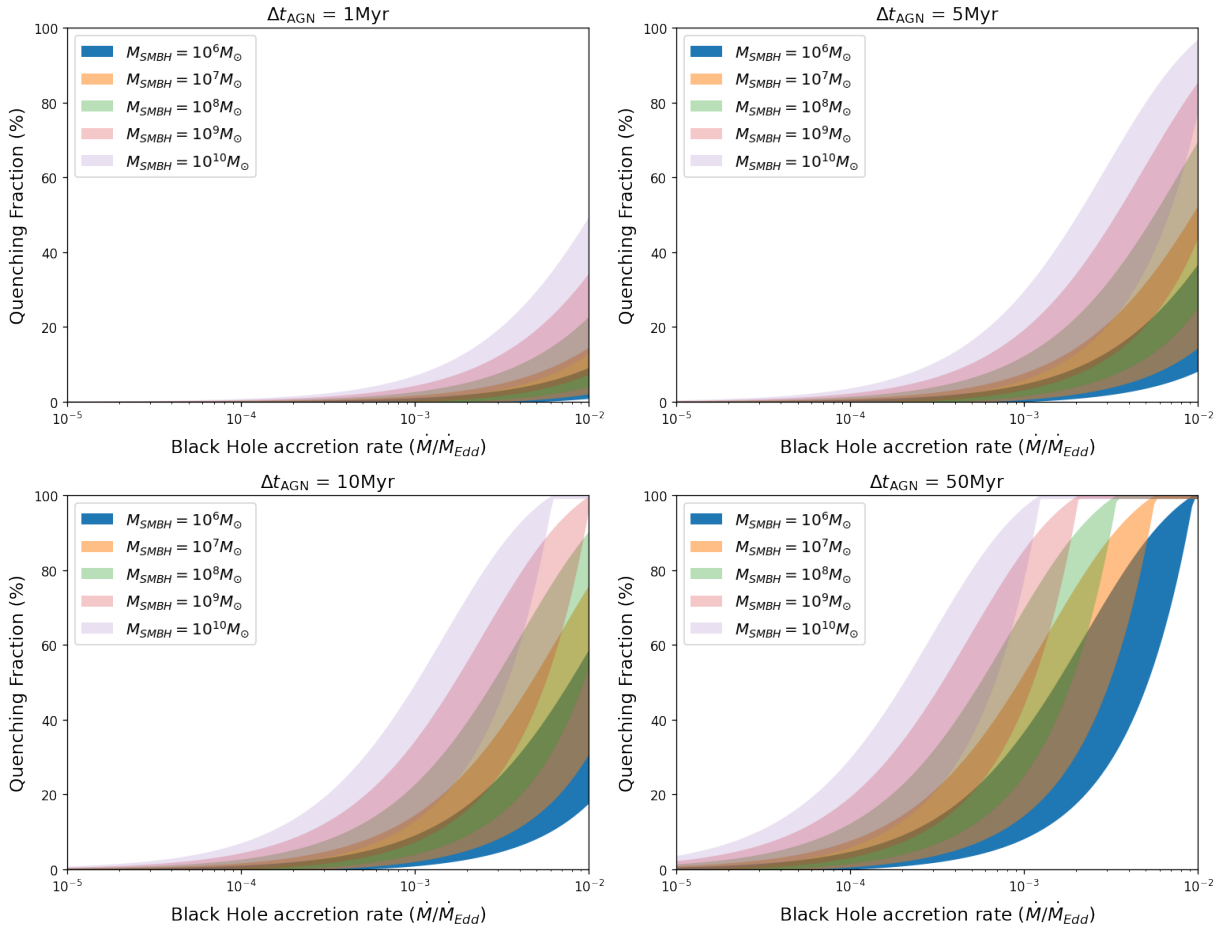

Figure 4.3: The plot shows the quenching fraction inside a region of 20kpc as a function of the LLAGN accretion rate. The increase in the accretion rate has a significant effect on the gas. Each colour represents a different SMBH mass. We can observe the importance of the system's total mass; the quenching only occurs for the most massive SMBHs. The three different panels refer to the LLAGN activity time Δt, long-lived LLAGN have a much more substantial impact on the gas temperature and subsequent quenching. The denoted regions represent the different distributions of the protostellar cores (see equation (4.7)); they are the region delimited by the lines shown in figure 4.2.

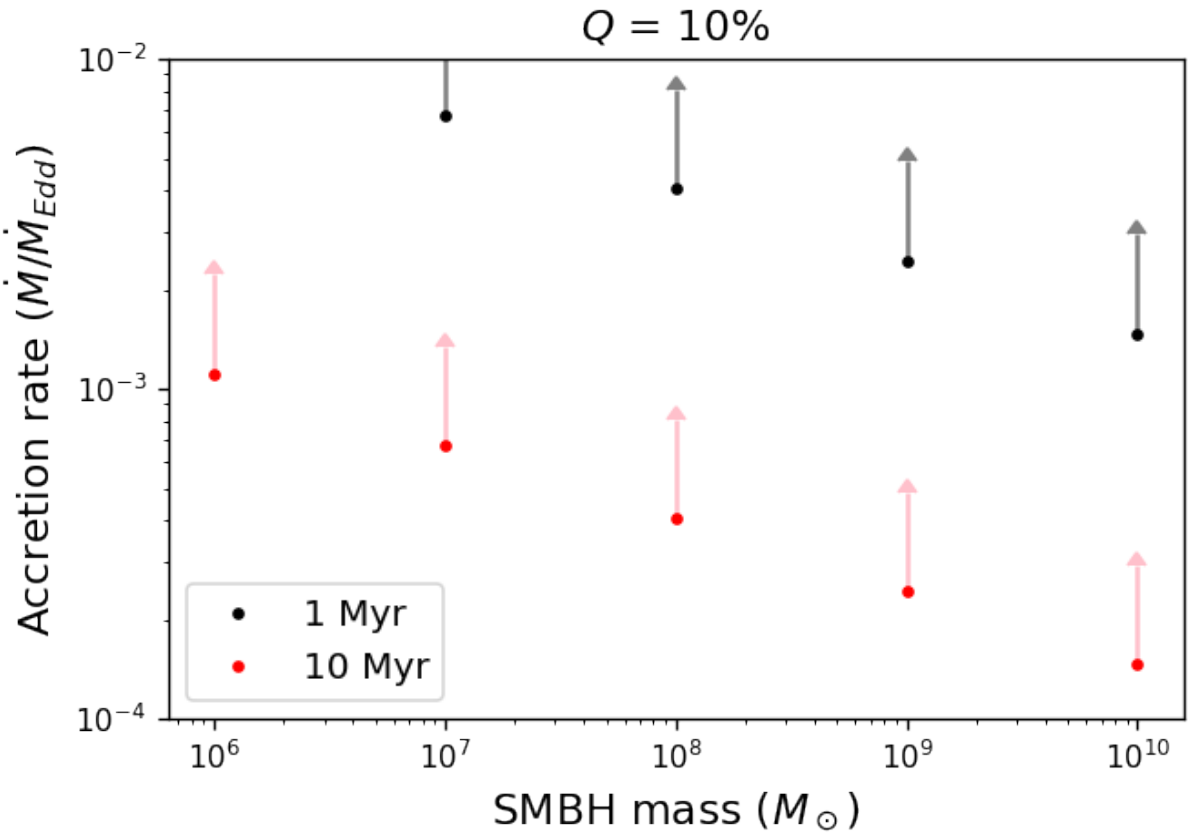

Figure 4.4: Family of accreting SMBH parameters required to produce quenching of star formation of at least ten per cent, as a function of BH mass. Black (top) and red (bottom) circles correspond to LLAGN lifetimes of 1 Myr and 10 Myr, respectively. This figure serve as a guide to evaluate whether a LLAGN feedback is effective as a function of black hole mass and accretion rate.

dicted in our calculations. This figure displays the family of accreting SMBH parameters required to produce a ten per cent quenching of star formation, i.e. the combination of mass accretion rates and masses that result in $Q = 0.1$. Figure 4.4 shows that a $10^8 M_\odot$ or $10^9 M_\odot$ SMBH that experiences an accretion episode lasting 1 Myr with $\dot{M} > 4 \times 10^{-3} \dot{M}_{\rm Edd}$ will be able to abort more than 10% of star formation in its host galaxy. For an accretion episode lasting 10 Myr, a $10^8 M_\odot$ SMBH needs $\dot{M} > 4 \times 10^{-4} \dot{M}_{\rm Edd}$ to significantly impact its host galaxy via winds; a $10^9 M_\odot$ SMBH needs $\dot{M} > 3 \times 10^{-4} \dot{M}_{\rm Edd}$.

Correspondingly, Figure 4.5 displays the wind power resulting in effective AGN feedback with $Q \geq 0.1$. Similarly to the story told in Figure 4.4, a $10^8 M_\odot$ SMBH that produces a wind lasting 1 Myr with power larger than 5×10^{39}erg s^{-1} will be able to abort more than 10% of star formation in its host galaxy. For winds lasting 10 Myr, a $10^8 M_\odot$ ($10^9 M_\odot$) SMBH needs a wind power larger than 4×10^{38}erg s^{-1} (2×10^{39}erg s^{-1}) for effective quenching.

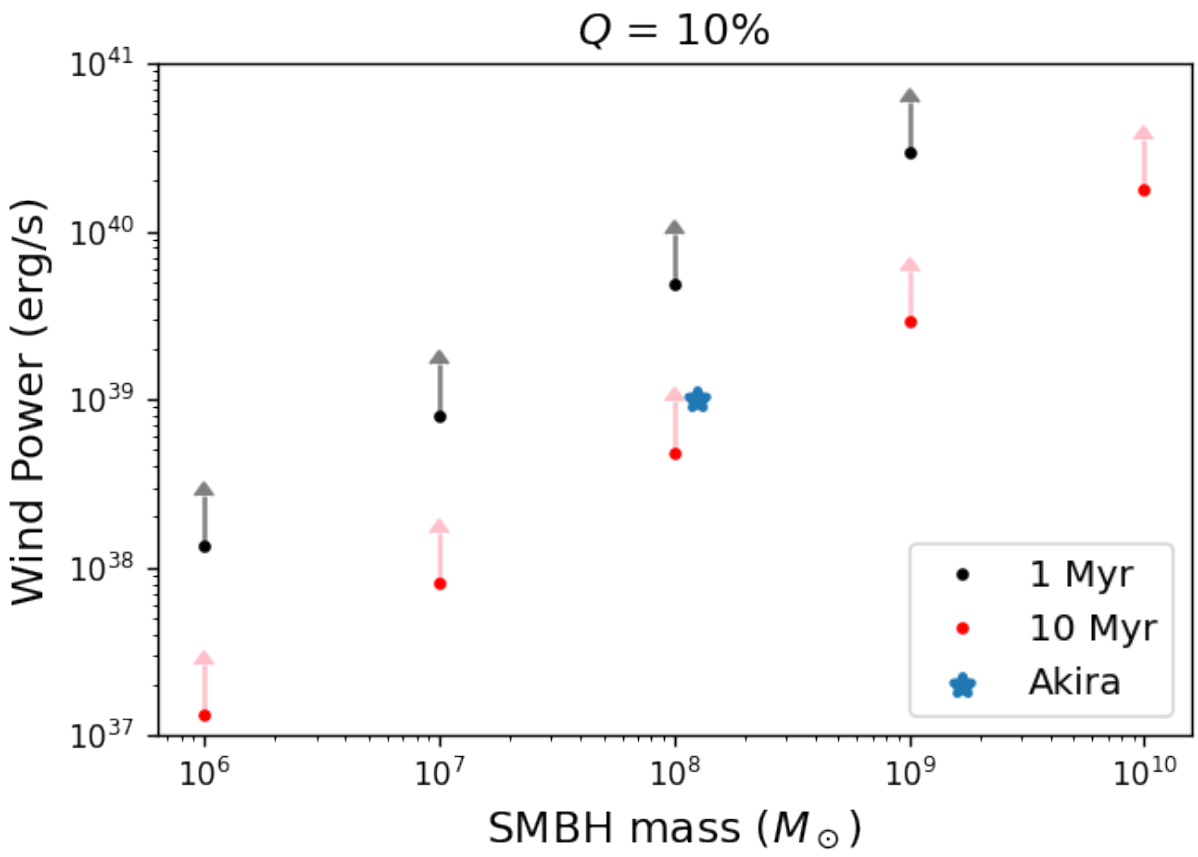

Figure 4.5: Wind power required to produce quenching of star formation of at least ten per cent. Color scheme is the same of Figure 4.4. The star indicates the values measured for the Akira LLAGN.

Overall, the LLAGN will only have an impact larger than ten per cent on the host galaxy if it persists for durations longer than 10 Myr, regardless of the SMBH mass. This timescale is one order of magnitude larger than the typical quasar lifetime. Long LLAGN durations are needed in order to significantly suppress star formation.

4.4 Discussion

Going back to the questions posed at the beginning of this work: Are LLAGN powerful enough to quench star-formation in an early-type galaxy? Can LLAGN winds keep a red-and-dead galaxy quiescent? With our simple models we find that the answer to both questions is yes. The quenching intensity, however, depends on the black hole mass, accretion rate and on the duration of the accretion episode.

Let's consider the particular case of the

Akira galaxy. Cheung et al. (2016) reported evidence for winds emerging from the LLAGN in Akira. The authors dubbed this putative class of objects "red geysers" (e.g. Roy et al. 2018). Our work supports the notion that LLAGN winds can indeed be energetic enough to originate the red geyser phenomenon. Cheung et al. (2016) find that Akira hosts a $10^8 M_\odot$ SMBH currently accreting with $\lambda \equiv L/L_{\rm Edd} = 4 \times 10^{-4}$ and that the wind lasts at least 10Myr. This value of λ corresponds to $\dot{M} = 3 \times 10^{-3} \dot{M}_{\rm Edd}$, for a typical RIAF radiative efficiency of 1% (Xie and Yuan, 2012). Our model predicts that LLAGN winds in Akira can reach quenching fractions of about 30% if those accretion rates are sustained over 10 Myr, and potentially much more for longer times. Star formation in the so-called red geyser galaxies can be significantly impacted by winds produced from underfed SMBHs.

We explored two different assumptions on the radial expansion of the wind. Both of them indicate that the kinetic and thermal energies can be carried over kiloparsec scales way beyond the SMBH gravitational sphere of influence.

An important parameter in our results is the activity time of the LLAGN. If we want to explain the quiescence of the local universe galaxies as the effect of a steady and weak wind from a very faint AGN, this object must be active for a very long time. In figure 4.3, we can see in the left panel that only

SMBHs with mass $M_{\rm SMBH} \gtrsim 10^9 M_\odot$ and $\dot{m} \gtrsim 5 \times 10^{-3}$ can noticeably impact the star-formation in $\Delta t_{\rm AGN} = 1$Myr. However, for a longer time as $\Delta t_{\rm AGN} = 10$Myr, one LLAGN with $\dot{m} \gtrsim 10^{-3}$ and masses $M_{\rm SMBH} \gtrsim 10^8 M_\odot$ can turn off more than 50% the stellar formation sites. The star formation can be severely suppressed if the galaxy inflow can sustain the LLAGN accretion rate for a long enough time.

One limitation of our model is that we are unable to give more details on specific types of stellar populations arising after quenching by the LLAGN winds. Modeling the vast dynamical range and the nonlinear physics involved in star formation is complex problem and outside the scope of this work – a simulation of effect feedback for an elliptical galaxy treated in much more detail can be seen in Yuan et al. (2018). One broad brush consequence of the suppression of star formation is that we expect a smaller number of younger stars, so LLAGN winds tend to redden the host galaxy. This effect also could have impact over the metal abundancies in the hos galaxy, but we would need a more detailed analysis to investigate this possibility.

Our model assumes a smooth wind that interacts with molecular clouds, heating them up over Myr timescales. In a more realistic setting, outflows likely strip gas clouds. The ensuing cloud mass decrease would further boosting the quenching fraction to higher values than we reported in figure 4.3. This possibility remains to be investigated in the future.

4.5 Summary

The main conclusions of of our investigation can be summarised as follows:

(i) Low-luminosity active galactic nuclei can have important feedback effects in their host galaxies by quenching star formation. This occurs via thermal winds emerging from the hot accretion flow which are able to heat up protostellar clouds and prevent them from gravitationally collapsing.

(ii) The relevance of star formation quenching by LLAGN feedback is a function of the SMBH mass, mass accretion rate and the duration of the accretion

episodes. In general, quenching is only relevant for accretion lasting longer than 1 Myr.

(iii) For an accretion episode lasting 1 Myr, a $10^8 M_\odot$ or $10^9 M_\odot$ SMBH needs $\dot{M} \gtrsim 10^{-3} \dot{M}_{\rm Edd}$ to abort more than 10% of star formation.

(iv) For an accretion episode lasting 10 Myr, a $10^8 M_\odot$ or $10^9 M_\odot$ SMBH needs $\dot{M} \gtrsim 10^{-4} \dot{M}_{\rm Edd}$ to significantly impact its host galaxy via winds.

(v) Thermal winds can reach kiloparsec scales, and beyond.

Our model is subject to the limitations of our assumptions, mainly: the assumption of a spherical isothermal galaxy, steady state, lack of details on the treatment of the interstellar medium and the wind physics. Despite these idealizations, we hope that our calculations can offer insights on the galaxy-SMBH coevolution.

In conclusion, our model demonstrates that feedback via winds from LLAGNs is an important suppressor of star formation in red sequence galaxies. LLAGNs, despite their low Eddington ratios, will keep a red-and-dead galaxy quiescent at late times. Thermally-driven winds from underfed SMBHs offer a third mode of AGN feedback, in addition to the quasar or radiative mode relevant at the peak of galaxy mergers, and the radio or jet mode relevant for radio galaxies in galaxy clusters.

Chapter 5

Summary

We presented result for three independent and interrelated research projects with the common thread of LLAGN physics. The three works contemplated different aspects of this field:

- Small-scale BH-accretion physics;
- Feedback effects on the host galaxy due to SMBH winds
- Observational data modelling with ML.

Together these topics gives a broad comprehension of LLAGN physics and large-scale impact on the host galaxy.

Chapter 2 presents simulations of hot accretion flows around a Kerr SMBH. In these simulations, we explored the wind production. These winds carry mass up to $\sim 20\%$ of the accreted mass and $1 - 10\%$ of the energy. The winds have power close to $\sim 10^{40}$erg/s for BHs with $10^8 M_\odot$ (see equation (2.29)). These results are consistent with the observations of our prototypical galaxy "Akira" (Cheung et al., 2016).

In chapter 3, we presented the work from Almeida et al. (2022), published in the Monthly Notices of the Royal Astronomical Society in its totality. Here, we developed a neural network able to calculate the SED from a RIAF in much less time than a traditional approach. Thanks to this dramatic speed up in the calculations allowed by ML, we are now able to perform Bayesian inference of electromagnetic observations of LLAGN that were previously impossible.

Chapter 4 is the work from Almeida et al. (2023), submitted on the Monthly Notices of the Royal Astronomical Society. In this work, we created a toy model for the interaction between LLAGN winds with the galaxy. Our calculations showed that LLAGN wind can be powerful enough to quench star formation and keep galaxies quiescent.

Altogether these results state the importance of SMBHs in the local universe and their impact on the host galaxy. Many questions remain open, but we expect we can add a small piece of knowledge to this colossal scientific puzzle.

Bibliography

Abdo A., Ackermann M., Ajello M., Atwood W., Axelsson M., Baldini L., Ballet J., Barbiellini G., Bastieri D., Bechtol K., et al., Fermi Large Area Telescope gamma-ray detection of the radio galaxy M87, The Astrophysical Journal, 2009, vol. 707, p. 55

Abramowicz M. A., Czerny B., Lasota J. P., Szuszkiewicz E., Slim accretion disks, ApJ, 1988, vol. 332, p. 646

Abramowicz M. A., Fragile P. C., Foundations of Black Hole Accretion Disk Theory, Living Reviews in Relativity, 2013, vol. 16, p. 1

Abuter R., Amorim A., Bauböck M., Berger J., Bonnet H., Brandner W., Clénet Y., Du Foresto V. C., de Zeeuw P., Deen C., et al., Detection of orbital motions near the last stable circular orbit of the massive black hole SgrA, Astronomy & Astrophysics, 2018, vol. 618, p. L10

Agudo I., Thum C., Gómez J., Wiesemeyer H., A simultaneous 3.5 and 1.3 mm polarimetric survey of active galactic nuclei in the northern sky, A&A, 2014, vol. 566, p. A59

Akiyama K., Alberdi A., Alef W., Algaba J. C., Anantua R., Asada K., Azulay R., Bach U., Baczko A.-K., Ball D., et al., First Sagittarius A* Event Horizon Telescope results. I. The shadow of the supermassive black hole in the center of the Milky Way, The Astrophysical Journal Letters, 2022a, vol. 930, p. L12

Akiyama K., Alberdi A., Alef W., Algaba J. C., Anantua R., Asada K., Azulay R., Bach U., Baczko A.-K., Ball D., et al., First Sagittarius A* Event Horizon

Telescope Results. V. Testing Astrophysical Models of the Galactic Center Black Hole, The Astrophysical Journal Letters, 2022b, vol. 930, p. L16

Akiyama K., Alberdi A., Alef W., Asada K., Azulay R., Baczko A.-K., Ball D., Baloković M., Barrett J., Bintley D., et al., First M87 event horizon telescope results. IV. Imaging the central supermassive black hole, The Astrophysical Journal Letters, 2019a, vol. 875, p. L4

Akiyama K., Alberdi A., Alef W., Asada K., Azulay R., Baczko A.-K., Ball D., Baloković M., Barrett J., Bintley D., et al., First M87 event horizon telescope results. VI. The shadow and mass of the central black hole, The Astrophysical Journal Letters, 2019b, vol. 875, p. L6

Almeida I., Duarte R., Nemmen R., Deep learning Bayesian inference for low-luminosity active galactic nuclei spectra, MNRAS, 2022, vol. 509, p. 5657

Almeida I., Nemmen R., Winds and feedback from supermassive black holes accreting at low rates: Hydrodynamical treatment, Monthly Notices of the Royal Astronomical Society, 2020, vol. 492, p. 2553

Almeida I., Nemmen R., Riffel R., Quenching star formation with low-luminosity AGN winds, arXiv preprint arXiv:2303.00826, 2023

Almeida I., Nemmen R., Wong K.-W., Wu Q., Irwin J. A., The multiwavelength spectrum of NGC 3115: hot accretion flow properties, MNRAS, 2018, vol. 475, p. 5398

Asensio Ramos A., Ramos Almeida C., BayesCLUMPY: BAYESIAN INFERENCE WITH CLUMPY DUSTY TORUS MODELS, ApJ, 2009

Asmus D., Hönig S., Gandhi P., Smette A., Duschl W., The subarcsecond mid-infrared view of local active galactic nuclei–I. The N-and Q-band imaging atlas, MNRAS, 2014, vol. 439, p. 1648

Baganoff F. K., Maeda Y., Morris M., Bautz M. W., Brandt W. N., Cui W., Doty J. P., Feigelson E. D., Garmire G. P., Pravdo S. H., Ricker G. R.,

Townsley L. K., Chandra X-Ray Spectroscopic Imaging of Sagittarius A* and the Central Parsec of the Galaxy, ApJ, 2003, vol. 591, p. 891

Balbus S. A., Enhanced Angular Momentum Transport in Accretion Disks, ARA&A, 2003, vol. 41, p. 555

Bandyopadhyay B., Xie F.-G., Nagar N. M., Schleicher D. R., Ramakrishnan V., Arévalo P., López E., Diaz Y., Resolving accretion flows in nearby active galactic nuclei with the Event Horizon Telescope, Monthly Notices of the Royal Astronomical Society, 2019, vol. 490, p. 4606

Beckmann V., Shrader C. R., Active Galactic Nuclei. Wiley, 2012

Begelman M. C., Radiatively inefficient accretion: breezes, winds and hyperaccretion, MNRAS, 2012, vol. 420, p. 2912

Bell E. F., Wolf C., Meisenheimer K., Rix H.-W., Borch A., Dye S., Kleinheinrich M., Wisotzki L., McIntosh D. H., Nearly 5000 Distant Early-Type Galaxies in COMBO-17: A Red Sequence and Its Evolution since$z \sim 1$, ApJ, 2004, vol. 608, p. 752

Benson A. J., Bower R. G., Frenk C. S., Lacey C. G., Baugh C. M., Cole S., What Shapes the Luminosity Function of Galaxies?, ApJ, 2003, vol. 599, p. 38

Bergstra J., Bengio Y., Random Search for Hyper-Parameter Optimization, J. Mach. Learn. Res., 2012, vol. 13, p. 281

Bietenholz M. F., Bartel N., Rupen M. P., A Stationary Core with a One-sided Jet in the Center of M81, ApJ, 2000, vol. 532, p. 895

Binette L., Magris C. G., Stasińska G., Bruzual A. G., Photoionization in elliptical galaxies by old stars., A&A, 1994, vol. 292, p. 13

Blaes O., General Overview of Black Hole Accretion Theory, Space Sci. Rev., 2014, vol. 183, p. 21

Blandford R., Globus N., Ergomagnetosphere, ejection disc, magnetopause in M87–I. Global flow of mass, angular momentum, energy, and current, Monthly Notices of the Royal Astronomical Society, 2022, vol. 514, p. 5141

Blandford R. D., Begelman M. C., On the fate of gas accreting at a low rate on to a black hole, MNRAS, 1999, vol. 303, p. L1

Blandford R. D., Znajek R. L., Electromagnetic extraction of energy from Kerr black holes, MNRAS, 1977, vol. 179, p. 433

Boizelle B. D., Walsh J. L., Barth A. J., Buote D. A., Baker A. J., Darling J., Ho L. C., Cohn J., Kabasares K. M., Black Hole Mass Measurements of Radio Galaxies NGC 315 and NGC 4261 Using ALMA CO Observations, The Astrophysical Journal, 2021, vol. 908, p. 19

Bower R. G., Schaye J., Frenk C. S., Theuns T., Schaller M., Crain R. A., McAlpine S., The dark nemesis of galaxy formation: why hot haloes trigger black hole growth and bring star formation to an end, MNRAS, 2017, vol. 465, p. 32

Bu D.-F., Gan Z.-M., On the wind production from hot accretion flows with different accretion rates, MNRAS, 2018, vol. 474, p. 1206

Bu D.-F., Yang X.-H., Thermal wind from hot accretion flows at large radii, MNRAS, 2018, vol. 476, p. 4395

Bu D.-F., Yuan F., Gan Z.-M., Yang X.-H., Magnetohydrodynamic Numerical Simulation of Wind Production from Hot Accretion Flows around Black Holes at Very Large Radii, ApJ, 2016, vol. 823, p. 90

Bundy K., Ellis R. S., Conselice C. J., Taylor J. E., Cooper M. C., Willmer C. N. A., Weiner B. J., Coil A. L., Noeske K. G., Eisenhardt P. R. M., The Mass Assembly History of Field Galaxies: Detection of an Evolving Mass Limit for Star-Forming Galaxies, ApJ, 2006, vol. 651, p. 120

Capetti A., Kleijn G. V., Chiaberge M., The HST view of the nuclear emission line region in low luminosity radio-galaxies, A&A, 2005, vol. 439, p. 935

Cheung E., Bundy K., Cappellari M., Peirani S., Rujopakarn W., Westfall K., Yan R., Bershady M., Greene J. E., Heckman T. M., Drory N., Law D. R., Masters K. L., Thomas D., Wake D. A., Weijmans A.-M., Rubin K., Belfiore F., Vulcani B., Chen Y.-M., Zhang K., Gelfand J. D., Bizyaev D., Roman-Lopes A., Schneider D. P., Suppressing star formation in quiescent galaxies with supermassive black hole winds, Nature, 2016, vol. 533, p. 504

Ciotti L., Ostriker J. P., Proga D., Feedback from Central Black Holes in Elliptical Galaxies. III. Models with Both Radiative and Mechanical Feedback, ApJ, 2010, vol. 717, p. 708

Croton D. J., Springel V., White S. D. M., De Lucia G., Frenk C. S., Gao L., Jenkins A., Kauffmann G., Navarro J. F., Yoshida N., The many lives of active galactic nuclei: cooling flows, black holes and the luminosities and colours of galaxies, MNRAS, 2006, vol. 365, p. 11

Cybenko G., Approximation by superpositions of a sigmoidal function, Mathematics of Control, Signals and Systems, 1989, vol. 2, p. 303

de Menezes R., Nemmen R., Finke J. D., Almeida I., Rani B., Gamma-ray observations of low-luminosity active galactic nuclei, Monthly Notices of the Royal Astronomical Society, 2020, vol. 492, p. 4120

De Villiers J.-P., Hawley J. F., Krolik J. H., Magnetically Driven Accretion Flows in the Kerr Metric. I. Models and Overall Structure, ApJ, 2003, vol. 599, p. 1238

Dib S., Brandenburg A., Kim J., Gopinathan M., André P., Core mass function: The role of gravity, The Astrophysical Journal, 2008, vol. 678, p. L105

Doeleman S. S., Fish V. L., Schenck D. E., Beaudoin C., Blundell R., Bower G. C., Broderick A. E., Chamberlin R., Freund R., Friberg P., Gurwell M. A., Ho P. T. P., Honma M., Inoue M., Krichbaum T. P., Lamb J., Loeb A., Lonsdale C., Marrone D. P., Moran J. M., Oyama T., Plambeck R., Primiani R. A., Rogers A. E. E., Smythe D. L., SooHoo J., Strittmatter P., Tilanus

R. P. J., Titus M., Weintroub J., Wright M., Young K. H., Ziurys L. M., Jet-Launching Structure Resolved Near the Supermassive Black Hole in M87, Science, 2012, vol. 338, p. 355

Doeleman S. S., Weintroub J., Rogers A. E. E., Plambeck R., Freund R., Tilanus R. P. J., Friberg P., Ziurys L. M., Moran J. M., Corey B., Young K. H., Smythe D. L., Titus M., Marrone D. P., Cappallo R. J., Bock D. C.-J., Bower G. C., Chamberlin R., Davis G. R., Krichbaum T. P., Lamb J., Maness H., Niell A. E., Roy A., Strittmatter P., Werthimer D., Whitney A. R., Woody D., Event-horizon-scale structure in the supermassive black hole candidate at the Galactic Centre, Nature, 2008, vol. 455, p. 78

Done C., Gierliński M., Kubota A., Modelling the behaviour of accretion flows in X-ray binaries. Everything you always wanted to know about accretion but were afraid to ask, A&A Rev., 2007, vol. 15, p. 1

Dubois Y., Pichon C., Haehnelt M., Kimm T., Slyz A., Devriendt J., Pogosyan D., Feeding compact bulges and supermassive black holes with low angular momentum cosmic gas at high redshift, MNRAS, 2012, vol. 423, p. 3616

Enßlin T. A., Brüggen M., On the formation of cluster radio relics, MNRAS, 2002, vol. 331, p. 1011

Eracleous M., Hwang J. A., Flohic H. M. L. G., Spectral Energy Distributions of Weak Active Galactic Nuclei Associated with Low-Ionization Nuclear Emission Regions, ApJS, 2010, vol. 187, p. 135

Esin A. A., McClintock J. E., Narayan R., Advection-Dominated Accretion and the Spectral States of Black Hole X-Ray Binaries: Application to Nova Muscae 1991, ApJ, 1997, vol. 489, p. 865

Fabian A. C., Observational Evidence of Active Galactic Nuclei Feedback, ARA&A, 2012, vol. 50, p. 455

Fabian A. C., Reynolds C., Taylor G., Dunn R., On viscosity, conduction and sound waves in the intracluster medium, Monthly Notices of the Royal Astronomical Society, 2005, vol. 363, p. 891

Falcke H., Melia F., Agol E., Viewing the Shadow of the Black Hole at the Galactic Center, ApJ, 2000, vol. 528, p. L13

Fathivavsari H., , 2020 Deep Learning Prediction of Quasars Broad Ly$\hat{I}\pm$ Emission Line

Ferrarese L., Ford H., Supermassive Black Holes in Galactic Nuclei: Past, Present and Future Research, Space Sci. Rev., 2005, vol. 116, p. 523

Ferrarese L., Ford H. C., Jaffe W., Evidence for a massive black hole in the active galaxy NGC 4261 from Hubble Space Telescope images and spectra, ApJ, 1996, vol. 470, p. 444

Finke J. D., Dermer C. D., Böttcher M., Synchrotron Self-Compton Analysis of TeV X-Ray-Selected BL Lacertae Objects, ApJ, 2008, vol. 686, p. 181

Fishbone L. G., Moncrief V., Relativistic fluid disks in orbit around Kerr black holes, The Astrophysical Journal, 1976, vol. 207, p. 962

Foreman-Mackey D., Hogg D. W., Lang D., Goodman J., emcee: The MCMC Hammer, PASP, 2013, vol. 125, p. 306

Frank J., King A., Raine D. J., Accretion Power in Astrophysics 3rd edn. Cambridge University Press, 2002

Gammie C. F., McKinney J. C., Tóth G., HARM: A Numerical Scheme for General Relativistic Magnetohydrodynamics, ApJ, 2003, vol. 589, p. 444

Gebhardt K., Adams J., Richstone D., Lauer T. R., Faber S. M., Gültekin K., Murphy J., Tremaine S., The Black Hole Mass in M87 from Gemini/NIFS Adaptive Optics Observations, ApJ, 2011, vol. 729, p. 119

Gebhardt K., Bender R., Bower G., Dressler A., Faber S. M., Filippenko A. V., Green R., Grillmair C., Ho L. C., Kormendy J., Lauer T. R., Magorrian J., Pinkney J., Richstone D., Tremaine S., A Relationship between Nuclear Black Hole Mass and Galaxy Velocity Dispersion, ApJ, 2000, vol. 539, p. L13

Genel S., Vogelsberger M., Nelson D., Sijacki D., Springel V., Hernquist L., Following the flow: tracer particles in astrophysical fluid simulations, MNRAS, 2013, vol. 435, p. 1426

Genzel R., Cesarsky C. J., Extragalactic Results from the Infrared Space Observatory, ARA&A, 2000, vol. 38, p. 761

Genzel R., Eisenhauer F., Gillessen S., The Galactic Center massive black hole and nuclear star cluster, Reviews of Modern Physics, 2010, vol. 82, p. 3121

Genzel R., Schödel R., Ott T., Eckart A., Alexander T., Lacombe F., Rouan D., Aschenbach B., Near-infrared flares from accreting gas around the supermassive black hole at the Galactic Centre, Nature, 2003, vol. 425, p. 934

George D., Huerta E., Deep Learning for real-time gravitational wave detection and parameter estimation: Results with Advanced LIGO data, Physics Letters B, 2018, vol. 778, p. 64

Ghez A. M., Salim S., Hornstein S. D., Tanner A., Lu J. R., Morris M., Becklin E. E., Duchêne G., Stellar Orbits around the Galactic Center Black Hole, ApJ, 2005, vol. 620, p. 744

Gillessen S., Eisenhauer F., Trippe S., Alexander T., Genzel R., Martins F., Ott T., Monitoring Stellar Orbits Around the Massive Black Hole in the Galactic Center, ApJ, 2009, vol. 692, p. 1075

Giovannini G., Feretti L., Comoretto G., VLBI observations of a complete sample of radio galaxies. I-Snapshot data, The Astrophysical Journal, 1990, vol. 358, p. 159

Godunov S. K., Bohachevsky I., Finite difference method for numerical computation of discontinuous solutions of the equations of fluid dynamics, Matematičeskij sbornik, 1959, vol. 47, p. 271

Gonzalez-Martin O., Masegosa J., Márquez I., Guerrero M. A., Dultzin-Hacyan D., X-ray nature of the LINER nuclear sources, A&A, 2006, vol. 460, p. 45

Goodman J., Weare J., Ensemble samplers with affine invariance, Communications in applied mathematics and computational science, 2010, vol. 5, p. 65

Greene J. E., Zakamska N. L., Smith P. S., A spectacular outflow in an obscured quasar, The Astrophysical Journal, 2012, vol. 746, p. 86

Gu Q.-S., Huang J.-S., Wilson G., Fazio G., Direct Evidence from Spitzer for a low-luminosity AGN at the center of the Elliptical Galaxy NGC 315, ApJ, 2007, vol. 671, p. L105

Guo F., Mathews W. G., The Fermi Bubbles. I. Possible Evidence for Recent AGN Jet Activity in the Galaxy, ApJ, 2012, vol. 756, p. 181

Harlow F. H., Welch J. E., Numerical Calculation of Time-Dependent Viscous Incompressible Flow of Fluid with Free Surface, Physics of Fluids, 1965, vol. 8, p. 2182

Harten A., Lax P. D., Leer B. v., On upstream differencing and Godunov-type schemes for hyperbolic conservation laws, SIAM review, 1983, vol. 25, p. 35

HESS Collaboration Abramowski A., Aharonian F., Benkhali F. A., Akhperjanian A. G., Angüner E. O., Backes M., Balzer A., Becherini Y., Tjus J. B., et al. Acceleration of petaelectronvolt protons in the Galactic Centre, Nature, 2016, vol. 531, p. 476

Ho L. C., Nuclear Activity in Nearby Galaxies, ARA&A, 2008, vol. 46, p. 475

Ho L. C., Filippenko A. V., Sargent W. L., New Insights into the Physical Nature of LINERs from a Multiwavelength Analysis of the Nucleus of M81, The Astrophysical Journal, 1996, vol. 462, p. 183

Igumenshchev I. V., Abramowicz M. A., Rotating accretion flows around black holes: convection and variability, MNRAS, 1999, vol. 303, p. 309

Igumenshchev I. V., Abramowicz M. A., Two-dimensional Models of Hydrodynamical Accretion Flows into Black Holes, ApJS, 2000, vol. 130, p. 463

Ilha G. S., Riffel R. A., Ricci T. V., Rembold S. B., Storchi-Bergmann T., Riffel R., Roy N., Bundy K., Nemmen R., Schimoia J. S., et al., Active galactic nuclei signatures in Red Geyser galaxies from Gemini GMOS-IFU observations, Monthly Notices of the Royal Astronomical Society, 2022, vol. 516, p. 1442

Jones D. L., Wehrle A. E., VLBA Imaging of NGC 4261: Symmetric Parsec-scale Jets and the Inner Accretion Region, ApJ, 1997, vol. 484, p. 186

Junor W., Biretta J. A., The radio jet in 3C274 at 0.01 PC resolution, The Astronomical Journal, 1995, vol. 109, p. 500

Kellermann K. I., Sramek R., Schmidt M., Shaffer D. B., Green R., VLA observations of objects in the Palomar Bright Quasar Survey, AJ, 1989, vol. 98, p. 1195

Kelley H. J., Gradient theory of optimal flight paths, Ars Journal, 1960, vol. 30, p. 947

King A., Black Holes, Galaxy Formation, and the M_{BH}-σ Relation, ApJ, 2003, vol. 596, p. L27

Kingma D., Ba J., Adam: A Method for Stochastic Optimization, International Conference on Learning Representations, 2014

Komissarov S., A Godunov-type scheme for relativistic magnetohydrodynamics, Monthly Notices of the Royal Astronomical Society, 1999, vol. 303, p. 343

Kormendy J., Ho L. C., Coevolution (Or Not) of Supermassive Black Holes and Host Galaxies, ARA&A, 2013, vol. 51, p. 511

Krizhevsky A., Sutskever I., Hinton G. E., ImageNet Classification with Deep Convolutional Neural Networks, Commun. ACM, 2017, vol. 60, p. 84

Kuo C. Y., Asada K., Rao R., Nakamura M., Algaba J. C., Liu H. B., Inoue M., Koch P. M., Ho P. T. P., Matsushita S., Pu H.-Y., Akiyama K., Nishioka H., Pradel N., Measuring Mass Accretion Rate onto the Supermassive Black

Hole in M87 Using Faraday Rotation Measure with the Submillimeter Array, ApJ, 2014, vol. 783, p. L33

Lazio T. J. W., Waltman E. B., Ghigo F. D., Fiedler R. L., Foster R. S., Johnston K. J., A Dual-Frequency, Multiyear Monitoring Program of Compact Radio Sources, ApJS, 2001, vol. 136, p. 265

LeCun Y., Bengio Y., Hinton G., Deep learning, nature, 2015, vol. 521, p. 436

Lee S.-S., Lobanov A. P., Krichbaum T. P., Witzel A., Zensus A., Bremer M., Greve A., Grewing M., A global 86 GHz VLBI survey of compact radio sources, The Astronomical Journal, 2008, vol. 136, p. 159

Leshno M., Lin V. Y., Pinkus A., Schocken S., Multilayer feedforward networks with a nonpolynomial activation function can approximate any function, Neural networks, 1993

Li J., Ostriker J., Sunyaev R., Rotating Accretion Flows: From Infinity to the Black Hole, ApJ, 2013, vol. 767, p. 105

Liska M., Hesp C., Tchekhovskoy A., Ingram A., van der Klis M., Markoff S., Formation of precessing jets by tilted black hole discs in 3D general relativistic MHD simulations, MNRAS, 2018, vol. 474, p. L81

Liska M. T. P., Chatterjee K., Issa D., Yoon D., Kaaz N., Tchekhovskoy A., van Eijnatten D., Musoke G., Hesp C., Rohoza V., Markoff S., Ingram A., van der Klis M., H-AMR: A New GPU-accelerated GRMHD Code for Exascale Computing with 3D Adaptive Mesh Refinement and Local Adaptive Time Stepping, ApJS, 2022, vol. 263, p. 26

Lonsdale C. J., Doeleman S. S., Phillips R. B., A 3 millimeter VLBI continuum source survey, The Astronomical Journal, 1998, vol. 116, p. 8

Mahadevan R., Narayan R., Krolik J., Gamma-Ray Emission from Advection-dominated Accretion Flows around Black Holes: Application to the Galactic Center, ApJ, 1997, vol. 486, p. 268

Maiolino R., Gallerani S., Neri R., Cicone C., Ferrara A., Genzel R., Lutz D., Sturm E., Tacconi L., Walter F., et al., Evidence of strong quasar feedback in the early Universe, Monthly Notices of the Royal Astronomical Society: Letters, 2012, vol. 425, p. L66

Markoff S., Nowak M., Young A., Marshall H. L., Canizares C. R., Peck A., Krips M., Petitpas G., Schödel R., Bower G. C., Chandra P., Ray A., Muno M., Gallagher S., Hornstein S., Cheung C. C., Results from an Extensive Simultaneous Broadband Campaign on the Underluminous Active Nucleus M81*: Further Evidence for Mass-scaling Accretion in Black Holes, ApJ, 2008, vol. 681, p. 905

McConnell N. J., Ma C.-P., Gebhardt K., Wright S. A., Murphy J. D., Lauer T. R., Graham J. R., Richstone D. O., Two ten-billion-solar-mass black holes at the centres of giant elliptical galaxies, Nature, 2011, vol. 480, p. 215

McKinney J. C., Tchekhovskoy A., Blandford R. D., General relativistic magnetohydrodynamic simulations of magnetically choked accretion flows around black holes, MNRAS, 2012, vol. 423, p. 3083

McNamara B. R., Kazemzadeh F., Rafferty D. A., Bîrzan L., Nulsen P. E. J., Kirkpatrick C. C., Wise M. W., An Energetic AGN Outburst Powered by a Rapidly Spinning Supermassive Black Hole or an Accreting Ultramassive Black Hole, ApJ, 2009, vol. 698, p. 594

McNamara B. R., Nulsen P. E. J., Heating Hot Atmospheres with Active Galactic Nuclei, ARA&A, 2007, vol. 45, p. 117

McNamara B. R., Nulsen P. E. J., Mechanical feedback from active galactic nuclei in galaxies, groups and clusters, New Journal of Physics, 2012, vol. 14, p. 055023

Meier D. L., Black Hole Astrophysics: The Engine Paradigm. Springer, Verlag Berlin Heidelberg, 2012

Merloni A., Heinz S., Measuring the kinetic power of active galactic nuclei in the radio mode, MNRAS, 2007, vol. 381, p. 589

Mewes V., , 2021

Mignone A., Bodo G., Massaglia S., Matsakos T., Tesileanu O., Zanni C., Ferrari A., PLUTO: A Numerical Code for Computational Astrophysics, ApJS, 2007, vol. 170, p. 228

Mignone A., Zanni C., Tzeferacos P., van Straalen B., Colella P., Bodo G., The PLUTO Code for Adaptive Mesh Computations in Astrophysical Fluid Dynamics, ApJS, 2012, vol. 198, p. 7

Misner C. W., Thorne K. S., Wheeler J. A., Gravitation. W. H. Freeman and Company, 1973

Morabito D., Niell A., Preston R., Linfield R., Wehrle A., Faulkner J., VLBI observations of 416 extragalactic radio sources, The Astronomical Journal, 1986, vol. 91, p. 1038

Mościbrodzka M., Status of GRMHD simulations and radiative models of Sgr A*. In The Multi-Messenger Astrophysics of the Galactic Centre , vol. 322 of IAU Symposium, 2017, p. 43

Mościbrodzka M., Falcke H., Coupled jet-disk model for Sagittarius A*: explaining the flat-spectrum radio core with GRMHD simulations of jets, A&A, 2013, vol. 559, p. L3

Mościbrodzka M., Falcke H., Shiokawa H., Gammie C. F., Observational appearance of inefficient accretion flows and jets in 3D GRMHD simulations: Application to Sagittarius A*, A&A, 2014, vol. 570, p. A7

Nagar N. M., Falcke H., Wilson A. S., Radio sources in low-luminosity active galactic nuclei. IV. Radio luminosity function, importance of jet power, and radio properties of the complete Palomar sample, A&A, 2005, vol. 435, p. 521

Narayan R., Kato S., Honma F., Global Structure and Dynamics of Advection-dominated Accretion Flows around Black Holes, ApJ, 1997, vol. 476, p. 49

Narayan R., Mahadevan R., Grindlay J. E., Popham R. G., Gammie C., Advection-dominated accretion model of Sagittarius A*: evidence for a black hole at the Galactic center., ApJ, 1998, vol. 492, p. 554

Narayan R., Mahadevan R., Quataert E., Advection-dominated accretion around black holess. In Theory of Black Hole Accretion Disks , 1998, p. 148

Narayan R., Sadowski A., Penna R. F., Kulkarni A. K., GRMHD simulations of magnetized advection-dominated accretion on a non-spinning black hole: role of outflows, MNRAS, 2012, vol. 426, p. 3241

Narayan R., Yi I., Advection-dominated accretion: A self-similar solution, ApJ, 1994, vol. 428, p. L13

Narayan R., Yi I., Advection-dominated accretion: Self-similarity and bipolar outflows, ApJ, 1995, vol. 444, p. 231

Narayan R., Yi I., Mahadevan R., Explaining the spectrum of Sagittarius A* with a model of an accreting black hole, Nature, 1995, vol. 374, p. 623

Nemmen R. S., Storchi-Bergmann T., Eracleous M., Spectral models for low-luminosity active galactic nuclei in LINERs: the role of advection-dominated accretion and jets, MNRAS, 2014, vol. 438, p. 2804

Nemmen R. S., Storchi-Bergmann T., Yuan F., Eracleous M., Terashima Y., Wilson A. S., Radiatively Inefficient Accretion Flow in the Nucleus of NGC 1097, ApJ, 2006, vol. 643, p. 652

Netzer H., Revisiting the Unified Model of Active Galactic Nuclei, ARA&A, 2015, vol. 53, p. 365

Ohsuga K., Two-dimensional Radiation-Hydrodynamic Model for Limit-Cycle Oscillations of Luminous Accretion Disks, ApJ, 2006, vol. 640, p. 923

Pacheco-Sanchez J., Alejo R., Cruz-Reyes H., Álvarez-Ramírez F., Neural networks to fit potential energy curves from asphaltene-asphaltene interaction data, Fuel, 2019

Paczyńsky B., Wiita P. J., Thick accretion disks and supercritical luminosities, A&A, 1980, vol. 88, p. 23

Park J., Hada K., Kino M., Nakamura M., Ro H., Trippe S., Faraday Rotation in the Jet of M87 inside the Bondi Radius: Indication of Winds from Hot Accretion Flows Confining the Relativistic Jet, ApJ, 2019, vol. 871, p. 257

Perlman E. S., Sparks W. B., Radomski J., Packham C., Fisher R. S., Piña R., Biretta J. A., Deep 10 micron imaging of M87, The Astrophysical Journal Letters, 2001, vol. 561, p. L51

Ponti G., Terrier R., Goldwurm A., Belanger G., Trap G., Discovery of a Superluminal Fe K Echo at the Galactic Center: The Glorious Past of Sgr A* Preserved by Molecular Clouds, ApJ, 2010, vol. 714, p. 732

Porth O., Olivares H., Mizuno Y., Younsi Z., Rezzolla L., Moscibrodzka M., Falcke H., Kramer M., The black hole accretion code, Computational Astrophysics and Cosmology, 2017, vol. 4, p. 1

Prieto M. A., Fernández-Ontiveros J. A., Markoff S., Espada D., González-Martín O., The central parsecs of M87: jet emission and an elusive accretion disc, MNRAS, 2016, vol. 457, p. 3801

Proga D., Begelman M. C., Accretion of Low Angular Momentum Material onto Black Holes: Two-dimensional Magnetohydrodynamic Case, ApJ, 2003, vol. 592, p. 767

Quataert E., Particle Heating by Alfvenic Turbulence in Hot Accretion Flows, ApJ, 1998, vol. 500, p. 978

Quataert E., Narayan R., On the Energetics of Advection-dominated Accretion Flows, ApJ, 1999, vol. 516, p. 399

Rafferty D. A., McNamara B. R., Nulsen P. E. J., The Regulation of Cooling and Star Formation in Luminous Galaxies by Active Galactic Nucleus Feedback and the Cooling-Time/Entropy Threshold for the Onset of Star Formation, ApJ, 2008, vol. 687, p. 899

Rafferty D. A., McNamara B. R., Nulsen P. E. J., Wise M. W., The Feedback-regulated Growth of Black Holes and Bulges through Gas Accretion and Starbursts in Cluster Central Dominant Galaxies, ApJ, 2006, vol. 652, p. 216

Rosolowsky E., The mass spectra of giant molecular clouds in the local group, Publications of the Astronomical Society of the Pacific, 2005, vol. 117, p. 1403

Roy N., Bundy K., Cheung E., Rujopakarn W., Cappellari M., Belfiore F., Yan R., Heckman T., Bershady M., Greene J., Westfall K., Drory N., Rubin K., Law D., Zhang K., Gelfand J., Bizyaev D., Wake D., Masters K., Thomas D., Li C., Riffel R. A., Detecting Radio AGN Signatures in Red Geysers, ApJ, 2018, vol. 869, p. 117

Roy N., Bundy K., Nevin R., Belfiore F., Yan R., Campbell S., Riffel R. A., Riffel R., Bershady M., Westfall K., et al., Evidence of wind signatures in the gas velocity profiles of Red Geysers, The Astrophysical Journal, 2021, vol. 913, p. 33

Ruder S., An overview of gradient descent optimization algorithms, arXiv preprint arXiv:1609.04747, 2016

Rupke D. S., Veilleux S., Integral field spectroscopy of massive, kiloparsec-scale outflows in the infrared-luminous QSO Mrk 231, The Astrophysical Journal Letters, 2011, vol. 729, p. L27

Russell H. R., Fabian A. C., McNamara B. R., Broderick A. E., Inside the Bondi radius of M87, MNRAS, 2015, vol. 451, p. 588

Ryan B. R., Dolence J. C., Gammie C. F., bhlight: General Relativistic Radiation Magnetohydrodynamics with Monte Carlo Transport, ApJ, 2015, vol. 807, p. 31

Sánchez S., Walcher C., Lopez-Cobá C., Barrera-Ballesteros J., Mejía-Narváez A., Espinosa-Ponce C., Camps-Fariña A., From global to spatially resolved

in low-redshift galaxies, Revista mexicana de astronomía y astrofísica, 2021, vol. 57, p. 3

Sądowski A., Lasota J.-P., Abramowicz M. A., Narayan R., Energy flows in thick accretion discs and their consequences for black hole feedback, MNRAS, 2016, vol. 456, p. 3915

Sądowski A., Narayan R., Penna R., Zhu Y., Energy, momentum and mass outflows and feedback from thick accretion discs around rotating black holes, MNRAS, 2013, vol. 436, p. 3856

Schneider P., Extragalactic astronomy and cosmology: an introduction. vol. 146, Springer, 2006

Shakura N. I., Sunyaev R. A., Black holes in binary systems. Observational appearance., A&A, 1973, vol. 24, p. 337

Shapiro S. L., Lightman A. P., Black holes in X-ray binaries-Marginal existence and rotation reversals of accretion disks, The Astrophysical Journal, 1976, vol. 204, p. 555

Sharma P., Quataert E., Hammett G. W., Stone J. M., Electron Heating in Hot Accretion Flows, ApJ, 2007, vol. 667, p. 714

Shi F., Li Z., Yuan F., Zhu B., An energetic hot wind from the low-luminosity active galactic nucleus M81, Nature Astronomy, 2021, vol. 5, p. 928

Sijacki D., Springel V., Di Matteo T., Hernquist L., A unified model for AGN feedback in cosmological simulations of structure formation, MNRAS, 2007, vol. 380, p. 877

Sijacki D., Vogelsberger M., Genel S., Springel V., Torrey P., Snyder G. F., Nelson D., Hernquist L., The Illustris simulation: the evolving population of black holes across cosmic time, MNRAS, 2015, vol. 452, p. 575

Silk J., Rees M. J., Quasars and galaxy formation, arXiv preprint astro-ph/9801013, 1998

Soares G. R. R., Accretion discs, jets, and black hole spins: a study of blazars, Universidade de São Paulo, 2021, Ph.D. Thesis

Stone J. M., Pringle J. E., Begelman M. C., Hydrodynamical non-radiative accretion flows in two dimensions, MNRAS, 1999, vol. 310, p. 1002

Sturm E., Dexter J., Pfuhl O., Stock M. R., Davies R. I., Lutz D., Clénet Y., Eckart A., Eisenhauer F., Genzel R., Gratadour D., Hönig S. F., Kishimoto M., Lacour S., Millour F., Netzer H., Perrin G., Peterson B. M., Petrucci P. O., Rouan D., Waisberg I., Woillez J., Amorim A., Brandner W., Schreiber N. M. F., Garcia P. J. V., Gillessen S., Ott T., Paumard T., Perraut K., Scheithauer S., Straubmeier C., Tacconi L. J., Widmann F., Collaboration G. R. A. V. I. T. Y., Spatially resolved rotation of the broad-line region of a quasar at sub-parsec scale, Nature, 2018, vol. 563, p. 657

Su M., Slatyer T. R., Finkbeiner D. P., Giant Gamma-ray Bubbles from Fermi-LAT: Active Galactic Nucleus Activity or Bipolar Galactic Wind?, ApJ, 2010, vol. 724, p. 1044

Takami H., γ-rays as a diagnostic of the origin of core radiation in low-luminosity active galactic nuclei, MNRAS, 2011, vol. 413, p. 1845

Tchekhovskoy A., Launching of Active Galactic Nuclei Jets. In Astrophysics and Space Science Library , vol. 414 of Astrophysics and Space Science Library, 2015, p. 45

Tchekhovskoy A., McKinney J. C., Narayan R., General Relativistic Modeling of Magnetized Jets from Accreting Black Holes, Journal of Physics Conference Series, 2012, vol. 372, p. 012040

Tchekhovskoy A., Metzger B. D., Giannios D., Kelley L. Z., Swift J1644+57 gone MAD: the case for dynamically important magnetic flux threading the black hole in a jetted tidal disruption event, MNRAS, 2014, vol. 437, p. 2744

Tchekhovskoy A., Narayan R., McKinney J. C., Black Hole Spin and The Radio Loud/Quiet Dichotomy of Active Galactic Nuclei, ApJ, 2010, vol. 711, p. 50

Thuerey N., Holl P., Mueller M., Schnell P., Trost F., Um K., Physics-based Deep Learning, arXiv e-prints, 2021, p. arXiv:2109.05237

Toro E., Riemann Solvers and Numerical Methods for Fluid Dynamics: A Practical Introduction. Springer Berlin Heidelberg, 2009

Vanzo D., Siviglia A., , 2018 A. Siviglia November 15, 2018 - ETH Z

Vemado A., Radiative cooling and state transitions in stellar mass black holes, Universidade de Sao Paulo, 2020, Master Dissertation

Verdoes Kleijn G. A., Baum S. A., de Zeeuw P. T., O'Dea C. P., Core radio and optical emission in the nuclei of nearby FR I radio galaxies, AJ, 2002, vol. 123, p. 1334

Visser M., The Kerr spacetime: A brief introduction, arXiv preprint arXiv:0706.0622, 2007

Wang Q. D., Nowak M. A., Markoff S. B., Baganoff F. K., Nayakshin S., Yuan F., Cuadra J., Davis J., Dexter J., Fabian A. C., Grosso N., Haggard D., Houck J., Ji L., Li Z., Neilsen J., Porquet D., Ripple F., Shcherbakov R. V., Dissecting X-ray–Emitting Gas Around the Center of Our Galaxy, Science, 2013, vol. 341, p. 981

Whysong D., Antonucci R., Thermal emission as a test for hidden nuclei in nearby radio galaxies, The Astrophysical Journal, 2004, vol. 602, p. 116

Wong K.-W., Irwin J. A., Shcherbakov R. V., Yukita M., Million E. T., Bregman J. N., The Megasecond Chandra X-Ray Visionary Project Observation of NGC3115: Witnessing the Flow of Hot Gas within the Bondi Radius, ApJ, 2014, vol. 780, p. 9

Wong K.-W., Irwin J. A., Yukita M., Million E. T., Mathews W. G., Bregman J. N., Resolving the Bondi Accretion Flow toward the Supermassive Black Hole of NGC 3115 with Chandra, ApJ, 2011, vol. 736, p. L23

Woo J.-H., Cho H., Gallo E., Hodges-Kluck E., Le H. A. N., Shin J., Son D., Horst J. C., A 10,000-solar-mass black hole in the nucleus of a bulgeless dwarf galaxy, Nature Astronomy, 2019, vol. 3, p. 755

Wu Q., Yuan F., Cao X., On the Origin of X-Ray Emission in Some FR I Galaxies: ADAF or Jet?, ApJ, 2007, vol. 669, p. 96

Xie F.-G., Yuan F., Radiative efficiency of hot accretion flows, MNRAS, 2012, vol. 427, p. 1580

Yang H., Yuan F., Yuan Y.-F., White C. J., Numerical Simulation of Hot Accretion Flows. IV. Effects of Black Hole Spin and Magnetic Field Strength on the Wind and the Comparison between Wind and Jet Properties, ApJ, 2021, vol. 914, p. 131

Young A., McHardy I., Emmanoulopoulos D., Connolly S., The absence of a thin disc in M81, Monthly Notices of the Royal Astronomical Society, 2018, vol. 476, p. 5698

Yu Z., Yuan F., Ho L. C., On the Origin of Ultraviolet Emission and the Accretion Model of Low-luminosity Active Galactic Nuclei, ApJ, 2011, vol. 726, p. 87

Yuan F., Bu D., Wu M., Numerical Simulation of Hot Accretion Flows. II. Nature, Origin, and Properties of Outflows and their Possible Observational Applications, ApJ, 2012, vol. 761, p. 130

Yuan F., Gan Z., Narayan R., Sadowski A., Bu D., Bai X.-N., Numerical Simulation of Hot Accretion Flows. III. Revisiting Wind Properties Using the Trajectory Approach, ApJ, 2015, vol. 804, p. 101

Yuan F., Narayan R., Hot Accretion Flows Around Black Holes, ARA&A, 2014, vol. 52, p. 529

Yuan F., Quataert E., Narayan R., Nonthermal Electrons in Radiatively Inefficient Accretion Flow Models of Sagittarius A*, ApJ, 2003, vol. 598, p. 301

Yuan F., Wu M., Bu D., Numerical Simulation of Hot Accretion Flows. I. A Large Radial Dynamical Range and the Density Profile of Accretion Flow, ApJ, 2012, vol. 761, p. 129

Yuan F., Yoon D., Li Y.-P., Gan Z.-M., Ho L. C., Guo F., Active galactic nucleus feedback in an elliptical galaxy with the most updated AGN physics. I. low angular momentum case, The Astrophysical Journal, 2018, vol. 857, p. 121

Yuan F., Yu Z., Ho L. C., Revisiting the "Fundamental Plane" of Black Hole Activity at Extremely Low Luminosities, ApJ, 2009, vol. 703, p. 1034

Zezas A., Birkinshaw M., Worrall D., Peters A., Fabbiano G., Chandra observations of NGC 4261 (3C 270): revealing the jet and hidden active galactic nucleus in a Type 2 LINER, ApJ, 2005, vol. 627, p. 711

Zhou D.-X., Universality of deep convolutional neural networks, Applied and Computational Harmonic Analysis, 2020, vol. 48, p. 787

Appendix

Appendix A

AGNNES Appendix

A.1 Observational data

The observational data of the modelled galaxies are listed in Tables A.1-A.2. Data for M87 were extracted from Prieto et al. (2016) and data for NGC315 and NGC4261 were the same as presented by de Menezes et al. (2020).

ν (Hz)	νL_ν (erg s^{-1})	Reference
1.60E+09	1.87E+038	Giovannini et al. (1990)
8.40E+09	1.41E+039	Morabito et al. (1986)
2.20E+10	2.48E+039	Junor and Biretta (1995)
8.60E+10	4.43E+039	Lee et al. (2008)
1.00E+11	1.61E+040	Lonsdale et al. (1998)
2.30E+11	7.25E+040	Doeleman et al. (2012)
2.60E+13	1.09E+041	Whysong and Antonucci (2004)
2.80E+13	1.51E+041	Perlman et al. (2001)
2.47E+14	1.28E+041	Prieto et al. (2016)
3.32E+14	1.39E+041	Prieto et al. (2016)
3.70E+14	7.55E+040	Prieto et al. (2016)
4.99E+14	6.81E+040	Prieto et al. (2016)
6.32E+14	8.40E+040	Prieto et al. (2016)
8.93E+14	5.15E+040	Prieto et al. (2016)
1.10E+15	4.53E+040	Prieto et al. (2016)
1.27E+15	7.40E+040	Prieto et al. (2016)
1.36E+15	4.73E+040	Prieto et al. (2016)
2.06E+15	2.75E+040	Prieto et al. (2016)
2.42E+17	1.95E+040	Prieto et al. (2016)
2.42E+18	1.79E+040	Prieto et al. (2016)

Table A.1 - SED data for M87.

ν (Hz)	νL_ν (erg s^{-1})	Reference
1.40E+09	2.86E+39	Capetti et al. (2005)
2.50E+09	5.28E+39	Lazio et al. (2001)
5.00E+09	9.11E+39	Nagar et al. (2005)
1.50E+10	3.68E+40	Nagar et al. (2005)
8.62E+10	(2.28 ± 0.13)E+41	Agudo et al. (2014)
2.29E+11	(3.08 ± 0.23)E+41	Agudo et al. (2014)
3.75E+13	(1.47 ± 0.08)E+42	Gu et al. (2007)
5.17E+13	(7.72 ± 0.59)E+41	Gu et al. (2007)
6.67E+13	(4.63 ± 0.45)E+41	Gu et al. (2007)
8.33E+13	(2.95 ± 0.35)E+41	Gu et al. (2007)
3.68E+14	2.00E+41	Verdoes Kleijn et al. (2002)
5.40E+14	9.48E+40	Verdoes Kleijn et al. (2002)
(4.8–24)E+17	4.36E+41	Gonzalez-Martin et al. (2006)

Table A.2 - SED data for NGC 315.

ν (Hz)	νL_ν (erg s^{-1})	Reference
1.63E+09	2.40E+38	Jones and Wehrle (1997)
5.00E+09	5.88E+38	Nagar et al. (2005)
8.39E+09	1.24E+39	Jones and Wehrle (1997)
1.50E+10	6.71E+39	Nagar et al. (2005)
1.66E+13	(5.39 ± 0.24)E+41	Asmus et al. (2014)
2.50E+13	(4.79 ± 1.10)E+41	Asmus et al. (2014)
3.64E+14	¿ 6.03E+39	Ferrarese et al. (1996)
4.41E+14	¿ 4.60E+39	Ferrarese et al. (1996)
5.41E+14	¿ 3.96E+39	Ferrarese et al. (1996)
(4.8–24)E+17	1.03E+41	Zezas et al. (2005)

Table A.3 - SED data for NGC 4261.

A.2 Further validations

We built `AGNNES` with two different NNs: one for the RIAF component and another for the jet. Figures A.1 and A.2 illustrate how close `AGNNES`' predictions are to the fiducial model.

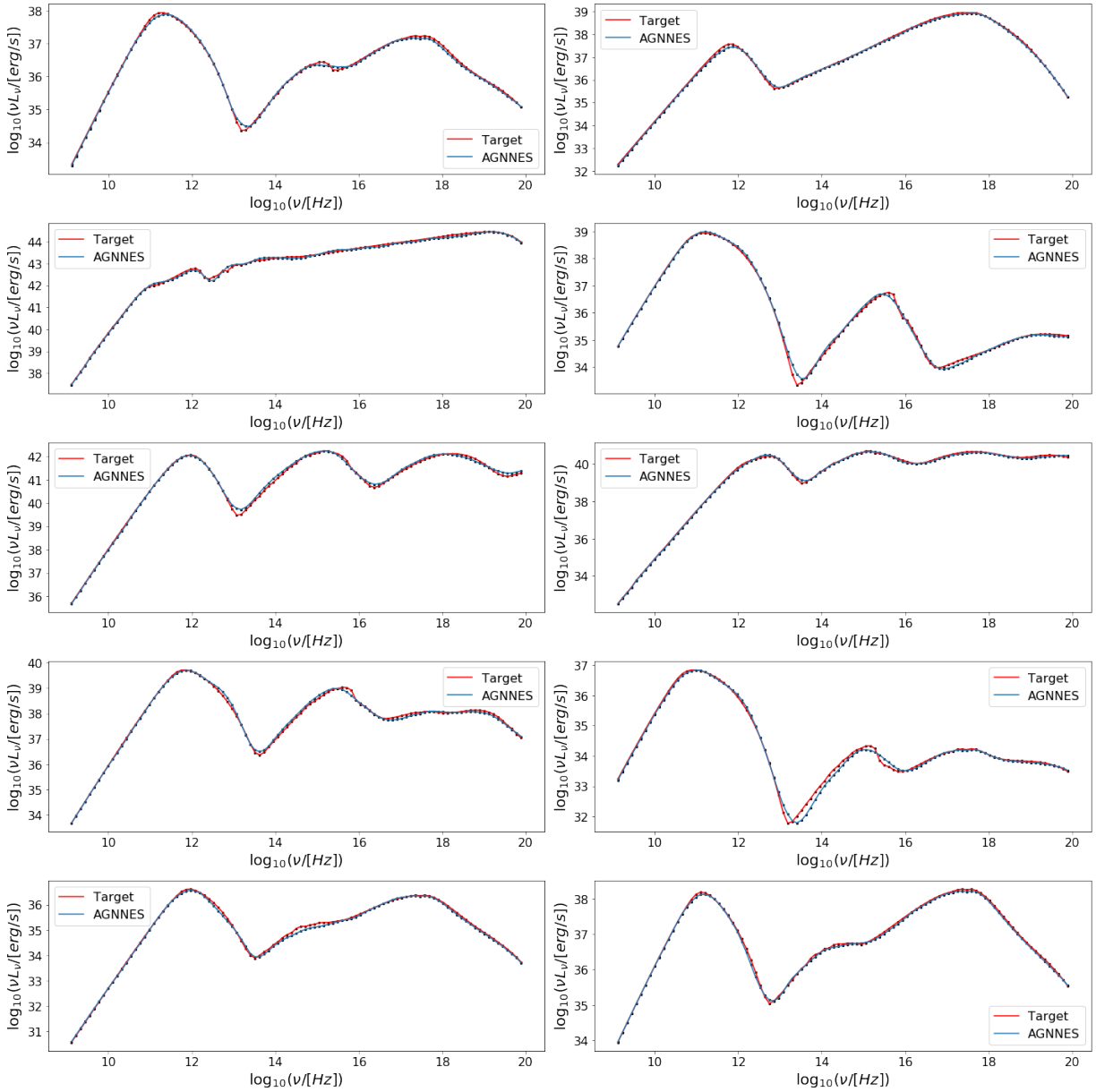

Figure A.1: Comparison of `AGNNES` predictions (blue line and black dots) with the fiducial RIAF model (red line).

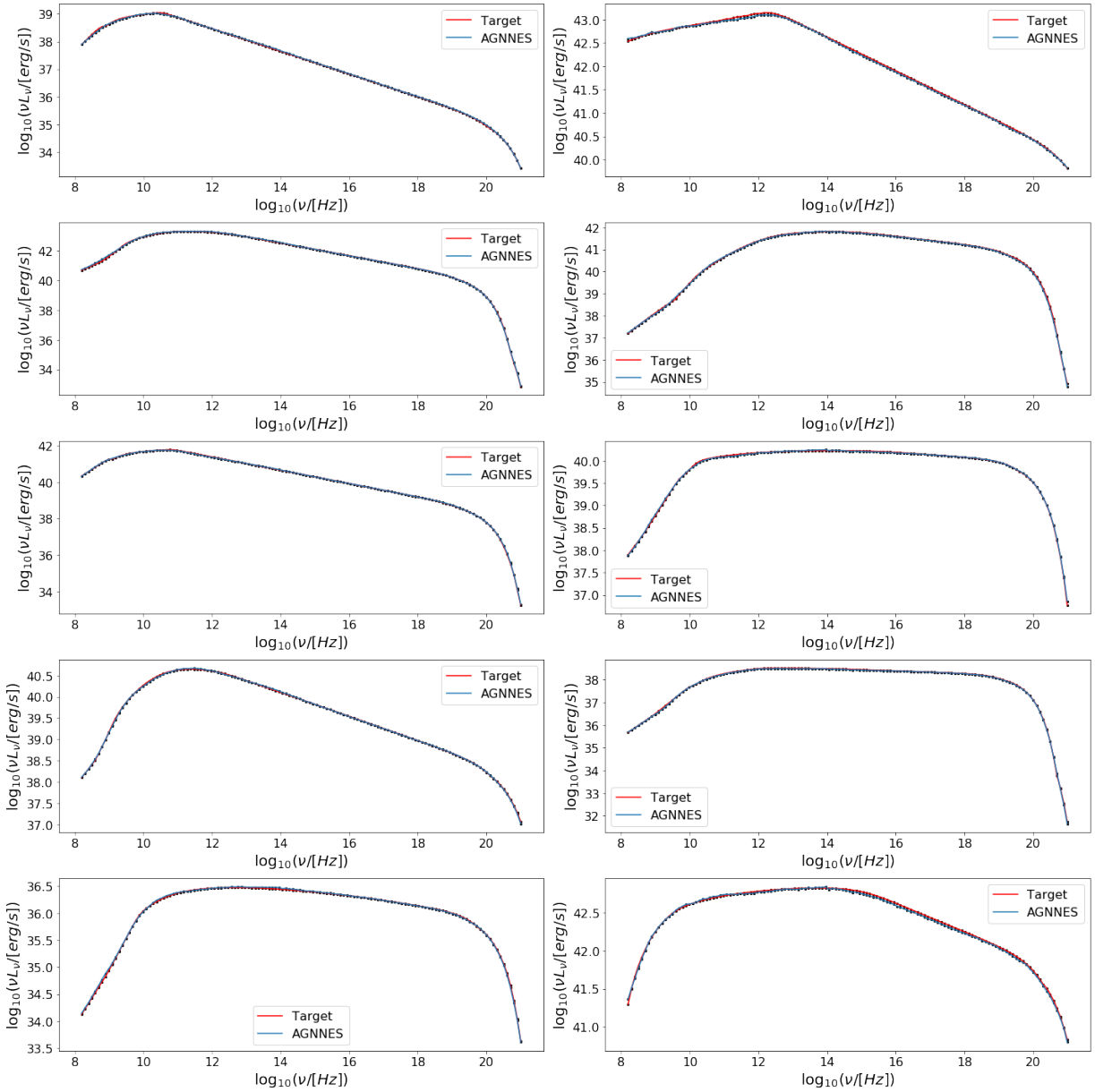

Figure A.2: Comparison of `AGNNES` predictions (blue line and black dots) with the fiducial jet model (red line).

Appendix B

Numerical Methods - Riemman Problem and Godunov method

`H-AMR` solves the fluid equations for a grid of cells using the finite volume approach. The discrete nature of this method can create a mathematical problem that can lead to numerical errors. When solving equation (2.12), we need to compute the fluxes over the boundaries of the cells locally to estimate the future value of the variable of interest as it is showed in figure B.1 (Toro, 2009; Vanzo and Siviglia, 2018).

Considering the generic quantity u, in two neighbour cells named R (right) and L (left) with boundary located at $x = x_0$ –let's ignore another cells–, we have

$$u(x) = \begin{cases} u_L & \text{if } x < x_0 \\ u_R & \text{if } x > x_0. \end{cases} \tag{B.1}$$

At $x = x_0$, we clearly have a discontinuity. The question is how the discontinuity would evolve with time as we solve the equations. For our example case, the interested equation to be solved is similar to equation (2.12).

$$\frac{\partial u}{\partial t} + \frac{\partial f(u)}{\partial x} = 0 \tag{B.2}$$

In the presence of discontinuities, it is better to use the integral form of equation (B.2)

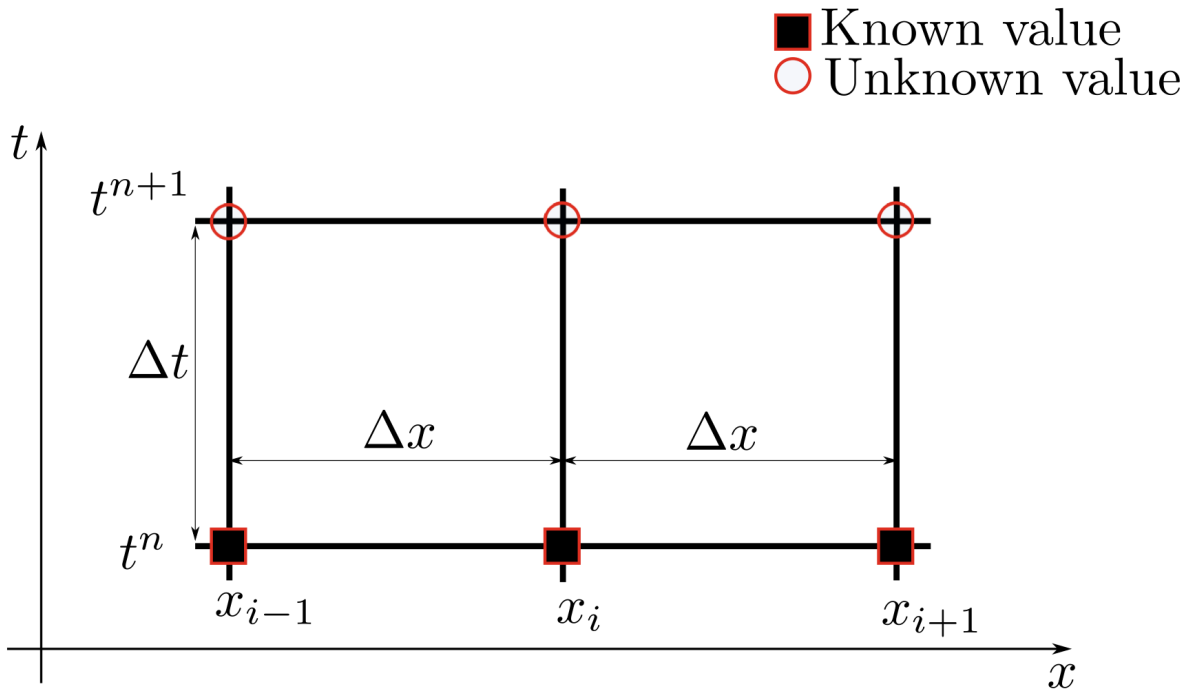

Figure B.1: Image from Vanzo and Siviglia (2018) showing the discrete grid. In this problem, we know the values of x_n at t^n, the objective is to calculate the value of x_n at $t^{n+1} = t^n + \Delta t$.

$$\oint u dx + f(u) dt = 0. \tag{B.3}$$

Looking to a generic cell delimited by the region $[x_{i-1/2}, x_{i-1/2}] \times [t^n, t^{n+1}]$, with $\Delta x_i = x_{i+1/2} - x_{i-1/2}$ and $\Delta t^n = t^{n+1} - t^n$ represented in figure B.2. For the shown cell, let's solve the equation (B.3).

$$\int_{x_{i-1/2}}^{x_{i+1/2}} u(x, t^{n+1}) dx - \int_{x_{i-1/2}}^{x_{i+1/2}} u(x, t^{n+1}) dx = -\left(\int_{t^n}^{t_{n+1}} f(u(x_{i+1/2}, t)) dt - \int_{t^n}^{t_{n+1}} f(u(x_{i-1/2}, t)) dt \right) \tag{B.4}$$

We can work only with the average values of the variables, defining the average value of the variable $Z(a, b)$ as $Z_j^m = \frac{1}{a_{j+1} - a_j} = \int_{a_j}^{a_j+1} Z(a, b^m) da$. Applying this notation to u and $f(u) = f$, we got

$$u_i^{n+1} = u_i^n - \frac{\Delta t^n}{\Delta x_i} (f_{i+1/2}^n - f_{i-1/2}^n). \tag{B.5}$$

The term $f_{i \pm 1/2}^n$ is the flux of the variables between two cells. For a conservative method, the right-side flux used to update the cell i must be the same as the

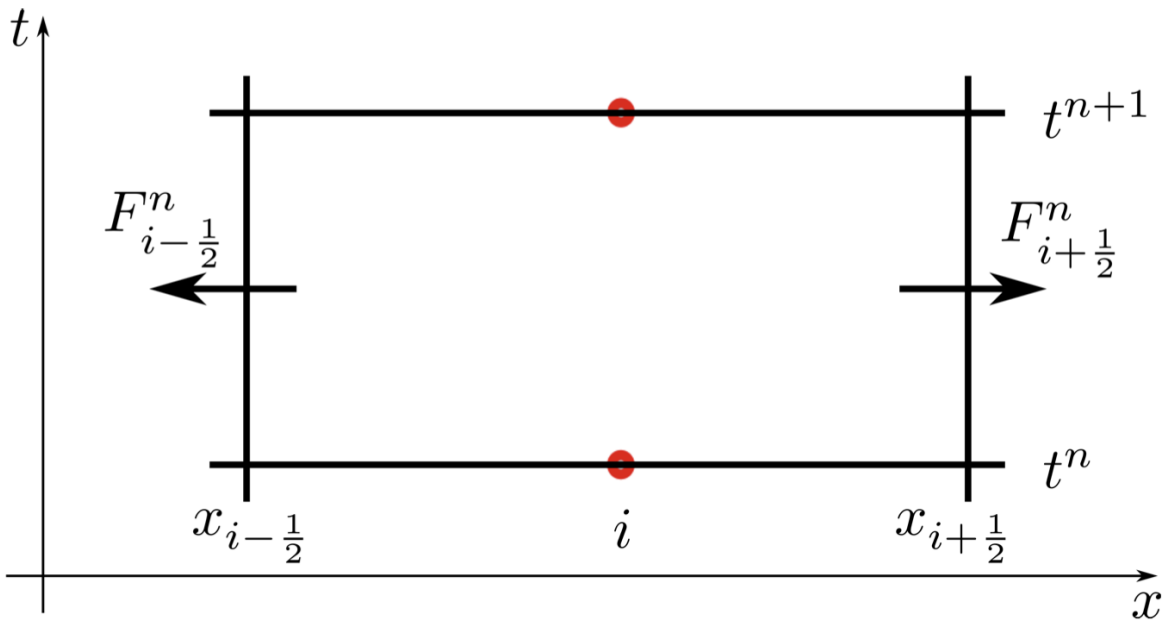

Figure B.2: Image from Vanzo and Siviglia (2018) showing the described generic cell.

left-side flux used to update the cell $i + 1$. The summation of all the fluxes between cells must be zero as we integrate over the complete domain of the calculation.

In the end, the numerical solution looks like figure B.3, and the discontinuities between cells can be described as equation (B.1). This situation characterizes the *Riemann problem*: A conservation equation coupled with an initial condition constant which has a discontinuity.

B.1 Godunov Method

The method proposed in Godunov and Bohachevsky (1959) calculates the intercell flux solving the Riemann problem at the cell boundaries. It assumed the initial condition is refreshed every time step and constant between t^n and t^{n+1}. The variable must be seen as pair (u_i^n, u_{i+1}^n) divided by a boundary at $x_{i+1/2}$. This Riemann problem (RP) is characterized by the equation (B.2), and the condition is similar to equation (B.1), but let's rewrite it

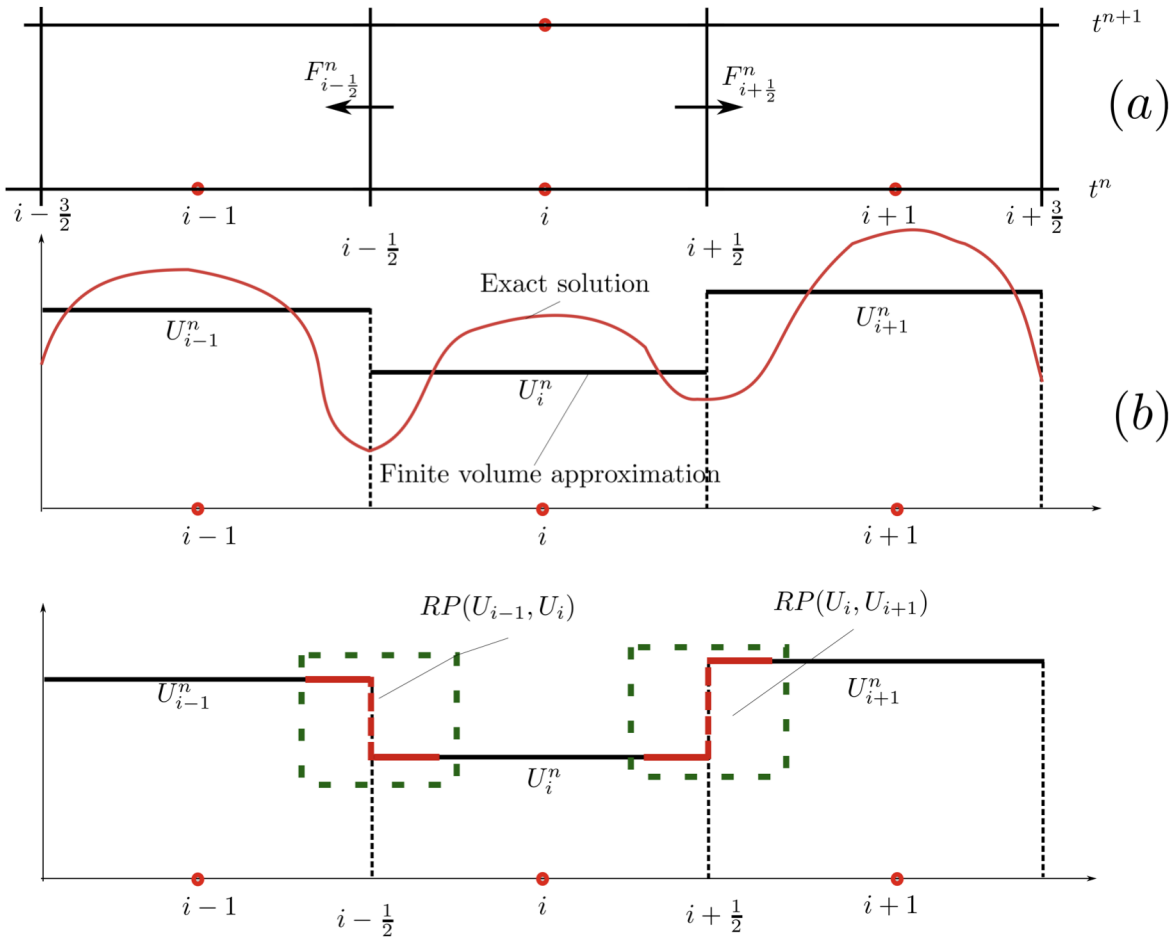

Figure B.3: Image from Vanzo and Siviglia (2018) showing the numerical solution found in equation (B.13). Note the discontinuities can be represented as the scheme in equation (B.1). The Riemann problem is related on how this discontinuities will propagate in the solution.

$$\frac{\partial u}{\partial t} + \frac{\partial f(u)}{\partial x} = 0$$
$$u(x,0) = u_0(x) \begin{cases} u_i^n & \text{if } x < x_{i+1/2} \\ u_{i+1}^n & \text{if } x > x_{i+1/2}. \end{cases} \tag{B.6}$$

To discover the value of u_i^{n+1}, we need to solve the RP in the two adjacent cell interfaces: $RP_- = RP(u_{i-1}^n, u_i^n)$ and $RP_+ = RP(u_i^n, u_{i+1}^n)$ – this can be seen in the last panel of figure B.3. After calculating $RP_\pm$, we need to take the averaged value integrated in the cell i, combining the two values.

Let's consider during the time-step we are solving a linear advection equation with $f = Ku$, with $K > 0$. The exact solutions for $RP_\pm$ become

$$u_{i-1/2}(x/t) = \begin{cases} u_{i-1}^n & \text{if } x/t < K \\ u_i^n & \text{if } x/t > K \end{cases} \tag{B.7}$$

$$u_{i+1/2}(x/t) = \begin{cases} u_i^n & \text{if } x/t < K \\ u_{i+1}^n & \text{if } x/t > K \end{cases} \tag{B.8}$$

The solution from Godunov and Bohachevsky (1959) for this problem is

$$u_i^{n+1} = \frac{1}{\Delta x}\left[\int_{-1/2\Delta x}^{0} u_{i-1/2}(x/\Delta t)dx \int_{0}^{1/2\Delta x} u_{i+1/2}(x/\Delta t)dx\right] \equiv \frac{1}{\Delta x}\int_{x_{i-1/2}}^{x_{i+1/2}} \tilde{\mathrm{u}}(x,\Delta t)dx. \tag{B.9}$$

Manipulating the result presented in equation (B.9), we can rewrite it following the idea of equation (B.4) as

$$\int_{x_{i-1/2}}^{x_{i+1/2}} \tilde{\mathrm{u}}(x,\Delta t)dx - \int_{x_{i-1/2}}^{x_{i+1/2}} \tilde{\mathrm{u}}(x,0)dx = -\left(\int_0^{\Delta t} f(\tilde{\mathrm{u}}(x_{i+1/2},t))dt - \int_0^{\Delta t} f(\tilde{\mathrm{u}}(x_{i-1/2},t))dt\right). \tag{B.10}$$

Defining

$$f_{i\pm1/2} \equiv \frac{1}{\Delta t}\int_0^{\Delta t} f(\tilde{\mathrm{u}}(x_{i\pm1/2}, t))dt. \tag{B.11}$$

We got

$$u_i^{n+1} = u_i^n - \frac{\Delta t^n}{\Delta x_i}(f_{i+1/2}^n - f_{i-1/2}^n). \tag{B.12}$$

The result is dependent of the exact solution $\tilde{\mathrm{u}}(x_{i\pm1/2}, t) = u_{i\pm1/2}(0)$ and $f_{i\pm1/2} = f(u_{i\pm1/2}(0))$. The generalization for more dimensions is straightforward

$$\mathbf{U}_i^{n+1} = \mathbf{U}_i^n - \frac{\Delta t^n}{\Delta x_i}(\mathbf{F}_{i+1/2}^n - \mathbf{F}_{i-1/2}^n). \tag{B.13}$$

B.2 Solving the Riemann problem: The HLL solver

Solving the Riemann problem for every cell boundary is a computationally challenging task. Some approximation methods were developed to speed-up the process, and `H-AMR` uses a Riemann solver known as HLL from the author's names Harten et al. (1983). We can choose the solver in `H-AMR` configurations, but HLL is the standard choice.

The method developed by Harten et al. (1983) approximately solves the Riemann problem. Coming back to the control volume $[x_L, x_R] \times [0, T]$, let's assume there is a known maximum speed signal perturbing the initial variables $U_{L,R}$ defined as $S_{L,R}$. Important to note that all intermediate states for the solution have speeds delimited by S_L and S_R.

Harten et al. (1983) suggests to use as solution of the Riemann solver the values shown in equation (B.14), where $\mathbf{F}_{L,R} = \mathbf{F}(\mathbf{U}_{L,R})$. For a more didactic derivation of the HLL solver see Soares (2021).

$$\tilde{\mathbf{U}}(\mathrm{x,t}) = \begin{cases} \mathbf{U}_L & \text{if } x/t < S_L \\ \mathbf{U}_{\mathrm{hll}} = \frac{S_R\mathbf{U}_R - S_L\mathbf{U}_L - \mathbf{F}_R + \mathbf{F}_L}{S_R - S_L} & S_L \leq x/t \leq S_R \\ \mathbf{U}_R & \text{if } x/t > S_R. \end{cases} \tag{B.14}$$

And the intercell flux become

$$\mathbf{F}_{i+1/2} = \begin{cases} \mathbf{F}_L & \text{if } x/t < S_L \\ \mathbf{F}_{\text{hll}} = \frac{S_R\mathbf{F}_L - S_L\mathbf{F}_R + S_L S_R(\mathbf{U}_R - \mathbf{U}_L)}{S_R - S_L} & S_L \leq x/t \leq S_R \\ \mathbf{F}_R & \text{if } x/t > S_R. \end{cases} \tag{B.15}$$

Appendix C

Wind calculations

C.1 Expanding bubble

Let's estimate the maximum radius reached by a thermally expanding bubble inside a medium with density described as (4.1) being cooled via bremsstrahlung.

C.1.1 Flow timescale

Starting with momentum conservation, where the wind force is applied to a layer of gas. Globally, the momentum changing is equal to the injected power by the wind ($\dot{M}_{\rm out} v_{\rm wind}$)

$$\frac{d}{dt}[M(R)\dot{R}] = \dot{M}_{\rm out} v_{\rm wind}. \tag{C.1}$$

Considering the mass outflow carried by the wind constant in time and a function of the radius R as

$$\dot{M}_{\rm out} = \dot{M}_0 \left(\frac{R}{R_0}\right)^{\alpha} = (2.23\ M_\odot\ /\ yr)\ \eta \left(\frac{M}{10^9 M_\odot}\right) \left(\frac{R}{10^4 R_S}\right)^{\alpha} \tag{C.2}$$

Rewriting equation (C.1), considering the accretion rate is related to the velocity by the relation $\dot{M}_{\rm out} = G v_{\rm wind}/f_g \sigma^2$

$$\frac{d}{dt}\left(R\dot{R}\right) = \left[\dot{M}_0 \left(\frac{R}{R_0}\right)^{\alpha}\right]^2 \left(\frac{G}{f_g \sigma^2}\right)^2 = \Lambda^2 R^{2\alpha} \tag{C.3}$$

Integrating over t in both sides and rearranging the terms considering $\dot{R} = dr/dt$

$$R^{1-2\alpha}dr = \Lambda^2 t dt \tag{C.4}$$

Then we found

$$\frac{R^2}{t^2} = \frac{1-\alpha}{2}\left(\frac{G\dot{M}_{\rm out}}{f_g\sigma^2}\right)^2 \tag{C.5}$$

Looking to equation (C.5), and defining the average velocity of the expanding bubble as $v_m = R/t$

$$v_m = \left(\frac{1-\alpha}{2}\right)^{1/2}\frac{G\dot{M}_{\rm out}}{f_g\sigma^2} \tag{C.6}$$

Defining a timescale named the "flow timescale" $t_f = R/v_m$, this time is the expected lifetime of the expanding bubble.

$$\begin{gathered} t_f = \frac{R}{v_m} = \left(\frac{2}{1-\alpha}\right)^{1/2}\frac{f_g\sigma^2}{G}\frac{R^\alpha}{\dot{M}_0}R^{1-\alpha} = \\ (4.1\times10^9 yr)\ f_g\eta\left(\frac{2}{1-\alpha}\right)^{1/2}\left(\frac{R_0}{R}\right)^\alpha\left(\frac{\sigma}{200{\rm km/s}}\right)^2\left(\frac{R}{1{\rm kpc}}\right) \end{gathered} \tag{C.7}$$

C.1.2 Cooling timescale

Considering the bubble cools via bremsstrahlung with the following timescale (King, 2003)

$$t_c = \frac{3m_e}{8\pi\sigma_T U_{\rm wind}}\frac{m_e c^2}{E}. \tag{C.8}$$

Here the U_{wind} is the density of energy of the wind and it is related to the wind power parameterized using the Eddington luminosity (see equation (1.10)) $L_{\rm wind} = f_w L_{\rm Edd}$

$$U_{\rm wind} = \frac{f_w L_{\rm Edd}}{4\pi 12 c^2 b}. \tag{C.9}$$

Where $b \lesssim 1$ and $E \approx 9 m_p v^2/16$. m_p and m_e are respectively the proton and electron masses.

Rewriting t_c

$$t_c = f_w^{-1} b \frac{2cR^2}{3GM} \left(\frac{m_e}{m_p}\right)^2 \left(\frac{c}{v}\right)^2 = 10^4 yr \left(\frac{b}{f_w}\right) \left(\frac{c}{v}\right)^2 \left(\frac{R}{1\text{kpc}}\right)^2 \left(\frac{M}{10^9 M_\odot}\right)^{-1} \tag{C.10}$$

C.1.3 Wind radius

We can estimate the "wind radius" by the relation $t_f = t_c$. This means the flow timescale is limited by the cooling timescale, the maximum radius the wind reaches comes from this relation. We need to rewrite the term from equation (C.7)

$$\left(\frac{R}{10^4 R_S}\right)^\alpha = \left(\frac{R}{10^{-4}\text{pc}}\right)^\alpha \left(\frac{M}{10^9 M_\odot}\right)^{-\alpha} = 10^{7\alpha} \left(\frac{R}{1\text{kpc}}\right)^\alpha \left(\frac{M}{10^9 M_\odot}\right)^{-\alpha}. \tag{C.11}$$

Now calculating R_{wind} as $t_f(R_{\text{wind}}) = t_c(R_{\text{wind}})$

$$\left(\frac{R_{\text{wind}}}{1\text{kpc}}\right)^{1+\alpha} 10^{-7\alpha} \left(\frac{1-\alpha}{2}\right)^{1/2} = 5.9{\times}10^5 \left(\frac{v}{c}\right)^2 \left(\frac{-f_g f_w}{b\eta}\right) \left(\frac{\sigma}{200\text{km/s}}\right)^2 \left(\frac{M}{10^9 M_\odot}\right)^\alpha. \tag{C.12}$$

Substituting the typical values, we had $(v/c)^2 f_g f_w \sim 10^{-10}$. Isolating R_{wind}, we got the result presented in equation (4.9).

$$R_{\text{wind}} = \left(\frac{5.9 \times 10^{-5} \eta^{-1} \sigma_{200}^2 M^\alpha}{10^{7\alpha}\sqrt{1-\alpha}}\right)^{\frac{1}{1+\alpha}} \text{kpc}$$

C.2 Thermal transfer

Considering the LLAGN wind effect as a smooth process modelled like a continuous heat transfer through the galactic medium, we can estimate the impact of this "heating flow".

The modelling is based on a thermal diffusion equation and considers radial symmetry. We can find the temperature ($T(R,t)$) profile solving

$$\frac{1}{R^2}\frac{\partial}{\partial R}\left(R^2\kappa\frac{\partial}{\partial R}T\right)+\dot{e}_{\rm AGN}=\rho C\frac{\partial}{\partial t}T \tag{C.13}$$

Being κ the thermal conductivity, C is the specific heat, and $\dot{e}_{\rm AGN}$ is the injection of energy due to the AGN, in the case, is the density of energy inserted through the wind at $R\approx 0$. Fabian et al. (2005) constrained the relation between κ, ρ and C for an astrophysical plasma (see equation 4). In our model we adapted it following the density profile presented in equation (4.1).

We have two ways to model the term $\dot{e}_{\rm AGN}$. Analytically, it can be modelled as the power density of the wind at launch, which we can estimate as $L_W/1pc^3$. Another option, more applicable to numerical solving, is forcing the temperature to be constant at $T(R=0)=T_{\rm wind}$. When doing the math, both options represent a continuous injection of energy into the system.

C.2.1 Analytical Solving

The analytical solution is tricky and can oblige one to explore some odd mathemathical methods that are outside the scope of our work. I opted to study a perturbation solution. The solution for equation (C.13) can be written as the sum between the homogeneous solution T_0 and the specific one T_s.

T_0 is a solution that vanishes at $R,t\to\infty$ leaving the state of a spheroid with constant temperature (our initial assumption). T_s must obey equation (C.13), and we can investigating qualitatively the following form:

$$T_s=\frac{k_1}{R}+k_2t \tag{C.14}$$

This solution aims to vanish the dependence on R and t, leaving some constants. It is not a proper solution, but it reveals two important things observed even in the other calculations like figure 4.1, the temperature –therefore the wind impact– grows linearly as time passes and decreases with the inverse of radius.

C.2.2 Numerical Solving

Last section was a qualitative analysis of the possible solution shape. Solving numerically, through a simplified finite difference method, we have the following discretized relation

$$T(R_i, t_{j+1}) = T(R_i, t_j) + T_{\rm AGN}\Theta(R_{\rm AGN}) + \frac{\delta t}{t_{th}}\left[2R_i\frac{T(R_{i+1}, t_j) - T(R_i, t_j)}{\delta R} + R^2\frac{T(R_{i+1}, t_j) - 2T(R_i, t_j) + T(R_{i-1}, t_j)}{\delta R^2}\right]. \tag{C.15}$$

$\Theta(R)$ is a step function, being $R_{\rm AGN} \approx 2pc$ and $t_{th} = \kappa/\rho C R^2$ is a thermal timescale for the system with values $\gtrsim 20$Myr.

In figure C.1, we have one possible solution. The temperature of the galaxy without the AGN is set as the unit, and the figure show a huge heating in the vicinity of the SMBH and a slight heating in the kpc region. For this model, at $R = 1$kpc, the heating was about 5% – a non-negligible increase in temperature.

Heat transfer is probably not the best model since the thermal conductivity, and density values for an astrophysical plasma are very low. These characteristics make the model underestimate the wind impact and its expansion ability. However, this calculation showed that even the "least efficient" wind propagation can reach larger distances and impact the galactic scales. Our objective in these calculations was to show the wind can get kpc scales after a Myr, and these two models show that it is possible.

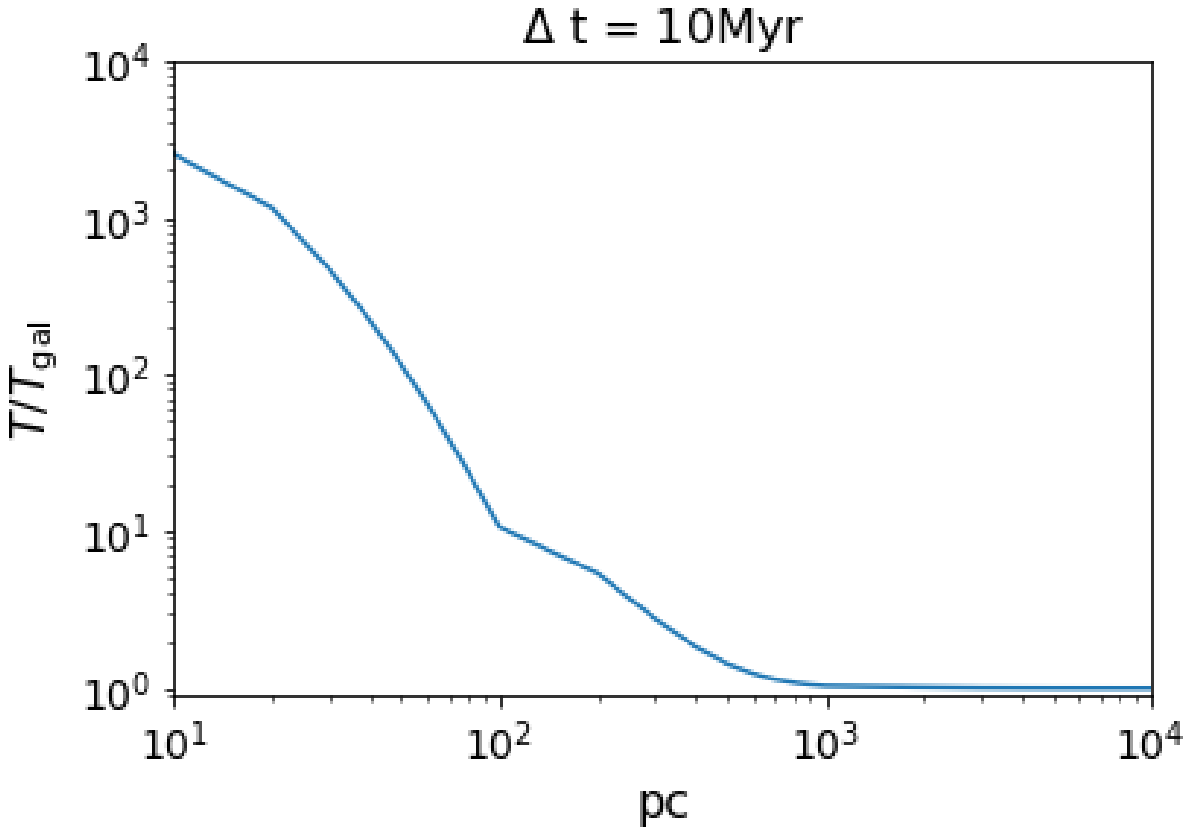

Figure C.1: Solution of equation (C.15), for a system with an AGN 10^6 hotter than the average of the galaxy and active for 10Myr. In $R = 1$kpc, the heating was $\sim 5\%$, and at $R = 10$kpc was $\lesssim 0.1\%$